The true nature of LINER galaxies

weak AGN or strong stars

Robert Artur Singh
Max-Planck-Institut für Astronomie

Heidelberg 2014

Dissertation in Astronomy

submitted to the
Combined Faculties of the Natural Sciences and Mathematics
of the
Ruperto-Carola-University of Heidelberg
Germany

for the degree of
Doctor of Natural Sciences

put forward by

Robert Artur Singh, M.Sc.
born in Offenbach am Main, Germany

oral examination: 4 February 2015

The true nature of LINER galaxies

weak AGN or strong stars

Robert Artur Singh
Max-Planck-Institut für Astronomie

Referees: **Dr. Knud Jahnke**
Dr. Christian Fendt

Abstract

Galaxies consist of dark matter, stars, dust and substantial amounts of mostly hydrogen gas and other elements. A particular sub-class of galaxies are those which exhibit low-ionisation nuclear emission line regions (LINERs) whose spectra predominantly show emission lines from weakly ionised atoms. When first identified in 1980, it was clear that the necessary radiation field had to be different than stemming from all previously known galaxies with an accreting super massive black hole, i.e. with an active galactic nucleus (AGN). Various explanations were put forward, ranging from shock-ionisation, via young hot stars, to the favoured ionisation by low-luminosity AGNs. The latter explanation has since become generally accepted.

The analysis is based on a new dataset that combines, for the first time, a complete spectral and spatial view on galaxies, whereas before either the spatial component was missing or spectral coverage for the LINER diagnostic was insufficient. All regions across all individual galaxies are classified based on the standard emission line ratio diagnostic (BPT) and show that regions with LINER-like emission at larger galactocentric radial distances show a significant excess in flux than what would be expected from AGN illumination. Furthermore evidence in support of the hypothesis of ionisation by hot old (post-AGB) stars is obtained.

These results have two immediate consequences: it necessitates a substantial revision of previous work on properties of AGN and their host galaxies where LINERs were assumed to be fully powered by the accreting black hole, and secondly it also implies a possible simplification for unified models of black hole accretion and feedback. In conclusion, our data rejects the low-luminosity AGN explanation as the sole ionisation mechanism in LINER galaxies and supports the hypothesis of ionisation by hot old stars.

Zusammenfassung

Galaxien bestehen aus dunkler Materie, Sternen, Staub und großen Mengen an Gas. Eine besondere Klasse von Galaxien sind jene, deren Gas Emissionslinienspektren von schwach ionisierten Elementen im Galaxienzentrum aufweisen, sogenannte LINER Galaxien. Mit der Entdeckung dieses Galaxientyps Anfang der 1980er Jahre konnten alle bis dahin bekannten aktiven galaktischen Kerne (AGNs), die durch Akkretion von Materie auf das zentrale schwarze Loch hochenergetische Strahlung aussenden, zweifelsfrei als Ursache für die Ionisation ausgeschlossen werden. Alternative Erklärungsversuche gingen von Stoßionisation über junge heiße Sterne bis hin zum allgemein akzeptieren AGN Model mit geringer Leuchtkraft.

Diese Arbeit basiert auf neuen Beobachtungsdaten, welche zum ersten mal zwei wesentliche Aspekte für eine Vielzahl von Galaxien verbindet und es erlaubt das gesamte optische Spektrum für jeden Bildpunkt der räumlich aufgelösten Galaxien zu untersuchen. Gebiete mit LINER Emission werden anhand der Standardklassifizierung durch Emissionslinienverhältnisse (BPT) identifiziert. Diese Arbeit zeigt, dass die singuläre Strahlungsquelle einer AGN die beobachtbaren LINER Signaturen nicht vollständig erklären kann, was bedeutet, dass dieses Modell als alleinige Ionisationsquelle ausgeschlossen werden kann.

Zudem werden weitere Ergebnisse präsentiert, welche die Hypothese stützen, dass diese Gebiete durch heiße alte (post-AGB) Sterne ionisiert werden. Diese Ergebnisse implizieren zudem, dass frühere Studien, welche sich mit den Eigenschaften von AGNs und deren Wirtsgalaxien beschäftigten, revidiert werden müssen, da diese unter der Annahme verliefen, dass LINER Galaxien ein Teil der AGNs sind. Dieser Wegfall ermöglicht außerdem eine Vereinfachung für Vereinheitlichungsmodelle von AGNs und deren Akkretionsscheiben. Es lässt sich abschließend sagen, dass unsere Daten gegen das AGN Modell und für eine Ionisation durch heiße alte Sterne sprechen.

Contents

1 Introduction

1.1 Motivation

Long time ago, in a galaxy far far away, a still controversially debated mechanism lead to the excitation of intergalactic gas, whose chemical fingerprints we observe today. However long the time and distance scales, which our data contains, are in our human perception, they are comparatively short with respect to the overall cosmic evolution. If we rescale the 13.7 billion years since the big bang into one single year, the light that we receive from the galaxies in our data, would have been emitted only two to eleven days ago. These galaxies are relatively close, making it possible to see them not as small and unresolved dots but with a good spatial resolution, enabling us to study many of their intricate details.

One of those details, which has led to the work at hand, is the question of which mechanism is responsible for the low ionisation of parts of the interstellar medium. The main focus will be on LINER galaxies, which are by definition galaxies with a low-ionisation nuclear emission line region, examining the question of whether the ionising radiation originates from a moderately accreting central super massive black hole of low luminosity – the long-established paradigm – or in how far alternative explanations, in particular the hypothesis of ionisation by hot old stars, can be supported by our data. Super massive black holes are known to exist in almost all galaxies. The only difference between ”active” and ”inactive” galaxies is whether the central black hole is being fed or not. The emitted radiation due to mass-accretion onto a central super massive black hole is often times powerful enough to produce more energy in a small region of the galaxy than the combined light of all its stars. The active galactic nucleus (AGN) in a galaxy can outshine the entire galaxy by several orders of magnitude. Of course the mode of accretion and the subsequent power output can vary. Seyfert galaxies for example show AGN activity

while being "faint" enough to also see the rest of the host galaxy, while high energetic Quasars are extremely luminous, rendering their optical appearance point-like to most telescopes.

The commonly accepted explanation for strong detection of weakly ionised atoms in LINER galaxies used to be, a low-luminosity AGN (Heckman 1980). While it has been clear from the beginning that young stars in regions of star-formation can not be spectrally identified with LINER emission, our focus is towards hot old stars, in particular so called post-asymptotic giant branch (post-AGB or pAGB) stars.

The analysis in this work is based on a new dataset (Sánchez et al. 2012) that, for the first time, combines a complete spectral and spatial view on LINER galaxies. The picture of gas ionisation in these galaxies is tested by an AGN as our null-hypothesis, which geometrically defines illumination by a single central point source. This geometry predicts a radiation field declining in radius as $\propto 1/r^2$. With interstellar gas density in galaxies normally distributed in a thin disk with an exponential fall off in radius (Bigiel & Blitz 2012), the density of ionised gas and hence surface brightness of emission line flux should also fall off similar to $1/r^2$ or faster, *if* LINER-like emission across the galaxy were caused by a central AGN point-source. We use the term *LINER-like emission* or *LINER signatures* to generalise LINER emission and include non-nuclear emission as well. If the surface brightness of spatial regions with LINER-like emission falls off less steeply than $\propto 1/r^2$, then it is not reconcilable with illumination by an AGN alone. The post-AGB hypothesis, by which regions with LINER signatures are being photoionised by hot old stars, are being analysed as well. For that, the spatial locations where LINER-like emission occurs are examined for indicators of post-AGB stars.

For these tests, both the full spatial resolution of the galaxies as well as the ability to spectrally identify LINER-like emission by means of diagnostic emission line ratios (Heckman 1980) is required. Whereas either no full spatial component was available (Cid Fernandes et al. 2011; Yan & Blanton 2012) or spectral coverage for the LINER diagnostic was limited before (Sarzi et al. 2010), the CALIFA survey (Sánchez et al. 2012; Husemann et al. 2013; García-Benito et al. 2014) provides the first dataset of this kind for a substantial number of LINER galaxies.

1.2 GALAXIES

Galaxies are generally defined as baryonic condensates in dark matter potential troughs. A galaxy is a large accumulation of stars, gas and dust, which is held together only by their mutual gravitational attraction. The galaxy in which we reside, the Milky Way Galaxy, is host to about 10^{11} stars. The observed motion of stars, in our and other spiral galaxies, does not slow down with the expected Keplerian behaviour ($v \propto r^{-1/2}$) at larger radial distances, and implies the presence

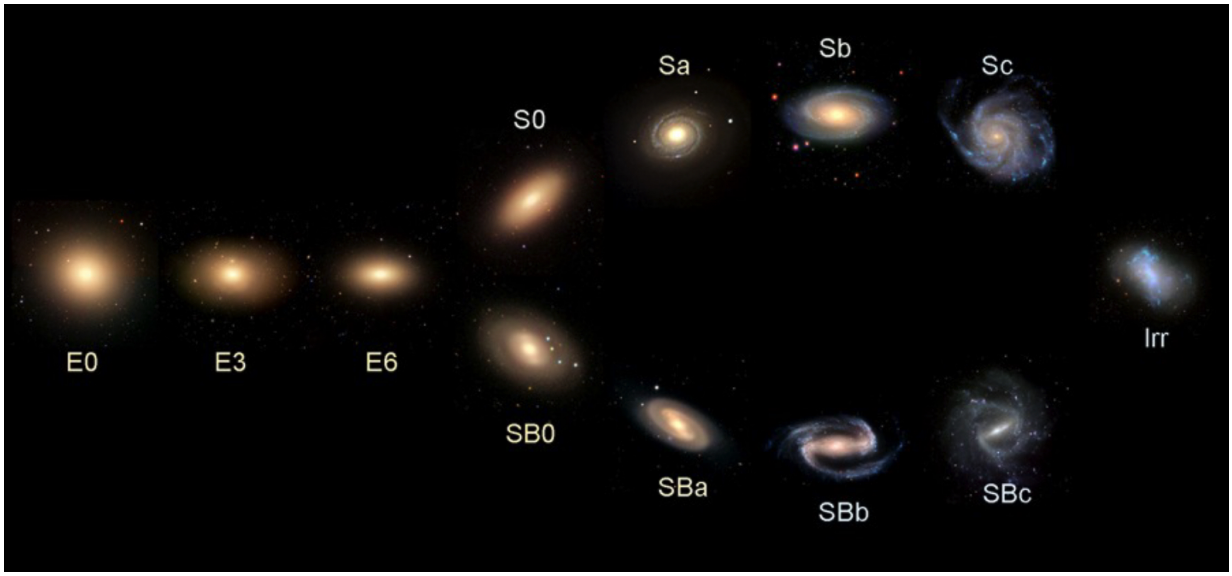

Figure 1.1: Hubble's morphological classification. Elliptical galaxies are denoted by E0-E7 depending on their ellipticity. Spiral galaxies are are divided into barred (SB) and un-barred (S) with sub-types "a" to "d", according to how bright the bulge and how tightly wound the spiral arms are. Lenticular galaxies (S0) are elliptical galaxies with a featureless disk. Irregular galaxies are denoted by Irr.

of a larger body of mass. We infer from these, so called, rotation curve measurements that our Galaxy consists of 10 times more matter, so called dark matter, which does not interact with electromagnetic radiation, hence the word, but only exerts a gravitational influence. (Schneider 2014)

The number of stars in galaxies can range from a few 10^6, in dwarf ellipticals, to 10^{13} in massive ellipticals, with varying amounts of gas, dust and dark matter. The variety of different types of galaxies is commonly categorised using the Hubble sequence (Hubble 1926) in Figure 1.1, a classification scheme, which differentiates galaxies into a number of types based on their optical morphology. The main types are: elliptical, lenticular, barred spiral, un-barred spiral, and irregular galaxies. This sequence was originally conceived as an evolutionary sequence in which elliptical galaxies (early types) evolve into spiral galaxies (late types). We nowadays know that rather the opposite is true.

Spiral galaxies are characterised by a flattened disk of stars, gas, and dust, in which the most recent star-formation occurs in spiral-shaped arms extending outwards from a densely packed central concentration of stars, also known as the bulge. Spiral galaxies have ordered rotation and a net angular momentum. They contain a larger fraction of young hot (blue) stars and have higher star-formation rates, because of proportionally larger amounts of available gas.

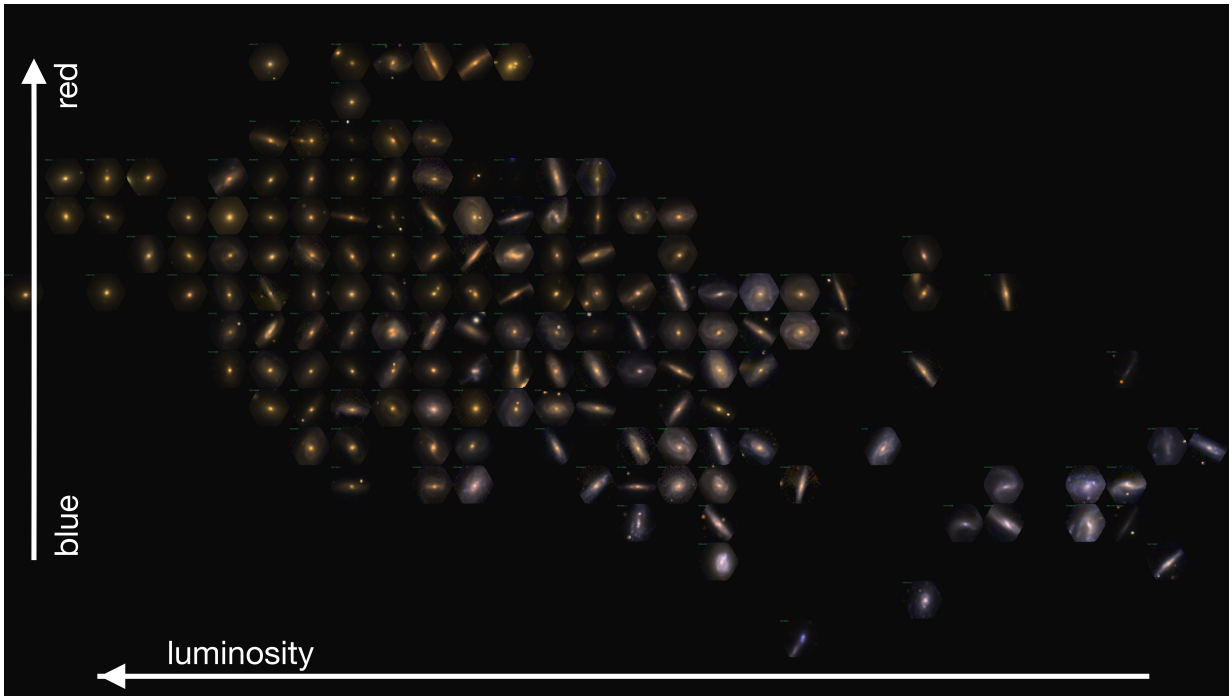

Figure 1.2: Galaxy Color Magnitude Diagram. This CMD (Sánchez CALIFA priv. comm.) is constructed only with galaxies from the CALIFA survey, which comprises galaxies of all Hubble types. From bottom to top the color changes from blue to red, and from left to right the luminosity changes from high- to low-luminous.

Elliptical galaxies however are composed of mostly older (redder) stellar populations, their gas reservoir of which new stars can be formed is getting exhausted which connects to a lower star-formation rate. As opposed to spirals, ellipticals have a low angular momentum and higher velocity dispersion. Their light distribution is rather smooth and featureless and their typically larger mass and size as well as their spherical or ellipsoidal shape bears witness to a history of interactions and mergers with other galaxies.

While irregular galaxies do not display any regular structure or pattern, lenticular galaxies are similar to spiral galaxies in that they also consist of a central bulge and are surrounded by an extended featureless disk. Unlike spiral galaxies, the disks of lenticulars does not exhibit spiral arms.

One could think that galaxies might be evenly distributed from blue spirals to red ellipticals but that is not the case. If we plot galaxy color against luminosity, this so called galaxy color-magnitude-diagram (CMD) will show two particularly overpopulated regions. The ”blue cloud” which mainly consists of star-forming spiral galaxies, and the ”red sequence” which is largely composed of old elliptical galaxies. The underpopulated space in between has been dubbed the green valley. This dichotomy was shown in Kauffmann et al. (2003a,b); Bell et al. (2004)

and Faber et al. (2007) with a sharp transition between the two distinct types of galaxies at $M^* = 3 \times 10^{10} M_\odot$. At this threshold a transition occurs from young to old stellar populations, from low to high surface mass densities, from low to high concentrations, from recent starbursts to little star-formation, or in general from late types to early types. The question of why and how galaxies undergo a rapid transition from an active to a quiescent state is however un-answered and currently another highly debated topic. Different evolutionary tracks have been suggested which, in various degrees and combinations, include minor merger and/or major merger in the form of wet (with gas) and dry (without gas) merger, or quenching of star-formation by internal mechanisms like a simple depletion of the gas reservoir and gas-heating through AGN feedback.

Figure 1.2 shows the galaxy color-magnitude-diagram with galaxies from the CALIFA survey (introduced in section 2.2). Note that this representation does not depict the bimodal distribution, since only one galaxy is being plotted per grid element.

1.2.1 ACTIVE GALAXIES

Almost all galaxies contain a central super massive black hole, which at times can accrete gas. While black holes spend most of their time in an inactive state, being quiescent, the accretion of matter onto a black hole, has severe consequences and can affect the entire galaxy. Active galaxies, or galaxies with an active galactic nucleus (AGN), can outshine their host galaxy by several orders of magnitude. They are among the brightest objects in the universe. Whether a galaxy hosts an AGN or not is typically determined by the properties of its spectrum, the existence of strong radio emission, or the luminosity of its nucleus. (Schneider 2014)

Galaxies with AGNs are commonly categorised by a number of observational properties, such as: nuclear optical continuum and infrared emission, broad and narrow optical emission lines, radio and X-ray continuum emission, and X-ray line emission. With a range of different classifiers comes a range of differently named AGNs, such as: Quasars (radio-quiet & radio-loud), radio-quiet quasars are also referred to as quasi-stellar objects (QSOs), Blazars (BL-Lac objects and optically violent variable (OVV) quasars), radio galaxies, Seyfert I, Seyfert II, and LINERs. Most classes have been historically formed. Unfortunately no single criterion exists through which alone one could easily discern active from inactive galaxies.

- Seyfert galaxies: This is the first distinct class of AGN that had been identified (Seyfert 1943). They can be divided into two classes depending on their viewing angle (Urry & Padovani 1995). The rather face-on Seyfert Is show narrow and broad emission lines. For the highly inclined Seyfert IIs, the central region is blocked by a surrounding torus of neutral gas and dust, hence only narrow lines are detectable from regions more distant

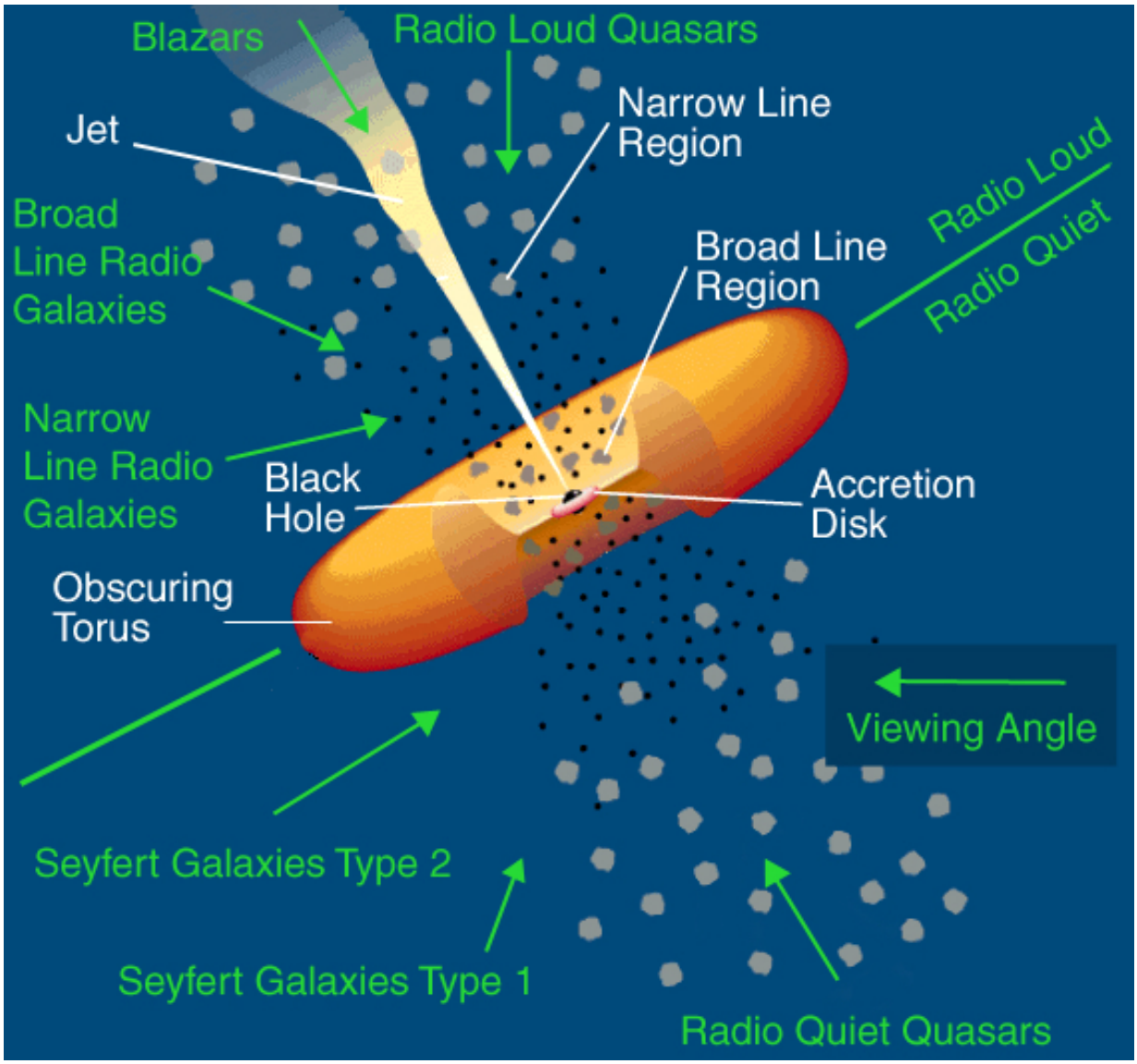

Figure 1.3: The unified picture of AGNs. This schematic shows the different types of AGN classifications, which can be understood in a unified framework as observing a single type of physical object under different conditions. (Urry & Padovani 1995)

to the nucleus. Seyfert Is are also more likely to have X-ray emission from the nucleus while Seyfert IIs oftentimes absorb the X-ray in their high column density tori. They are more likely to show radio emission from jets. The host galaxy of Seyfert-type AGNs are typically spirals.

- Quasars (quasi-stellar radio sources): 10% of quasars are radio-loud. These are the most luminous AGNs. Their optical luminosities are greater than that of their host galaxy. Quasars show strong optical continuum emission, broad and narrow emission lines, and strong X-ray emission, together with nuclear and often extended radio emission.

- Radio-quiet quasars/QSOs. Very similar to Seyfert I galaxies but more luminous. They show strong optical continuum emission, X-ray continuum emission, and broad and narrow optical emission lines. Quasars can be hosted by spirals, irregulars or ellipticals. There exists a host-mass quasar-luminosity correlation (Martini & Weinberg 2001), which is why the most luminous quasars inhabit the most massive ellipticals.

- Radio galaxies: Mostly hosted by ellipticals, these galaxies have luminosities up to 10^{47} erg s^{-1}. They show nuclear and extended radio emission and have rather heterogeneous AGN properties. Objects with a low excitation show optical and X-ray nuclear emission. They do not show strong narrow or broad emission lines. However existing emission lines may be excited by a different mechanism. Objects with a high excitation (narrow-line radio galaxies) have emission line spectra similar to those of Seyfert IIs.

- Blazars: Two more types of radio-loud objects are known as, BL Lac (BL Lacertae object, Stein et al. 1976) and OVVs (optically violent variable). In the unified AGN picture (Urry & Padovani 1995), the line-of-sight to these objects is aligned to their relativistic jet. The very similar OVVs are highly variable quasars. Their visible light output can change by 50% in a day. As opposed to BL Lacs, OVVs have stronger broad emission lines.

- LINERs: Galaxies with a low-ionisation nuclear emission line region (Heckman 1980), have historically been added to the AGN family. This type of galaxy does not show any other AGN signatures but strong low-ionisation emission lines. Emission lines of higher ionisation are relatively weak. LINER galaxies are very common. Around one third of the galaxies in the local universe are LINERs. The ionisation source driving the gas emission is still a current topic of debate and the work of this thesis is to show that the emission can not be the result of an AGN alone. We argue that hot old stars are the dominating ionisation mechanism in most galaxies, which explains the prevalent occurrence of LINER signatures throughout many galaxies, whenever gas is present and in the absence of a stronger radiation field.

Figure 1.3 shows a unification model of all AGN species. The underlying idea is that this whole variety of AGNs can mostly, or perhaps at all, be physically explained by a single class of object, observed under different conditions with different viewing-angles (Antonucci 1993; Urry & Padovani 1995).

1.2.2 LINER GALAXIES

LINER galaxies, or short LINERs, are galaxies with a low-ionisation nuclear emission line region. These galactic nuclei are spectrally defined by their strong emission lines from neutral or weakly ionised atoms such as [OI], [OII], [NII] and [SII], compared to weaker emission from strongly ionised atoms like [HeII], [OIII] and [NeIII].

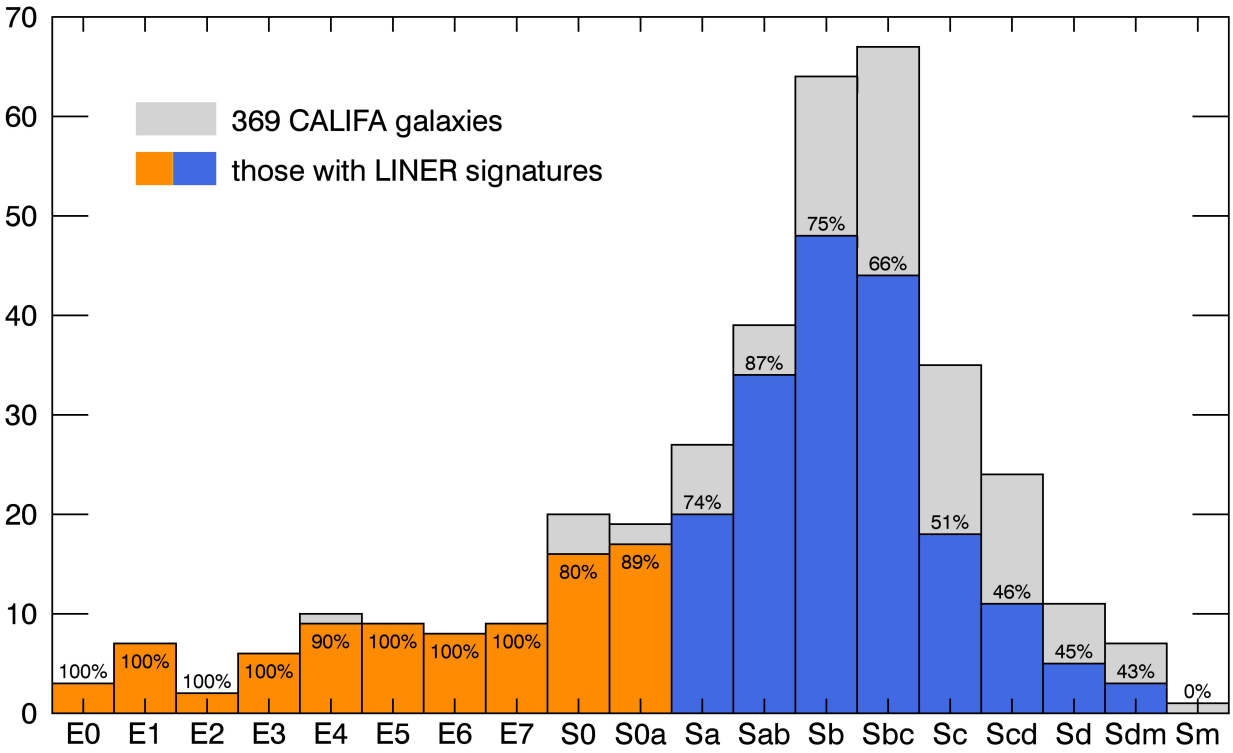

Figure 1.4: Absolute frequency of galaxies with LINER-like emission separated by morphology. The underlying distribution in grey shows our sample of 369 CALIFA galaxies separated into Hubble subtypes. The coloured filling shows how many galaxies with LINER-like emission are contained for each subtype in the Hubble sequence. Every galaxies with LINER-like emission has been taken into account, even when the emission is non-nuclear. Merging galaxies were excluded to be consistent with the upcoming analysis. Colours are used to distinguish early from late type galaxies.

When LINERs were first identified as a class of galaxies in the early 1980s (Heckman 1980), it was clear that the necessary radiation field had to be different or have a different impact than for all previously known AGNs. For both the rare high-power quasars observable across the whole visible Universe and the more common Seyfert galaxies, well-understood models of accretion disks could be computed (Shakura & Sunyaev 1973; Narayan & Yi 1994). Various explanations for the LINERs were put forward, ranging from shock-ionisation (Heckman 1980) via young hot stars (Terlevich & Melnick 1985) to the favoured ionisation by low-luminosity AGNs (Ferland & Netzer 1983; Halpern & Steiner 1983). The latter explanation has strong implications, because LINERs make up most objects in the AGN class. While in the following decades the explanation that LINERs are powered by low-luminosity AGNs became generally accepted, doubts were again re-fuelled very recently. Inconsistencies were found between the AGN-ionisation hypothesis, and either predicted emission line strengths (Cid Fernandes et al. 2011) or the spatial distribution of LINER-like ionised regions in the galaxies (Sarzi et al. 2010; Yan & Blanton 2012), but neither were conclusive, because they either lacked full spatial or spectral information.

LINER galaxies are in fact very common, about one third of the galaxies in the local universe are LINERs. Most of which (see Figure 1.4) are ellipticals, lenticulars or early type spirals (S0/a-Sab). LINERs may also be found in luminous infrared galaxies (LIRGs). Their defining strong infrared luminosities can occur when two galaxies collide with each other. In this and other cases of galaxy interactions, LINER emission is very prevalent but arises most probably due to the mechanical interaction of the gas and the inevitability of shock heating. Approximately 1/4 of luminous infrared galaxies (LIRGs) contain LINERs. Figure 1.4 shows how common LINER-like emission across all galaxies is. This histogram is based on our dataset of 369 CALIFA galaxies (see Section 2.6), and separates them into Hubble-types. The distribution in grey shows all galaxies, regardless of LINER signatures. The coloured filling however indicates how many galaxies in each category have LINER-like emission. Almost all early type galaxies exhibit LINER-like emission while the frequency decreases for later types.

1.3 ASTRONOMICAL SPECTROSCOPY

Spectroscopic observations have become a powerful technique to study objects at great distances by observing the light they emit, dispersing it, and measuring their spectra. The spectra of astronomical objects such as stars, planets, or galaxies can, for example, reveal information about their chemical composition, temperature, distance, relative motion along the line of sight, density, mass, metallicity, age and much more.

Spectra of galaxies or regions within galaxies, see Figure 2.4 for an example, are a superposition of spectra of different origins. They comprise several components that contribute to the

observed spectra, which are unsurprisingly similar to stellar spectra, since galaxies are composed of millions to billions of stars. Stellar features are commonly characterised by absorption lines, these are spectral gaps which are caused by elements in the outermost stellar atmospheres or by interspersed gas clouds between the light source and the observer.

Since the constituent stars can, for example, be of different ages, different metallicities, and different masses, an analysis of the observed combined spectrum can, given the knowledge of individual stellar spectra, help to decompose and identify the individual contributions. Further large scale properties, such as the kinematics of stars and gas, gradients or more complex distributions in other parameters, can be deduced by spectral analysis of individual regions.

The interstellar medium (ISM) is the low density gas that fills the vast space in between stars. Hydrogen, the most abundant element, constitutes 70% of the ISM by mass and 91% by number, followed by Helium with 28% in mass and 9% in number. Heavier elements only make up 1.5% in mass and 0.1% in number and form the 1% (in mass) dust particles in the ISM. The other 99% of the ISM is gaseous and, depending on the environment and the interstellar radiation field, in molecular, atomic or ionic form. Molecular hydrogen only exists in, the appropriately named, molecular clouds with high densities and low temperatures of ~10 K. Neutral atomic hydrogen exists in the Cold (CNM) and Warm Neutral Medium (WNM) with increasing temperatures of 10^2 to 10^4 K and decreasing gas density of 10^1 to 10^{-1} atoms/cm^3. Hα, one of the most prominent emission lines, traces the ionised hydrogen in H II-regions and the Warm Ionised Medium with temperatures of ~8000 K each and densities of 10^2 to 10^4 in H II regions and 10^{-1} in the WIM.

The Hα (H-alpha) emission line is one of many electron transitions in the Balmer series. The Balmer series has been the first identified set of spectral lines, because the first four lines are visible to the unaided eye. The Balmer series is characterised by electron transition from the quantised energy level $n_2 = 3$ to $n_1 = 2$. All Balmer lines have a transition to $n_1 = 2$ and are sequentially named by Greek letters as n_2 increases. Hβ therefore stands for transitions from $n_2 = 4$ to $n_1 = 2$, and so on. Figure 1.6 shows the first four Balmer lines, H$\alpha\lambda$6563, H$\beta\lambda$4861, H$\gamma\lambda$4341, and H$\delta\lambda$4102 in an absorption spectrum and Figure 1.7 in emission. These chemical fingerprints are a unique way to remotely identify the chemical composition of astronomical objects and for example infer kinematical properties like velocity and velocity dispersion, based on the amount of shift in wavelength and the line widths. Elements with higher atomic numbers sich as iron for example (see Figure 1.8) display a much more complex and numerous arrangement of spectral lines due to many more possible transitions between different energy levels.

To clarify the notation of our emission lines, as opposed to Hα and Hβ, the other emission lines (for example [NII]λ6583) are so called forbidden lines and are therefore put in square brackets. These brackets are a distinctive feature to distinguish forbidden transitions from allowed transitions. The emitted energy of certain excitation states are, perhaps misleadingly, called forbidden,

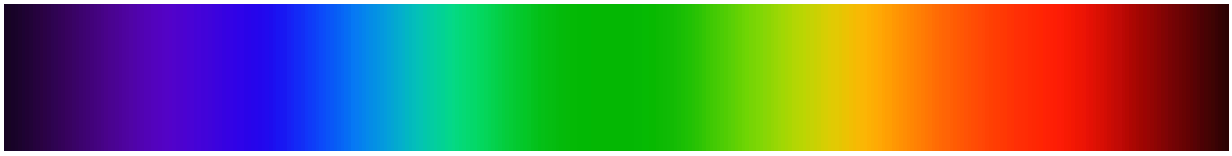

Figure 1.5: Continuous spectrum of electromagnetic radiation in the visible regime from 3500 Å to 8000 Å.

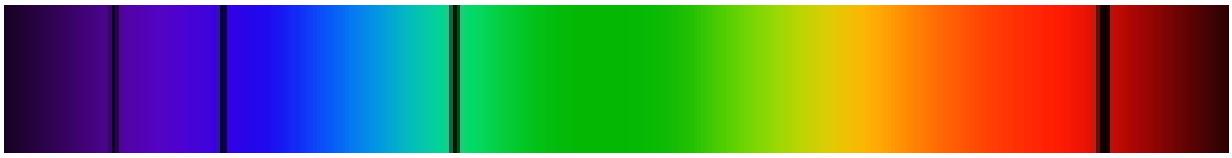

Figure 1.6: Absorption spectrum of hydrogen. Caused by hydrogen between the light source and an observer. This absorption spectrum shows the first four Balmer lines, H$\alpha\lambda$6563, H$\beta\lambda$4861, H$\gamma\lambda$4341, and H$\delta\lambda$4102.

Figure 1.7: Emission spectrum of hydrogen. Caused by a cloud of ionised hydrogen gas. It shows the same Balmer lines in emission.

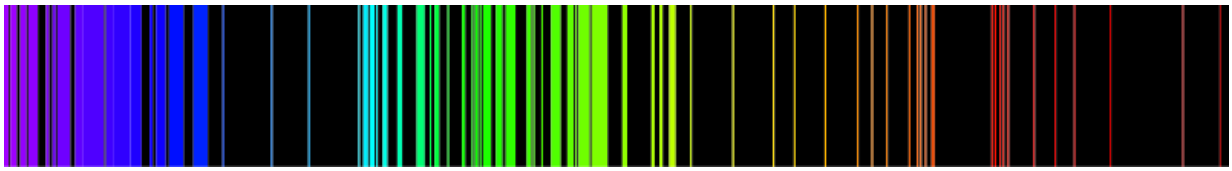

Figure 1.8: Emission spectrum of iron. Elements with higher atomic numbers have much more complex spectral signatures due to many more possible transitions between different energy levels.

not because they are against the law of physics. Of course, such photons still obey quantum-mechanics, but their occurrence has a very low probability. A certain probability exists that an excited atom or molecule will make a forbidden transition to a lower energy state but this probability is much lower than for any "permitted" transition or de-excitation via collisions. On earth, even in our best laboratory vacuum, gas densities are still too high to allow for the unlikely path of a forbidden transition. In space however, the extremely low gas densities of only few atoms per cubic centimetre, make particle collisions almost impossible and allow atoms or molecules that have been excited for any reason to emit a forbidden-line photon. Of the photons emitted by the very low density interstellar medium, forbidden transitions make up a significant percentage.

1.4 THESIS OUTLINE

This section concludes the introduction and gives a brief overview of the following chapters, in which the driving question of this thesis will recur. To concisely word the question, this work aims at showing the inadequacy of the current LINER/AGN-paradigm, adopting an alternative view for the main ionisation mechanism based on post-AGB stars, and corroborating this hypothesis by testing its implications.

Chapter 2 introduces the data together with a more detailed view on how it has been obtained. The principles of integral field spectroscopy are explained, and the spectrophotometer PMAS and the integral field unit PPak, which are the instruments in the integral field spectrograph for the CALIFA survey, are being presented. Furthermore the automated extraction of emission lines from observed spectra is described, along with the classification of ionised regions via line ratios. The data analysis pipeline used in this work is introduced with a presentation of its data products for one example galaxy. Chapter 2 ends with an online database, which contains most of our secondary data products, and will be made publicly available.

Chapter 3 tests the long-established paradigm of LINER ionisation by a low-luminosity AGN. Spatially distributed LINER-like emission line regions are analysed and compared to the expected point-source illumination that a central AGN can provide. The disparity between our observations and the AGN-model, as well as possible implications are being discussed at the end of the chapter. This chapter is adopted from the paper by Singh et al. (2013).

Chapter 4 shows how the analysis of LINER-like emission is getting extended to a larger sample of galaxies. While acknowledging that LINER-like emission can also be caused by shocks in interacting galaxies, we put such cases into a separate sub-sample for an individual analysis, and focus on two indicators for hot old stars in non-interacting galaxies, the spectrally inferred stellar ages and a low equivalent width of Hα. In the subsequent discussion section, the implications

of a detected correlation between these indicators and regions with LINER-like emission are discussed.

Chapter 5 concludes with a brief recapitulation of the initial situation, what we learned from this work and what it means for galaxies with LINER-like emission.

2 Data & Techniques

2.1 Integral Field Spectroscopy

The data analysis in this work is based on integral field spectroscopic data. Integral field spectroscopy (IFS) has become an increasingly important method to obtain astronomical data and answer questions which traditional techniques had to leave un-answered. An integral field spectrograph combines spectrographic and imaging capabilities with the purpose of obtaining spectra of spatially extended objects as a function of position.

As a matter of fact, this technique has already made its first appearance into a scientific publication in 1980 (Vanderriest 1980) with a fibre-fed spectrograph. It is due to technological advances that IFS surveys have recently gained more momentum and significance in the optical regime and have opened many new windows in the research of galaxy evolution. The concept of multi-dimensional data-cubes however has long been employed by radio astronomers. Radio interferometry can have 4 dimensions, the R.A. and Dec. position coordinates, and frequency as well as polarisation. All axes can be one- or multi-valued. Once limited to the 21-cm line, nowadays nearly all data from the EVLA and ALMA will be 3 dimensional spectro-image data-cubes.

IFS is a dramatic improvement over traditional long slit spectroscopy, since the later is based on imaging only a narrow slit, typically along the major axis of an object, and dispersing the light which falls within the aperture defined by the slit. Probing different regions of an extended object with long-slits is very time consuming since the slit must be positioned multiple times across the target by moving the whole telescope and recording separate exposures for each position.

IFS is therefore ideal to explore spatially extended objects in detail and investigate separable components. Typical areas of application are: stellar and gas dynamics in any type of galaxy, supermassive black holes, stellar populations, star formation histories, nuclear activity and fuelling

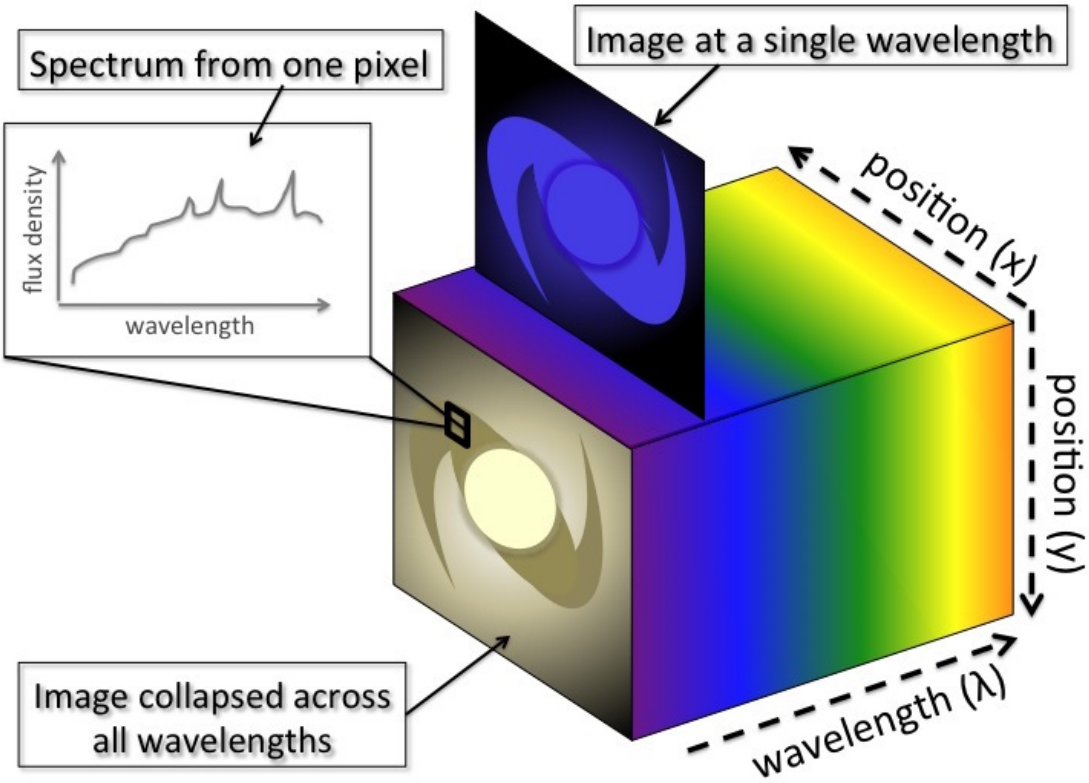

Figure 2.1: Exemplary representation of an IFU data cube. Credit: Chris Harrison[1]

of active galactic nuclei, galaxy formation, evolution and dynamics in groups and clusters of galaxies, tidal interactions and merging, and even the reconstruction of gravitational lens models and the inference of dark matter in lens galaxies.

Figure 2.1 shows a typical representation of an IFS data cube. Its dimensions are x,y or RA,DEC in the image plane and the wavelength λ in the third direction. Its face on view reveals the observed target either in single monochromatic slices or in combined light when collapsing the cube and integrating over all wavelengths. IFS observations can consist of anything between a dozen and several thousands of spectra, each originating from either an individual element of the integral field unit or from interpolation of several. These elements are commonly denoted as spaxels, which is short for spatial pixels and differentiates the spatial elements on an IFU from the otherwise ambiguously termed pixels on the detector.

[0]http://astro.dur.ac.uk/ cpnc25/research.html

An integral field spectrograph consists of two units, the spectrograph and the integral field unit (IFU). The IFU is used to divide the XY-plane and arrange the two dimensional plane into a continuous array. The following list and Figure 2.2 shows the three types of IFUs.

Lenslet arrays:

With this technique, a microlens array is placed in the image plane which splits up the input image. The array of lenses essentially transforms the image into a grid of pixels. The microlenses concentrate the light into small beams which are fed though a dispersive element, the spectrograph, and then imaged by a camera. This method provides spectra for each individual lenslet and by tilting the microlens array about the optical axis one can control in which direction the spectra are to be dispersed, as can be seen in Figure 2.2 top row. Since no spectrum should overlap with any other spectrum, the spectral length is obviously limited by the dimensions of the array and are generally very small. Furthermore the packing of the CCD is not very efficient.

This technique is for example used for the SAURON IFU (Bacon et al. 2001) on the William Herschel Telescope.

Fibre bundles:

Fibre optic cables are nowadays most commonly used to obtain spatially resolved spectroscopic observations. Using this method, the input image falls on the entrance of a bundle of fibre optic cables, which are flexible enough to arrange the other end of the fibres along a slit. This flexibility of the fibres makes it possible to forward the light from a round, rectangular or even hexagonal field of view, such that the fibre endings are still aligned along a slit and dispersed perpendicular to it in order to obtain a spectrum for each fibre. Since fibre optic cables are cylindrical, the sampling of the sky is not contiguous due to the gaps between the fibres. This issue can be solved by either placing an array of contiguous lenslets in front of the fibre to focus all the incoming light into the fibre. However fibres do not work efficiently at the slow focal ratios at which most telescopes work, which causes one handicap known as focal ratio degradation.

Fibres are for example used for the INTEGRAL IFU[2] on the William Herschel Telescope (without lenslets), Gemini GMOS-IFU[3] (with lenslets), and in these ongoing and upcoming surveys: CALIFA (Sánchez et al. 2012; see Section 2.2), SAMI (Croom et al. 2012) at the Australian Astronomical Observatory, and MaNGA[4] (as part of the Sloan Digital Sky Survey IV).

[2]http://www.iac.es/telescopes/pages/en/home/instruments/integral.php
[3]http://www.gemini.edu/sciops/instruments/gmos/?q=node/10372
[4]http://www.sdss.org/sdss-surveys/manga

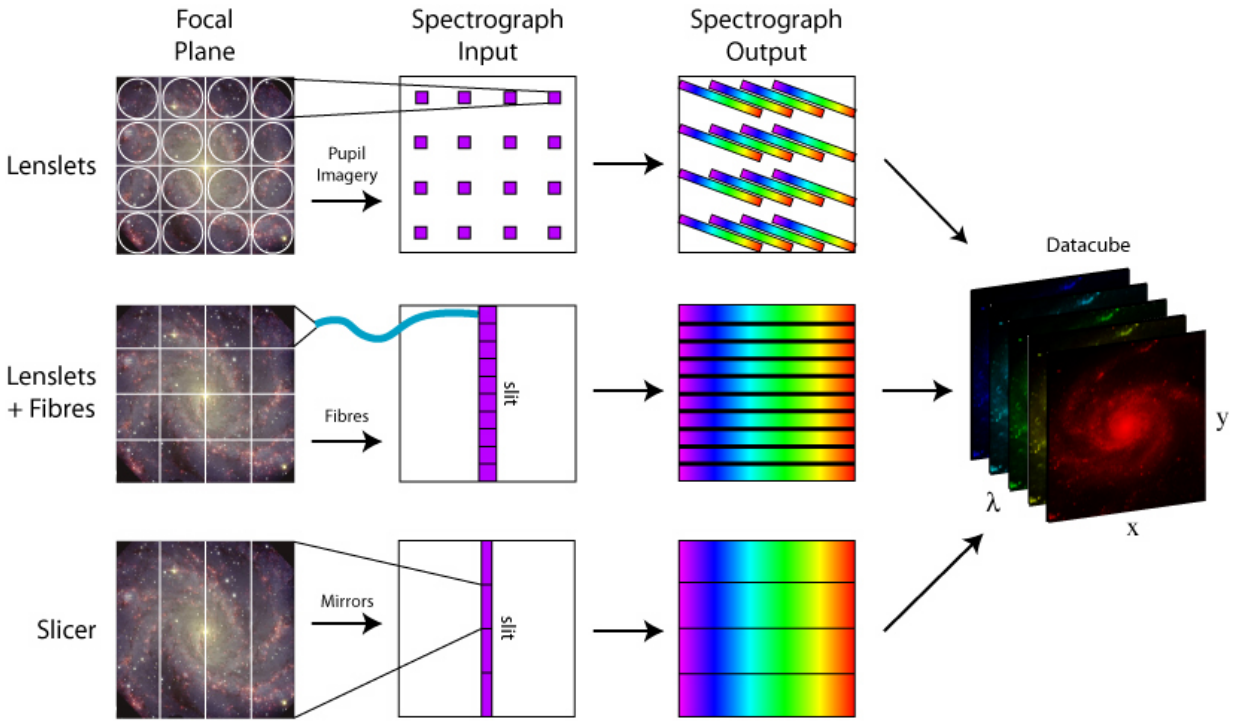

Figure 2.2: Instrument techniques used to achieve integral field spectroscopy. Credit: M. Westmoquette, adapted from Allington-Smith & Content (1998).

Image slicer:

Using this approach the observed image is being sliced, i.e. cut and re-arranged in such a way that all slices are strung together into a linear slit. Typically the input image is reflected by a mirror which consists of thin horizontal sections, each with a different orientation, and a second mirror which re-arranges the slices in order to be laid out end to end, instead of above each other. The different parts of the image in the resulting consecutive slice are then forwarded to the slit and a dispersing element of the instruments spectrograph, where a spectrum is obtained. This is practically the same as using multiple slits across the image. Advantages of this technique are a continuous coverage over the field and that focal ratio degradation is avoided. It is most adequate for infrared observations due to its inherent achromatic nature and the possibility to combine it with a cryogenic cooling system. Disadvantages of this technique are the difficulties in construction and handling of such a bulky optical system.

This technique has for example been used with VLT SINFONI (Bonnet et al. 2004) and Gemini NIFS[5].

[5]http://www.gemini.edu/sciops/instruments/nifs/

Further advantages of integral field spectroscopic observations, and in particular for data wich cover a very wide wavelength range, are the possibilities to correct for differential atmospheric refraction and dealing with a wavelength dependent point spread function. With IFS data it is even possible to separate sources which might be spatially blended but distinguishable by means of underlying spectral features. Any observed target can not only be mapped as it is seen visually, or in any particular wavelength but also physical parameters can be mapped that are derived from the spectra, going from emission lines and their ratios to stellar and gaseous velocity and dispersion maps, to stellar parameters such as mass, age or metallicity. If the signal is too faint, re-binning the spaxels enables one to gain a higher signal-to-noise ratio.

2.2 THE CALIFA SURVEY

The data for this work, were acquired through the CALIFA survey. The Calar Alto Legacy Integral Field Area (CALIFA; Sánchez et al. 2012; Husemann et al. 2013; García-Benito et al. 2014) survey is the first and currently still ongoing IFS survey of a diameter-selected ($45'' < D_{25} < 80''$) sample of up to 600 galaxies in the local universe ($0.005 < z < 0.03$) of *all Hubble types*. The data are being obtained with the PMAS/PPak IFU mounted on the 3.5 m telescope at the Calar Alto observatory. Calar Alto provides three telescopes with apertures of 1.23m, 2.2m and 3.5m to the general community. It is jointly operated by the Max-Planck-Institut für Astronomie (MPIA) in Heidelberg, Germany, and the Instituto de Astrofísica de Andalucía (CSIC) in Granada, Spain.

Our field-of-view of $65'' \times 72''$ covers the full optical extent of the selected galaxies. More than 96% of the CALIFA galaxies are covered to at least two effective radii, i.e. $2R_e$. The coverage distribution peaks around 4 R_e and reaches up to 7 R_e for highly inclined galaxies.

This survey comprises two different gratings for each galaxy: one at a lower spectral resolution (V500) of 6.0 Å FWHM and one at a higher resolution (V1200) of 2.3 Å FWHM. Since this specific analysis requires almost the whole optical wavelength range, only the V500 data are used, which cover a nominal wavelength range of 3745–7500 Å. The median spatial resolution is $3\farcs7$ FWHM.

The medium spectral-resolution V1200 grating yields high quality maps of stellar and ionised gas kinematics. The combination with the low spectral resolution V500 grating allows for mapping of stellar ages, metallicities, full star-formation histories, ionised gas emission line fluxes, and chemical abundances (e.g. Pérez et al. 2013; Sánchez et al. 2013; Falcón-Barroso et al. 2014).

2.2.1 INSTRUMENTATION

As described in section 2.1, an integral field spectrograph consists of two parts, the spectrograph and IFU. In case of the CALIFA observations, the PMAS spectrograph is used in combination with the PPak integral field fibre bundle. These instruments are attached to the Cassegrain focus of the 3.5 meter telescope at the Calar Alto Observatory (CAHA) in southern Spain. The combination of PMAS with PPak is very well suited for observations of extended object with a low surface brightness, since it offers a powerful combination of light collecting power, adequate spatial and spectral resolution and wavelength range.

2.2.1.1 POTSDAM MULTI-APERTURE SPECTROPHOTOMETER – PMAS

PMAS, the Potsdam Multi-Aperture Spectrophotometer, was developed and entirely built at the Leibniz Institute for Astrophysics (AIP) in Potsdam, Germany (Roth et al. 2005). PMAS was initially designed as a travelling instrument but has been installed at CAHA on Juli 1st, 2002 and has since been a common user instrument. It is by design a dedicated integral field spectrophotometer as opposed to IFUs which can be deployed in front of a conventional slit spectrograph.

This instrument is optimised to cover the whole optical wavelength range from 3,500 Å to 10,000 Å and has user-selectable gratings with groove densities from 1200 to 300 gr/mm, providing a spectral resolution of $\Delta\lambda = 1.5 - 7$Å. The PMAS spectrograph has a resolving power

$$R = \frac{\lambda}{\Delta\lambda} \tag{2.1}$$

of 800 to 8000, with $\Delta\lambda$ being the smallest difference in wavelength that can be distinguished at wavelength λ. The standard IFU is a lens array with 16×16 elements (256 spectra) and a relatively small field-of-view of 16×16 arcsec^2 using a 1.0 arcsec seeing limited sampling. A 0.5 and 0.75 arcsec sampling even reduces the FOV to 8×8 and 12×12 arcsec^2 respectively. The lens array IFU is recommended for studies requiring high spatial resolution.

In addition to the lens array, the off-axis fibre bundle IFU PPak provides a much larger FOV of 74×65 arcsec^2. It is recommended for low surface brightness objects and its large field of view comes at the expense of a lower spatial resolution (2.7 arcsec per fibre diameter).

2.2.1.2 PMAS FIBRE PACK – PPAK

PPak, the PMAS Fibre Pack, is the fibre based integral field unit for PMAS . This specialised fibre bundle was also developed and built at the AIP (Kelz et al. 2006), successfully integrated within PMAS in December 2003 and commissioned in spring 2004. PPak was designed to provide an extended field-of-view and to have a large light collecting power with an adequate spectral resolution. While the physical size of the central IFU fibres is only 4 mm, its coverage on the sky is more than 1 arcmin.

The PPak IFU consists of 382 fibres in total. As can be seen in Figure 2.3, it has an hexagonal fibre arrangement of 331 fibres in the centre, around which 6 concentrically aligned spots with each 6 fibres amount to the 36 sky-fibres, which are essential for the subsequent sky-removal. An additional set of 15 fibres are directly attached to internal spectral lines lamps. These calibration fibres are being illuminated during the science exposures to provide a synchronous spectral calibration. The contiguous FOV of the densely packed hexagonal grid is 74×64 arcsec, with a filling factor of 60%. Each individual fibre covers $2\farcs68$ in diameter on the sky and the six mini IFUs tracing the sky are at a distance of 72 arcsec from the centre. The PPak fibres are optimised to cover the wavelength range from 4000 Å to 9000 Å.

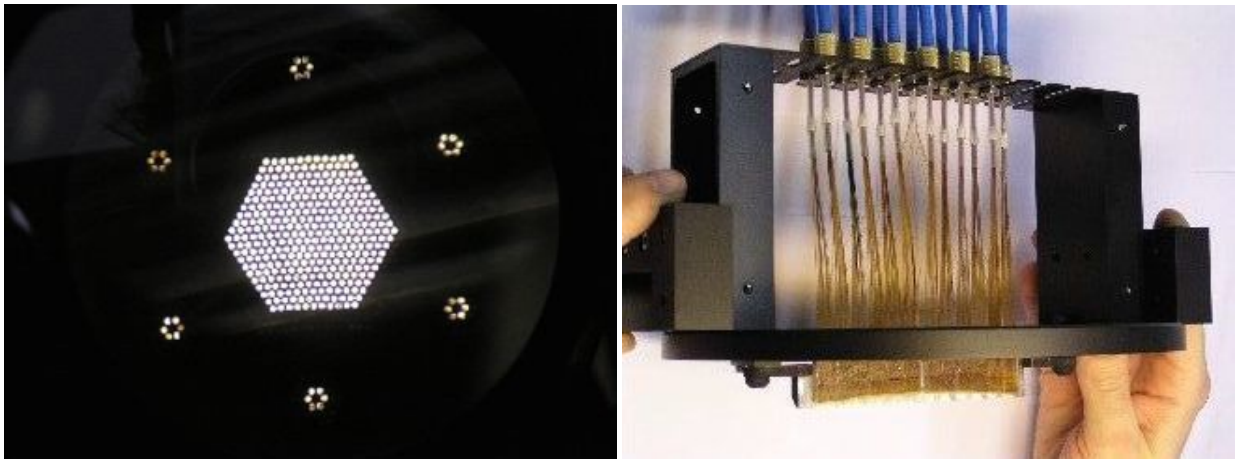

Figure 2.3: PPak IFU fibres. Left: Hexagonal array of 331 science-fibres surrounded by 36 sky-fibres. Right: The other end of the fibres is rearranged to a 1d slit which sits in the focal plane of the PMAS spectrograph. Sky and calibration fibres are evenly distributed among the fibre slit. Figures adopted from Kelz et al. (2006).

2.3 EMISSION LINE EXTRACTION

The initial goal of this work was to reliably discern the influence of emission lines from absorption lines in each spectrum by means of an automated process.

The electromagnetic radiation which is being recorded in spectra of astronomical observations comes from photons, which, at one point in time, have been emitted by stars or gas for example in the interstellar (ISM) or circumgalactic medium (CGM). The light of these stars that eventually reaches our telescopes is composed of photons that either made their long journey unhindered or became scattered or absorbed and re-emitted by interjacent particles in clouds of gas and dust. The combination of both effects results in what is typically seen as absorption and emission lines.

Even though stars typically irradiate their energy across a large wavelength scale, certain elements such as hydrogen, or heavier elements, which have been formed later through nuclear-synthesis, absorb the outgoing radiation. But because the energy of a photon which is required to excite e.g. a hydrogen's electron to a higher state cannot be arbitrary but must abide the laws of quantum mechanics, therefore only certain transitions are possible which results in a very distinct signature of gaps for each element in a stellar spectrum.

The visible wavelength range of our observations is dominated by the Balmer lines. The Balmer series is caused by an electron transition from $n_2 \geq 3$ to $n_1 = 2$, where n refers to the principal quantum number. In 1890 Johannes Rydberg generalised Balmer's formula for hydrogen, which then allowed to compute the wavelength of many other electron transition for many other chemical elements and predicted their spectral positions. The Rydberg equation is given by

$$\frac{1}{\lambda} = R_\infty \left(\frac{1}{n_1^2} - \frac{1}{n_2^2} \right) = \frac{m_e e^4}{8\epsilon_0^2 h^3 c} \left(\frac{1}{n_1^2} - \frac{1}{n_2^2} \right) \tag{2.2}$$

where R_∞ is the Rydberg constant, n_1 and n_2 are the principal quantum numbers after and before the electron transition, m_e is the electron rest mass, e is the electric charge of the electron, ϵ_0 is the permittivity of free space, h is the Planck constant and c the speed of light.

Due to the abundance of hydrogen in the universe, these lines are relatively strong with respect to other spectral lines. Table 2.1 lists all emission lines that are considered for this work. Absorption and emission lines that are caused by a change of state in rotation, vibration or excitation of the inner shell are not being discussed since they affect spectral regions in the microwave regime, infrared or X-ray respectively, which are therefore not probed by the CALIFA observations.

2.3.1 PENALISED PIXEL-FITTING – PPXF

PPXF is a computer program which extracts the stellar kinematics or stellar populations from absorption lines in the spectra of galaxies. The method of the "parametric recovery of line-of-sight velocity distributions from absorption line spectra of galaxies via penalized likelihood" or in short: penalised pixel-fitting (pPXF) is described in Cappellari & Emsellem (2004).

It's main principle, the modelling of a spectrums continuum, is achieved by fitting a superposition of differently weighted stellar templates to an observed spectrum in pixel space, while masking out the emission lines. The solution of the best fit for a given spectrum then gives the line-of-sight stellar velocity, velocity dispersion, higher order Gauss-Hermite moments (h_3 to h_6) and the stellar populations which could produce the observed spectrum.

Observables such as surface brightness, rotation velocity or velocity dispersion at a given position on the sky are always seen in projection along the line-of-sight (LOS). The normalised line-of-sight velocity distribution (LOSVD), which corresponds to its three-dimensional quantities, is given by

$$\mathcal{L}(x, y, v_z) = \frac{1}{\Sigma(x, y)} \int\int\int f(\vec{x}, \vec{v})\, dv_x\, dv_y\, dz \tag{2.3}$$

with $f(\vec{x}, \vec{v})$ as the phase-space distribution function, $\Sigma(x, y)$ as the projected surface mass density, and the distance z along the line-of-sight. By analysing the stellar absorption line profiles, acquired by spectroscopy, LOSVDs are being obtained observationally. Even though deviations from a Gaussian distribution are typically small, the LOSVDs are generally not perfectly Gaussian, making it necessary to parametrise it with a Gauss-Hermite series

$$\mathcal{L}(v) = \frac{1}{\sigma\sqrt{2\pi}} exp\left(\frac{-(v-V)^2}{2\sigma^2}\right)\left[1 + \sum_{j=3}^{N} h_j H_j[(v-V)/\sigma]\right] \tag{2.4}$$

where v is the line-of-sight velocity, V the mean and σ the dispersion of the best-fit Gaussian. H_j are the j-th degree Hermite polynomials and h_j the Gauss-Hermite moments. For example, the third moment (j=3) is associated with the skewness and the fourth moment (j=4) with a profiles kurtosis.

The reasons for fitting the line-of-sight velocity distribution in pixel space are the following. It is easy to exclude emission lines and bad pixels from the fit. It is easy to take the continuum matching directly into account. It is computationally feasible and libraries with high spectral resolution of stellar and galactic spectra are available.

To parametrically recover the LOSVD in pixel space, one must construct a model spectrum. The model spectrum $G_{mod}(x)$ can be constructed under the assumption that there exists a template $T(x)$, which is a good representation of the actual stars that created the observed spectrum.

$$G_{mod}(x) = T(x) \otimes \text{LOSVD} \tag{2.5}$$

Here x denotes the logarithmically re-binned wavelength ($x = ln(\lambda)$). The modelled spectrum is in fact a luminosity weighted sum of individual stellar spectra redshifted according to their LOSVs and convolved with a parametrised LOSVD.

$$G_{mod}(x) = \sum_{k=1}^{K} w_k \left[\mathcal{L}(cx) \otimes T_k\right](x) + \sum_{l=0}^{L} b_l \, \mathcal{P}_l(x) \tag{2.6}$$

where K is the number of stellar template spectra of a given library, w_k are the individual, non-negative template weights, $\mathcal{L}(cx)$ is the broadening function, with $\mathcal{L}(v)$ the LOSVD, c the speed of light, and $\mathcal{P}_l(x)$ are the Legendre polynomials of order l to correct for low frequency differences in shape between the data and template spectrum.

To evaluate the agreement between model and data, a χ^2 minimisation is used for all pixels in the fitted spectra.

$$\chi^2 = \sum_{n=1}^{N} \left(\frac{G_{mod}(x_n) - G(x_n)}{\Delta G(x_n)} \right)^2 \tag{2.7}$$

Where N is the number of good pixels that are being considered in the fit, $G(x_n)$ is the measurement, and $\Delta G(x_n)$ the measurement error. The minimisation of χ^2 is a non-linear least squares optimisation problem which can be solved efficiently with various routines.

The method of *penalised* pixel fitting introduces a secondary term to the χ^2:

$$\chi^2_p = \chi^2 + \alpha\mathcal{P} \tag{2.8}$$

While all parameters (v, σ, h_3, h_4, h_5, h_6) are fitted simultaneously, the addition of an adjustable penalty term $\alpha\mathcal{P}$ serves the purpose of biasing the solution towards a Gaussian shape, when the signal-to-noise (S/N) ratio of the data is insufficient to constrain the higher Gauss-Hermite moments.

In its latest modification for CALIFA (Husemann et al. 2013), pPXF also allows for a Monte Carlo simulation for each spectrum, based on its initial best-fit with the addition of normal distributed noise. As previously mentioned, the best-fit solutions contain the stellar kinematics for each spatial bin in a galaxy, which is subsequently used as the initial guess value for GANDALF.

2.3.2 GAS AND ABSORPTION LINE FITTING – GANDALF

GANDALF, the gas and absorption line fitting routine from Sarzi et al. (2006), is a spectral-fitting code which has been designed to separate the relative contribution of a spectrums emission lines and its underlying stellar continuum. It measures the gas emission and kinematics and is the heart of the IDL data analysis pipeline described in section 2.5.

GANDALF is not the only publicly available code to measure the contribution of emission lines, but unlike other routines, GANDALF has a unique approach. Other emission line fitting codes fit the stellar continuum first, while masking the spectral regions that are potentially affected by emission lines. Then after subtracting the best fit continuum from the data, the gas emission is measured on the residual spectrum. As described in Section 2.3.1, the stellar continuum is typically matched by a superposition of template spectra convolved with the stellar LOSVD, whereas the emission and kinematics of the gas is derived assuming a Gaussian LOSVD. This method of masking spectral regions can be particularly troublesome for weak emission lines. It can introduce biases when fitting the stellar contribution and cause spurious features in residual spectra which in turn might influence the measurement of the gas emission.

The GANDALF code is designed to measure the gas fluxes and kinematics by fitting both, the stellar continuum and gaseous emission lines *simultaneously*, without masking any spectral regions. Gaussian templates are used to represent the emission lines. Their spectral position (gas velocity), width (gas dispersion) and amplitude are iteratively searched for, while it also finds the best superposition of templates from the stellar library, which are being convolved with the best stellar LOSVD.

The crucial information about which emission lines are to be fit, including their specific parameters, is stored in a separate emission lines setup file. This setup file contains the emission lines that are listed in table 2.1. For each emission line the rest-frame wavelength must be specified, along with other line specific details such as its dispersion, or its possible affiliation to a multiplet. In case of multiplet emission lines, the main component has to be indicated as well as the relative strength of the other components. The two parameters stellar velocity and stellar velocity dispersion, which are obtained from the perviously described pPXF results, are now used as an initial guess for the fitting process. For the strongest emission lines, Hα and [NII]λ6583, gas velocity and its dispersion are both subject to the χ^2 minimisation. Weaker Balmer lines (Hβ, Hγ, Hδ, Hϵ) are typically fixed in velocity to their more prominent Hα counterpart, making the assumption that the origin of these emission lines is co-spatial and hence exhibits the same kinematic properties. The same is true for the other metal lines, which are typically tied in velocity space to [NII]λ6583.

#	emission line	wavelength [Å]	multiplets	rel. strength
0	HeII	3203.15	-	1.000
1	[NeV]	3345.81	-	1.000
2	[NeV]	3425.81	-	1.000
3	[OII]	3726.03	-	1.000
4	[OII]	3728.73	-	1.000
5	[NeIII]	3868.69	-	1.000
6	[NeIII]	3967.40	-	1.000
7	H5	3889.05	#24	0.037
8	He	3970.07	#24	0.056
9	Hd	4101.73	#24	0.091
10	Hg	4340.46	#24	0.164
11	[OIII]	4363.15	-	1.000
12	HeII	4685.74	-	1.000
13	[ArIV]	4711.30	-	1.000
14	[ArIV]	4740.10	-	1.000
15	Hb	4861.32	-	0.350
16	[OIII]	4958.83	#17	0.350
17	[OIII]	5006.77	-	1.000
18	[NI]	5197.90	-	1.000
19	[NI]	5200.39	-	1.000
20	HeI	5875.60	-	1.000
21	[OI]	6300.20	-	1.000
22	[OI]	6363.67	#21	0.333
23	[NII]	6547.96	#25	0.340
24	Ha	6562.80	-	1.000
25	[NII]	6583.34	-	1.000
26	[SII]	6716.31	-	1.000
27	[SII]	6730.68	-	1.000
30	[ArIII]	7135.67	-	1.000

Table 2.1: Typical list of emission lines that are being fitted with GANDALF.

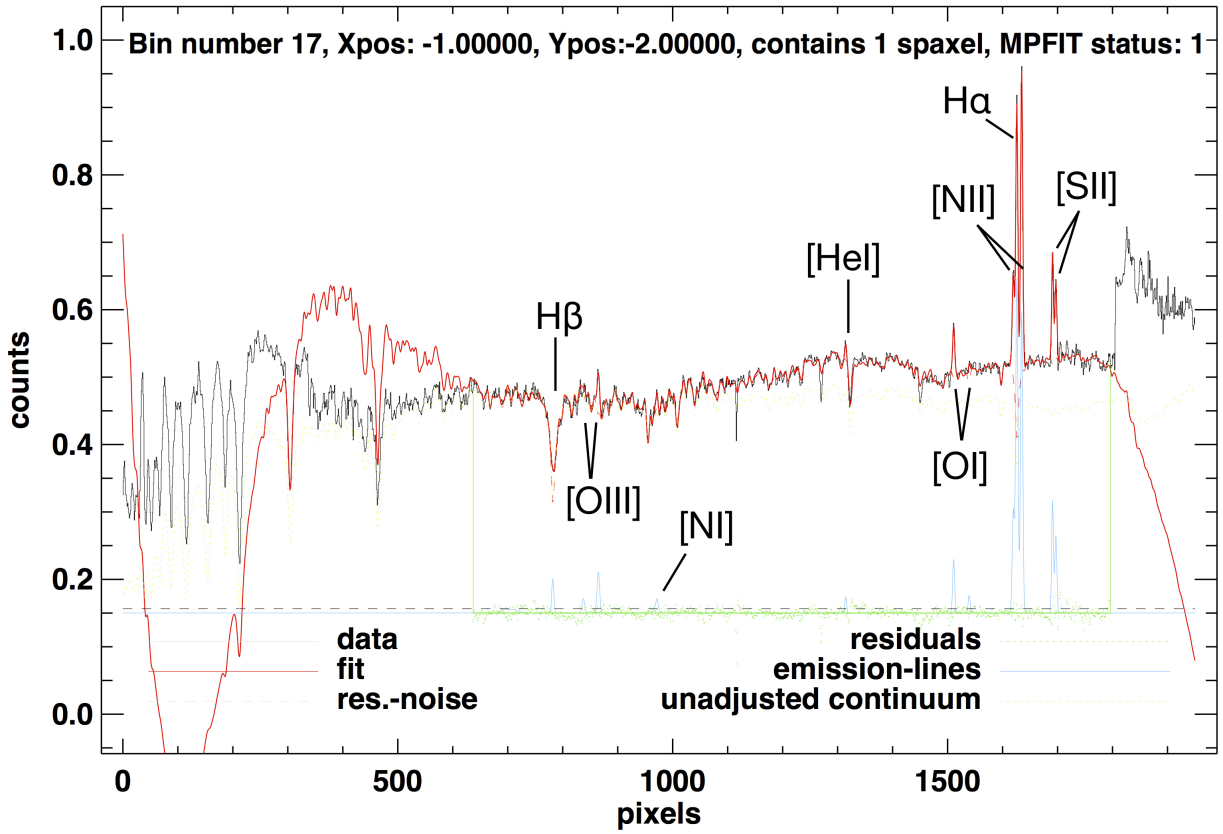

Figure 2.4: Emission line fit with GANDALF of one random example spectrum in NGC2623. The data is shown in black, the fitting range from 4700 Å to 7100 Å as green vertical lines, the fit to the data in red, the fitted emission lines in blue, the residuals as green dots and auxiliary information is printed above the lines

In order to reliably fit the continuum emission of the underlying stellar component, one needs a library of stellar templates. These libraries typically consist of ~100 to ~1000 stellar spectra, covering a broad range of stellar parameters. The observed spectra and the stellar templates must have the same spectral resolution and the same wavelength sampling. A model of the underlying stellar continuum then can be constructed by obtaining a best superposition of individually weighted stellar spectra.

Figure 2.4 shows an example spectrum. The original data is shown in black, the best-fit shown in red, models the data very well within the confines of the fitting range from 4700 Å to 7100 Å shown by the green vertical lines. This figure shows all available 1951 spectral pixels. In blue we see the emission lines only, analogously the dashed red line shows only the contribution of the stellar continuum. It overlaps here with the solid red line almost everywhere, except for the Hβ absorption trough. The Hβ emission line here results from the gap between anticipated stellar model (red dashed) and the fit (red solid) observed flux (black). Without simultaneously

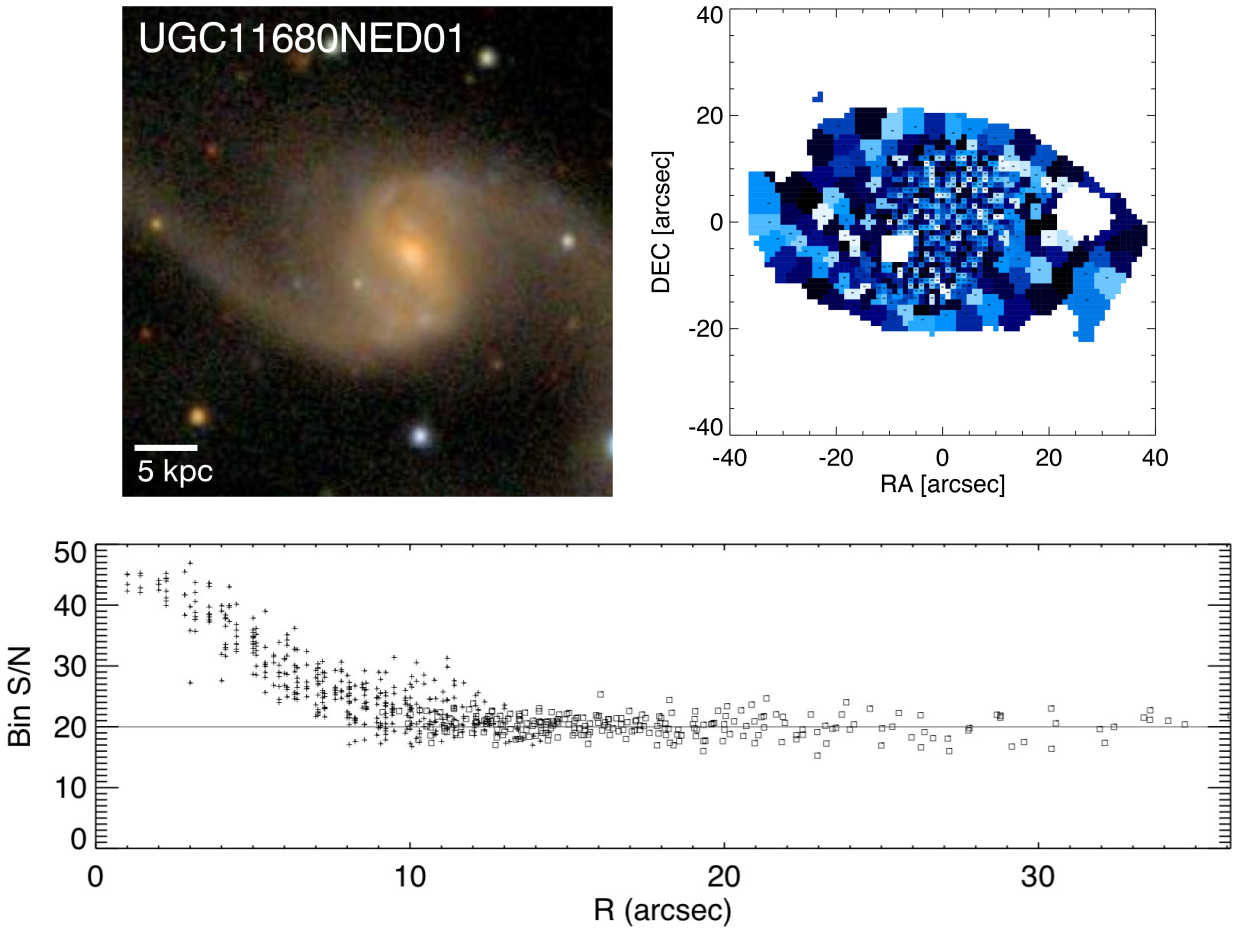

Figure 2.5: Voronoi binning. This example galaxy shows the concept of Voronoi binning. Upper left: SDSS image of UGC11680. Upper right: Binned Voronoi map, with individual spaxels in the centre and bins composed of multiple spaxels in the outer parts. Bottom: Radial distribution of bins and their S/N value. Central bins have a higher signal-to-noise than the required target value, hence binning only affects spaxels at larger radii. Un-binned individual spaxels are plotted as crosses, bins as squares.

fitting for both, the stellar continuum and the gaseous emission lines, the existence of such weak emission lines is hard to recover.

The three plots in Figure 2.5 visualise the principle method of the Voronoi tesselation. The Voronoi binning method of Cappellari & Copin (2003) is an optimal solution to the problem of preserving as much spatial resolution as possible, generally in two-dimensional data, while maintaining a minimum signal-to-noise ratio. The upper left plot shows an SDSS image of one example galaxy (UGC11680). The target signal-to-noise ratio was set to 20. In the bottom figure, the S/N vs. radius profile illustrates that, in this galaxy and similarly in others, Spaxels within a ∼10 arcsec radius already have a higher S/N value than 20, and are therefore not being binned. At larger radii the S/N drops below the target-value and hence individual spaxels must be

binned. Un-binned individual spaxels are plotted as crosses, bins as squares. The upper right plot shows the result of one Voronoi binned galaxy. Colors are randomly picked in order to visualise individual bin sizes. It distinctly shows how central bins are composed of individual spaxels, whereas outer bins contain multiple spaxels, and that bin-size gradually increases with radius.

2.4 EMISSION LINE RATIO DIAGNOSTICS

2.4.1 THE BPT DIAGRAM

The so called BPT diagram (Figure 2.6) is a commonly used optical emission line ratio diagnostic diagram, named after Baldwin, Phillips and Terlevich (Baldwin et al. 1981). Is is an empirically derived diagnostic tool which separates, based on the principal excitation mechanism, emission line regions into 4 different categories: star-forming HII regions/galaxies, type 2 Seyfert galaxies, LINERs and intermediate or composite regions/galaxies, which are likely to be influenced by more than one ionisation mechanism, thus difficult to classify.

Ths ISM can be ionised by many different mechanisms, such as hot OB stars, starbursts, shocks, AGN activity and presumably hot old post-AGB stars. The fact that different gas excitation mechanisms ionise the gas differently and that this can be distinguished by utilising specific line ratios was pioneered by Baldwin et al. (1981) and later revised by Veilleux & Osterbrock (1987). Baldwin et al. (1981) investigated the merits of emission line intensity ratios and build a classification scheme which would separate between HII regions, planetary nebulae, objects photoionised by a power law continuum, and objects excited by shock-wave heating. The choice of emission line ratios in the current BPT diagram is based on the following criteria by (from Veilleux & Osterbrock 1987). Emission line ratios should consist of strong lines that are easy to measure. Each ratio should have lines with a relatively small separation in wavelength so that the effect of reddening can be neglected but not too small so that blending can be avoided. Ratios including one Balmer liner are more abundance sensitive and should therefore be preferred. The ratios of emission lines that abide to these criteria are: [OIII]λ5007/Hβ, [NII]λ6583/Hα, [SII]$\lambda\lambda$6716,31/Hα, and [OI]λ6300/Hα.

Figure 2.6 shows the central emission line ratio distribution of 85.224 SDSS DR4 galaxies in the BPT diagram. It is apparent that there are at least two separate sequences of emission line galaxies populating the log([OIII]/Hα) vs. log([NII]/H) diagram. The red solid curve by Kewley et al. (2001) provides a theoretical classification scheme to separate starburst galaxies from AGNs. This extreme starburst line is based on self-consistent photoionisation models from the MAPPINGS III code. It is however obvious that the separation of the two sequences of emission

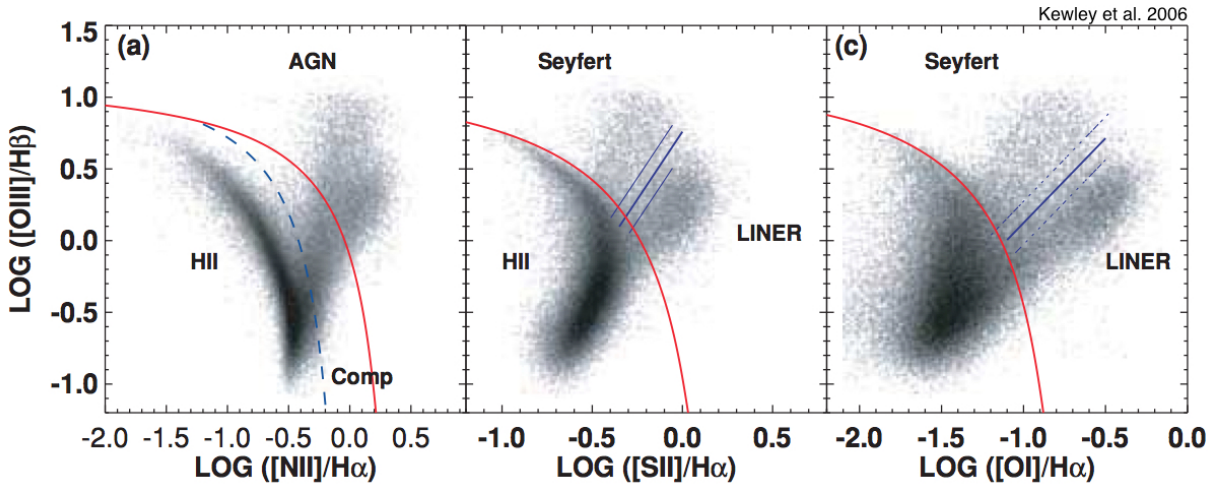

Figure 2.6: BPT diagram with SDSS data. Central apertures of 1″.5 radius show the central emission line ratios of 85.224 galaxies. The red solid curves are the theoretically modelled extreme starburst line (Kewley et al. 2001). The blue dashed curve (Kauffmann et al. 2003c) and solid lines (Kewley et al. 2006) are tracing a minimum in the central emission line ratio distribution of SDSS galaxies. This figure is adopted from Kewley et al. (2006).

line galaxies is located well below this curve. Instead of a theoretical approach, the blue dashed cure in the first panel (Kauffmann et al. 2003c) is a fit along the minimum of this bimodal distribution. Complementary to this, the blue solid lines in the second and third panel (Kewley et al. 2006) are also tracing a minimum in a bimodal distribution of Seyfert and LINER galaxies.

2.4.2 FURTHER LINE DIAGNOSTICS

Beside the BPT diagram there are a few more optical line diagnostics, mostly to discern AGNs and regions of star-formation.

- The *blue diagram* by Lamareille et al. (2004); Lamareille (2010) distinguishes between Seyfert 2 and star-formation and uses the flux ratio of [OIII]λ5007/Hb and the equivalent width ratio of [OII]λ3727/Hb. This might be useful if the spectral coverage is either too narrow or the emission lines around Hα are redshifted out of the optical spectrum.
- The *color-excitation* (CEx) diagram by Yan et al. (2011); Juneau et al. (2011) also disentangles star-forming galaxies from AGNs using the [OIII]λ5007/Hb flux ratio and rest-frame U-B color. Galaxies can be classified out to a redshift of z$\sim$1.
- The *mass-excitation* (MEx) diagram by Juneau et al. (2011, 2014) combines [OIII]λ5007/Hb and stellar mass to compute a probability of belonging to galaxies classified as purely star-

forming, LINER, composite or Seyfert 2. Galaxies can be categorised out to a redshift of z∼1 with optical spectra and z∼3.5 with near-IR spectra.

- The *DEW diagram* by Stasińska et al. (2006) draws a star-formation/AGN demarkation line through the parameter space of $D_n(4000)$ against max(EW[OII]λ3727,EW[NeIII]λ3869).
- The *TBT diagram* by Trouille et al. (2011) uses rest-frame g-z color and the [NeIII]λ3869/[OII]λ3726,29 line ratio to distinguish AGNs from star-forming galaxies. This diagnostic reaches out to a redshift of z∼1.4
- The *WHAN diagram* by Cid Fernandes et al. (2011) is based on the equivalent width of H (WHa) and the line ratio of [NII]/Ha. This diagnostic can also classify weak emission line galaxies and distinguishes between pure star-forming galaxies, strong AGN, weak AGN, retired galaxies, and passive galaxies.

2.5 MY DATA ANALYSIS PIPELINE

The development of an automated IDL pipeline, which reliably fits emission lines in a vast number of spectra for a large number of galaxies, was an early and major goal. Further development, either on the fitting part, or the many plotting routines perpetually remained one aspect of this work.

The pipeline takes as input the reduced CALIFA data, listens to various configuration files, stores its results into separate fits files, which can then be forwarded to a number of the different plotting routines. The GANDALF code (see section 2.3.2) is used to do the spectral fitting within this IDL pipeline. It is designed to fit both the stellar continuum and the emission lines simultaneously. Instead of masking the spectral regions where the emission lines are assumed to be and fitting the residuals, the emission lines are being treated as additional Gaussian templates, and solved for while finding at the same time an optimal superposition of stellar templates, which are convolved with the stellar LOSVD.

Different options can be set within the configuration files. Besides the emission line setup file, which was introduced on page 25, the main configuration file handles which galaxies are to be processed and the following parameters:

- FILENAME: Name of the rscube file. Multiple jobs will be run in sequence if more than one galaxy is selected.
- A/N-MIN: Threshold for keeping spectra with emission lines above a desired amplitude-to-noise ratio. If set to zero, then the signal-to-noise cut from PPXF will be adopted.

- REF-LINE: Rest-frame wavelength (in Å) to select the emission line which is needed to compute the A/N-min threshold.
- S/N-TARG: The target signal-to-noise value for Voronoi binning. Individual spaxels below this value will be binned using the Voronoi tesselation until the S/N of a bin approximately matches the targeted value. If set to a negative value the "REGION-FILE" will be loaded and all spectra will be binned accordingly.
- PLOT: Switch to turn off plotting, printing on screen or saving the output to a pdf-file.
- ERROR: Switch to obtain measurement uncertainties either from the internal GANDALF routine or to include a Monte Carlo simulation, which perturbs the input spectra, based on the associated error cube, to gain an estimate for measurement uncertainties of emission lines that are otherwise not provided with errors. By default, the former and less time consuming option is taken.
- QUIET: Switch to enable minimal verbose mode.
- VSYS: Systemic velocity of the galaxy.
- LMIN: Minimum rest-frame wavelength (in Å) to be considered in the fit.
- LMAX: Maximum rest-frame wavelength (in Å) to be considered in the fit.
- POL: Polynomial order to be used to compensate flux calibration difference between data and templates.
- SIG-INSTR-A: Instrumental resolution [3.2 Å for V500; 1.25 Å for V1200]
- SN-PPXF: Signal-to-noise ratio used in the preceding PPXF run.
- EMIFILE: Name of the ASCII file which containis the information of the emission lines to be fitted and sky-lines to be masked.
- LIBFILE: Name of the stellar templates library.
- REGION-FILE: Name of the region-file, in case a different binning scheme has to be adopted. By default, all spectra are binned using the Voronoi binning algorythm. One can instead provide different binning files and, for example, extract only the spectra of a galaxies central aperture.

The results which are being stored after a successful run, contain the best-fit to each spectrum, the best-fit emission line templates, the weights for each individual stellar template as well as

the MPFIT status keyword, which indicates whether a fit was able to converge successfully. Furthermore the names of all emission lines that were being considered are saved together with their line fluxes, amplitudes, the gas velocity, velocity dispersion, and errors if available, along with all ancillary data and spatial coordinates necessary to reconstruct 2-dimensional maps and other plots.

Figure 2.7 to Figure 2.33 exemplarily illustrate, for one of the 369 analysed galaxies, most of the data products that are derived. After applying the emission line fitting code described in section 2.3.2 and extracting the contribution of emission lines from the spectra, we are able to show for each galaxy the emission line flux maps of Hα (Figure 2.7), its errors (Figure 2.8), Hβ (Figure 2.19), [NII]λ6583 (Figure 2.13), its errors (Figure 2.14), [SII]$\lambda\lambda$6716,31 (Figure 2.20), [OIII]λ5007 (Figure 2.21), and [OI]λ6300 (Figure 2.22).

Furthermore, the kinematics, a non-essential by-product of this analysis, are derived from the two unconstrained emission lines Hα and [NII]. For Hα, the velocity field of this particular galaxy and the velocity errors are shown in Figure 2.9 and Figure 2.10 respectively. Errors are typically low near the galactic centre and generally increase as a function of galactocentric radial distance. The Hα velocity dispersion map and its errors are shown in Figure 2.11 and Figure 2.12. For [NII] the velocity and dispersion maps, as well as their errors, are shown in Figures 2.15 to 2.18.

All plots show the contour levels of the underlying stellar continuum and "half-light ellipses". The parameters of the ellipses are the following: the semi-major axis is set by the half-light radius, and the semi-minor axis is determined by the eccentricity of the system

$$\epsilon = \sqrt{1-(1-e)^2} = \sqrt{1-\left(\frac{b}{a}\right)^2} \tag{2.9}$$

with b/a as the minor-axis to major-axis ratio, and e as the ellipticity. The b/a-value was obtained from collaboration internal data catalogues.

Similarly to Figure 2.6 the standard emission line diagnostic diagram (BPT diagram) is constructed for all individual galaxies. With the advantage of spatially resolved spectroscopic information from IFS data, the necessary emission line ratios of all spatial bins within a single galaxy are computed and their distribution is plotted in the line ratio space of Figure 2.23. The solid curved lines are the theoretically modelled "extreme starburst lines" (Kewley et al. 2001). The dashed line (Kauffmann et al. 2003c) and the dotted line (Cid Fernandes et al. 2010) in (a) and the straight solid lines (Kewley et al. 2006) in (b) and (c) are tracing a minimum in the central emission line ratio distribution of SDSS galaxies. Data points are coloured by galactocentric radial distance. In this example case, the galaxies centre is dominated by AGN/Seyfert signatures with high ionisation. We also see data points in the star-forming and LINER section of this diagram.

The information in the BPT diagram from Figure 2.23 can be transformed into a two-dimensional map (Figure 2.24), which makes it much easier to recognise structures and spatially coherent signatures of different ionisation features. The grey area in this plot shows all theoretically available bins but different factors can be responsible in omitting certain regions. First of all, all bins must have a high enough signal-to-noise ratio (here S/N=20), and the relative error in each ratio must not exceed a given threshold (here 50%). Secondly, all six emission lines have to be detected. Since the very weak [OI]-line is often times undetectable and subject to the highest measurement uncertainty, only the first two panels of the BPT diagram are being considered, which loosens the restriction to a detection of five emission lines. If only one of these lines fails to be reliably measured, the corresponding bin in the BPT map is greyed out. Thirdly, the individual panels in the BPT diagram do not always yield a consistent classification.

Only data points are plotted in the BPT map which were unambiguously assigned to the same section of the BPT diagram. The example galaxy interestingly reveals regions of ionisation for all four types. The centre is dominated by AGN/Seyfert emission, the spiral-arms are unsurprisingly dominated by star-formation, intermediate and LINER-like emission is spatially dispersed, where the ionising radiation field is not dominated by the influence of young hot stars or the central AGN.

Figure 2.25 shows a two-dimensional map of the equivalent width in Hα (EW(Hα)). Its significance will be described in section 4.2. It reveals a strong spatial correlation of LINER signatures occurring in regions of low EW(Hα) and star-formation occurring in regions with higher EW(Hα). The implication of this discriminability is discussed in the above mentioned section and the subsequent conclusion section. The histogram in Figure 2.26 better depicts the separation of emission line regions with star-formation and LINER signatures. LINER-like regions are plotted in green, star-formation in blue, the Seyfert region in orange and intermediate regions in light-blue.

Figure 2.27 to 2.30 show light-weighted stellar-age maps, with different overlays to highlight the spatial locations of regions with star-formation (2.27), composite (2.28), LINER-like (2.29), and Seyfert (2.30) emission. How stellar ages are derived is explained in section 4.3.

Figure 2.31 and 2.33 show the [OIII]/Hβ vs. [NII]/Hα part of the BPT diagram. The datapoints are coloured according to the equivalent width in Hα (2.31), [OIII] (2.32), and [NII] (2.33). The EW(Hα) is approximately constant for a given [NII]/Hα-value while EW([OIII]) is approximately constant for a given [OIII]/Hβ-value. EW([NII]) is mostly similar to EW(Hα).

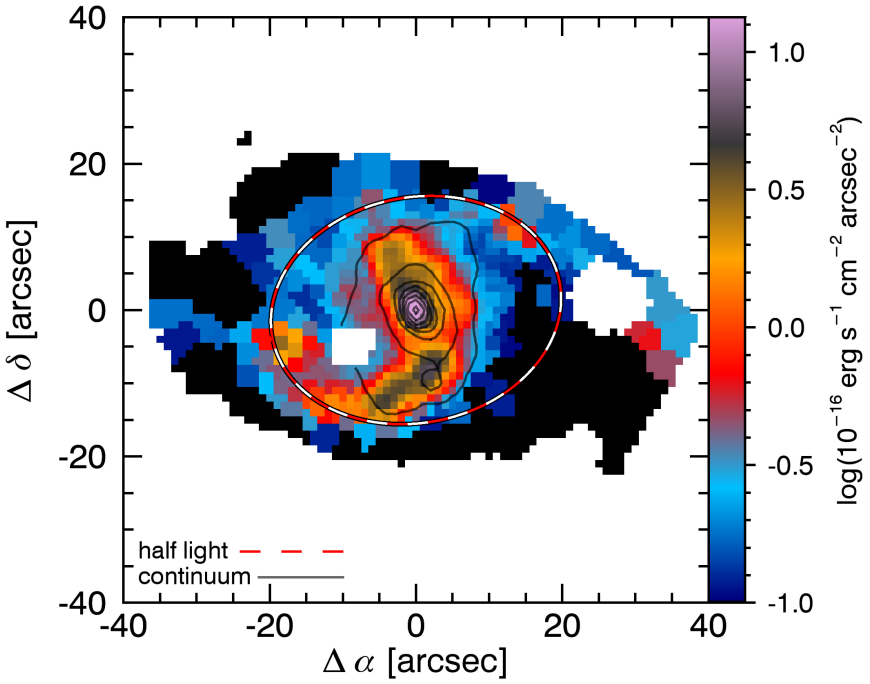

Figure 2.7: UGC11680 – **Hα emission line flux.** The highest intensity can be seen in the bulge, the star-forming near-side spiral-arm, and partially in the spiral arm on the far-side.

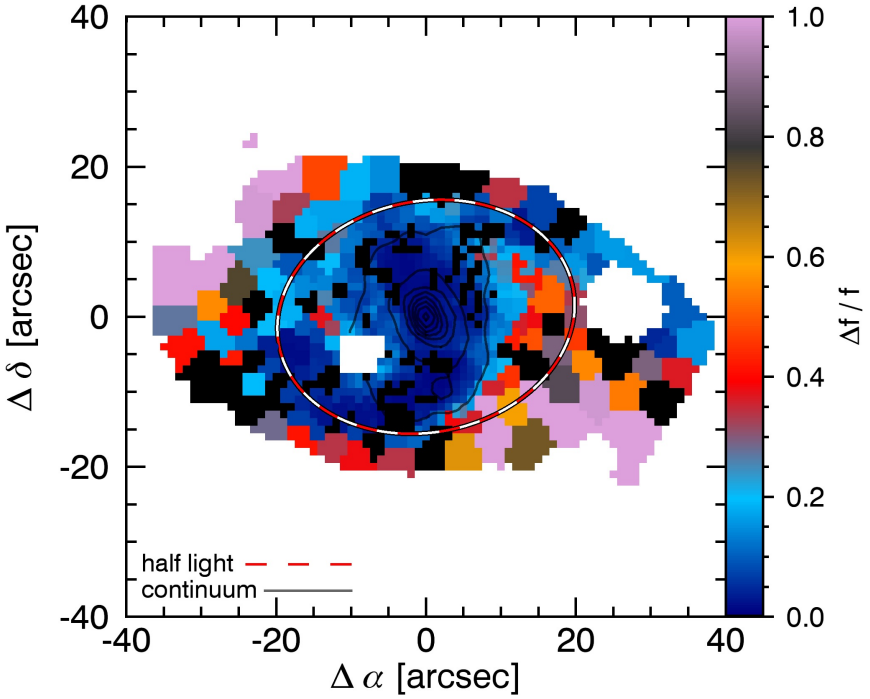

Figure 2.8: UGC11680 – **relative Hα flux error.** Most bins inside the half-light radius have a relatively low error. Bins towards the outskirts typically have larger measurement uncertainties.

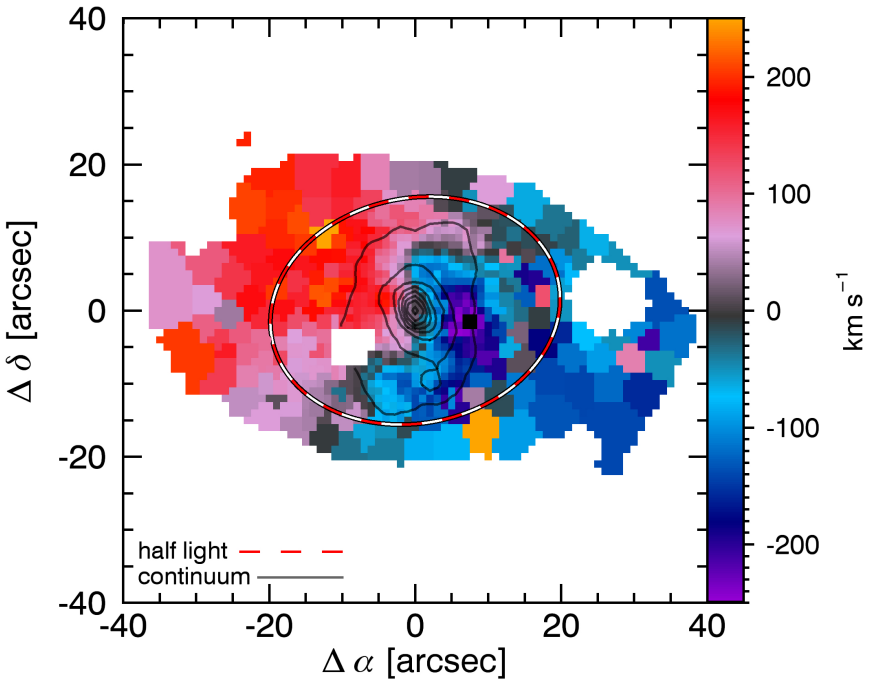

Figure 2.9: UGC11680 – **Hα velocity field.** This galaxy exhibits a regular and largely symmetric velocity pattern. The LOS velocities reach up to ~250 km s^{-1}.

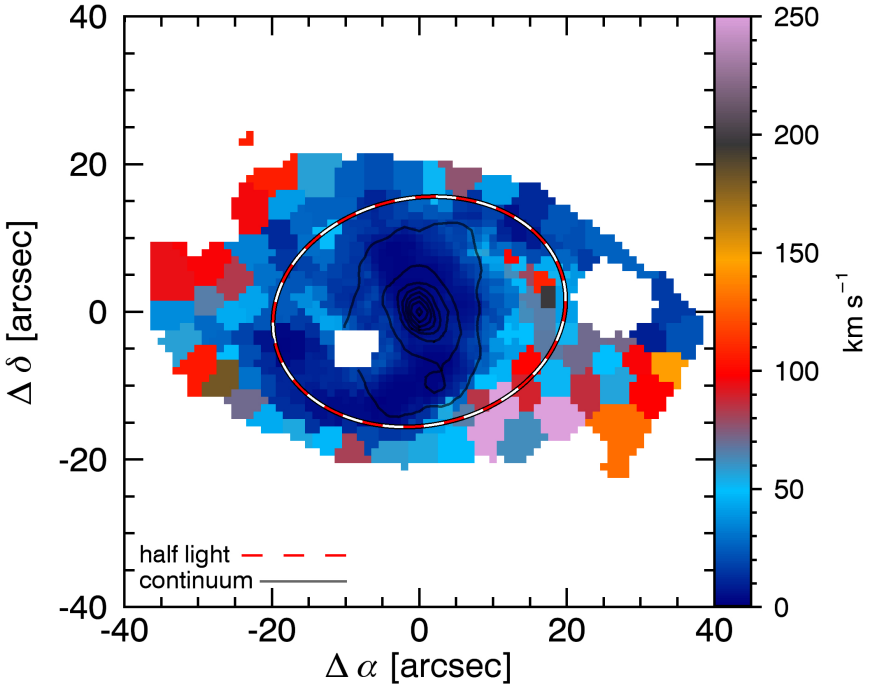

Figure 2.10: UGC11680 – **Hα velocity error.** Similarly to the flux measurement, errors increase as a function of radius.

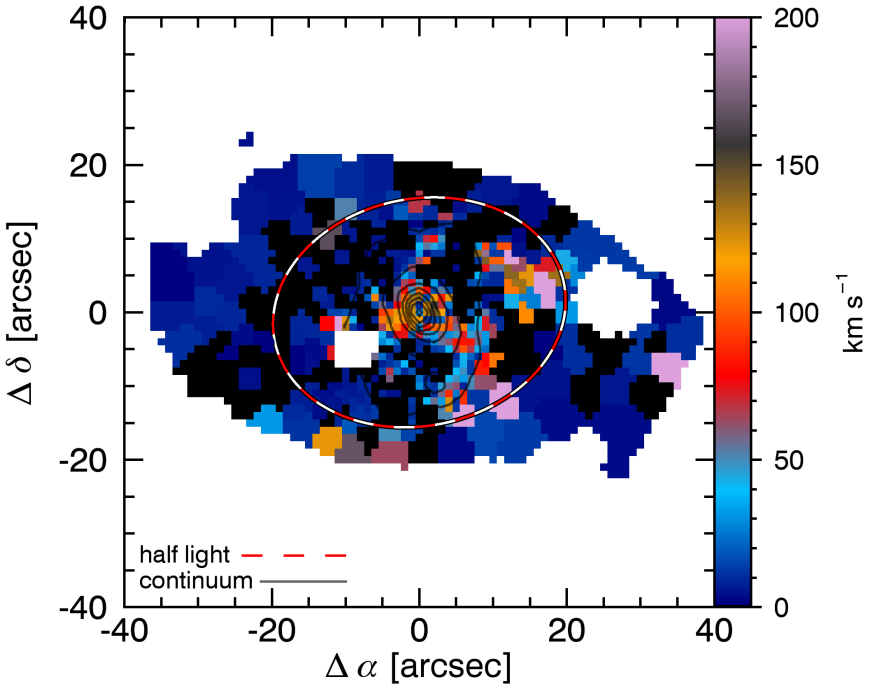

Figure 2.11: UGC11680 – **Hα velocity dispersion.** The vel. dispersion in this galaxy is negligible. The kinematics are, as seen in Figure 2.9, dominated by the rotational support.

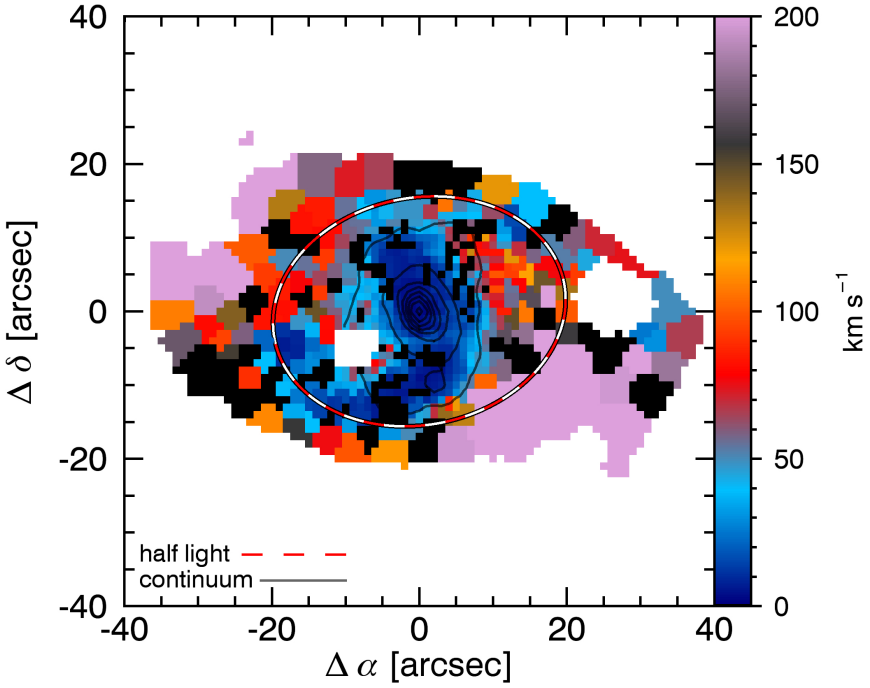

Figure 2.12: UGC11680 – **Hα velocity dispersion error.** The low spectral resolution V500 grating only yields reliable dispersion measurement in the inner parts of our galaxies.

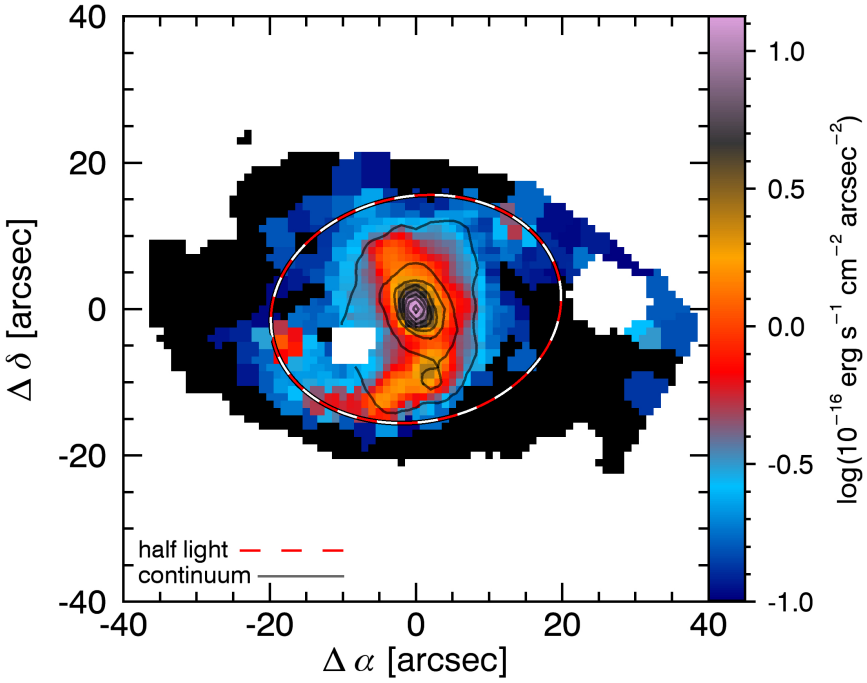

Figure 2.13: UGC11680 – **[NII]λ6583 flux.** Unsurprisingly, the gas distribution measured by the forbidden [NII] emission line is similar to Hα.

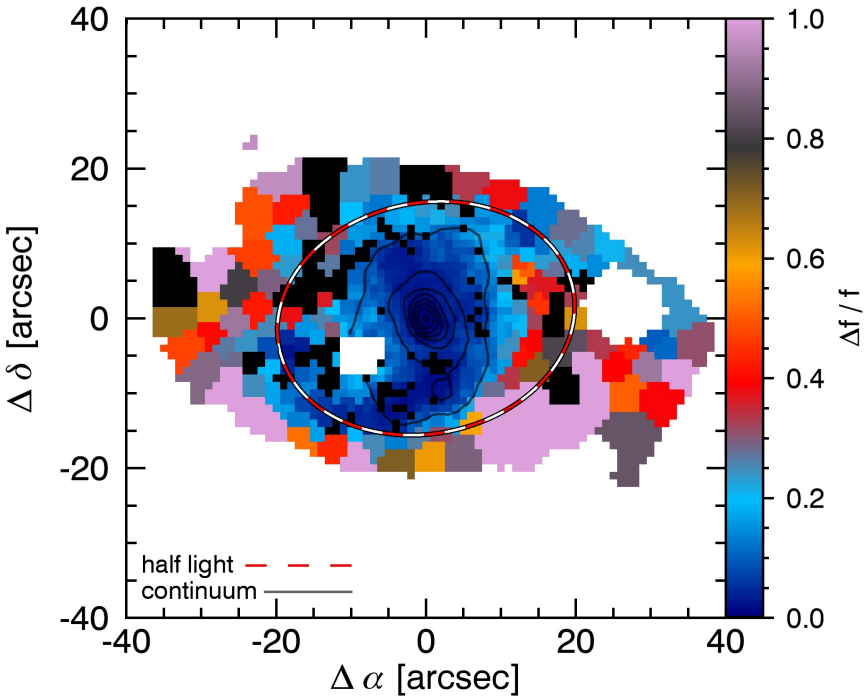

Figure 2.14: UGC11680 – **[NII]λ6583 relative flux error.**

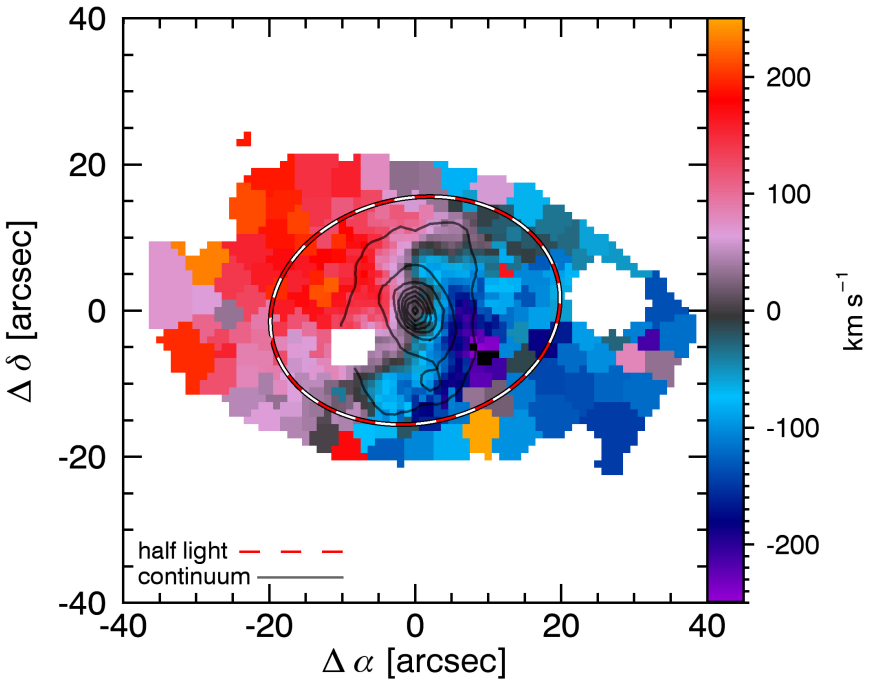

Figure 2.15: UGC11680 – **[NII]λ6583 velocity field.**

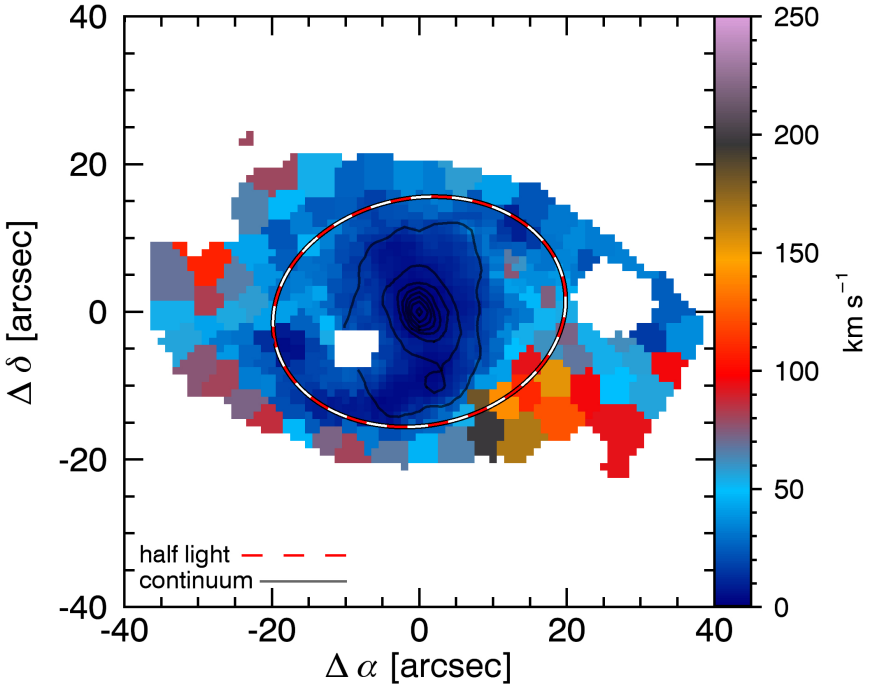

Figure 2.16: UGC11680 – **[NII]λ6583 velocity error.**

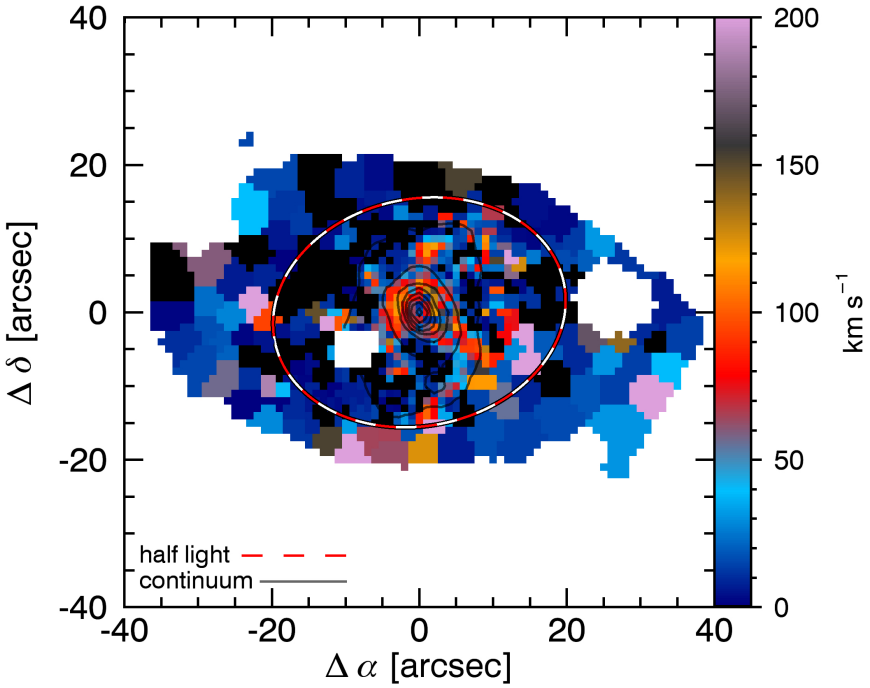

Figure 2.17: UGC11680 – **[NII]λ6583 velocity dispersion.**

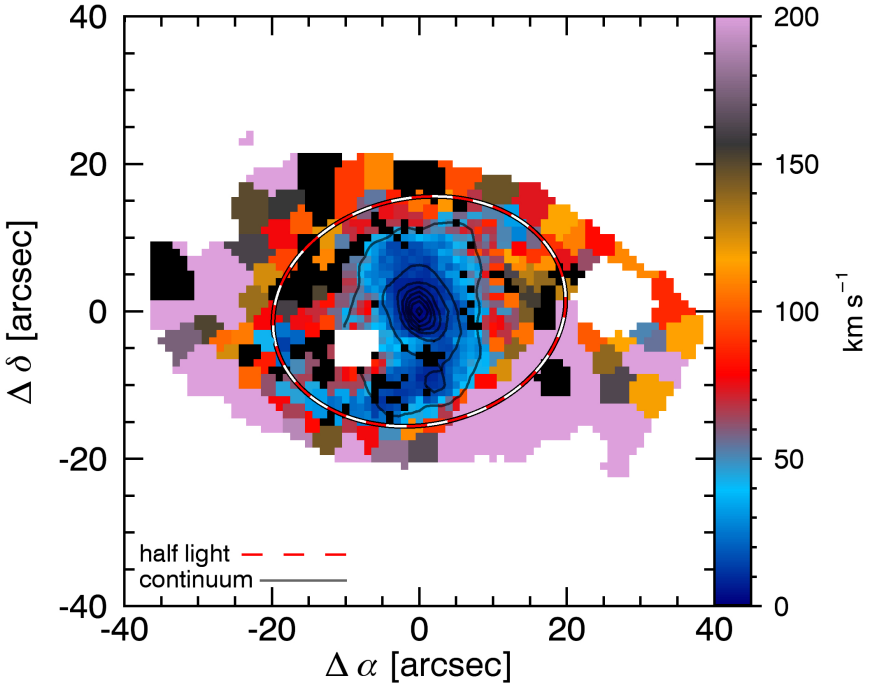

Figure 2.18: UGC11680 – **[NII]λ6583 vel. dispersion error.**

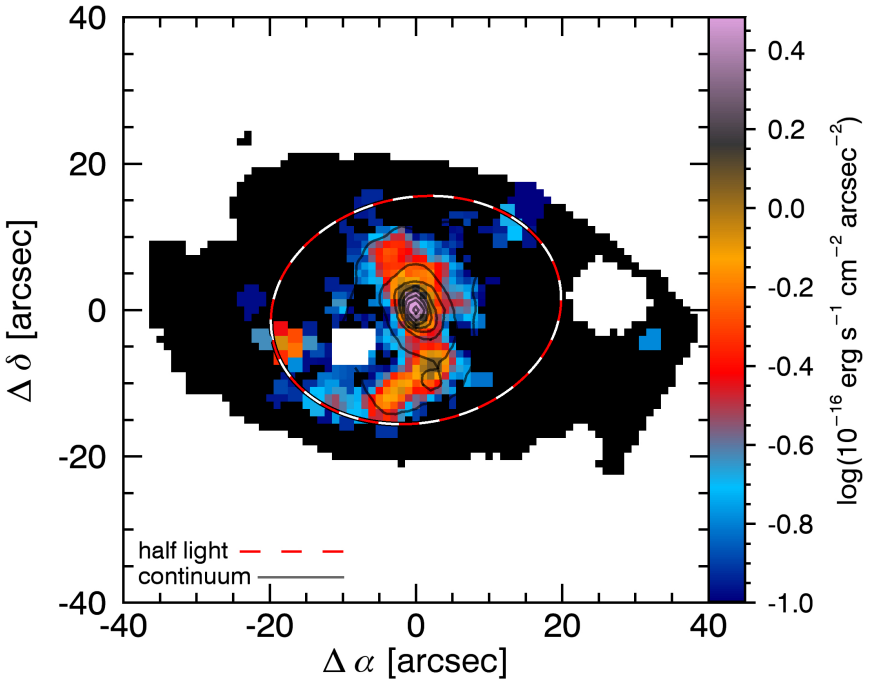

Figure 2.19: UGC11680 – **Hβ emission line flux.**

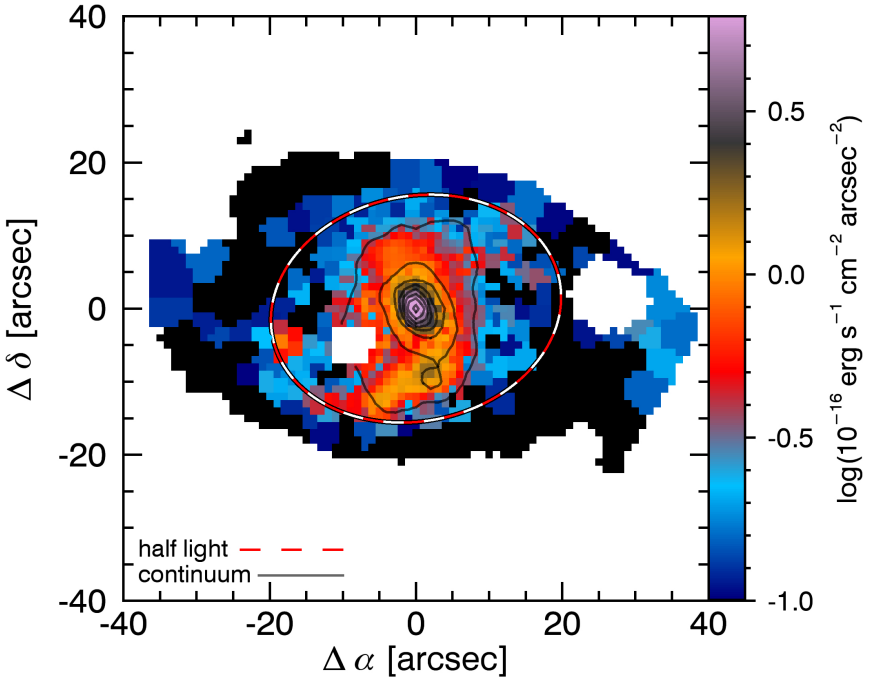

Figure 2.20: UGC11680 – **[SII] emission line flux.**

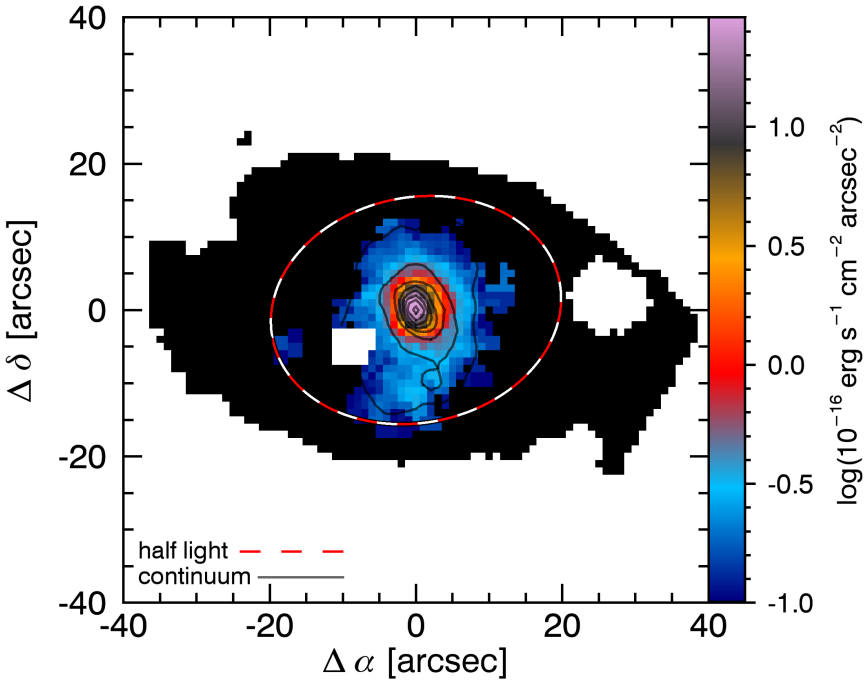

Figure 2.21: UGC11680 – **[OIII] emission line flux.**

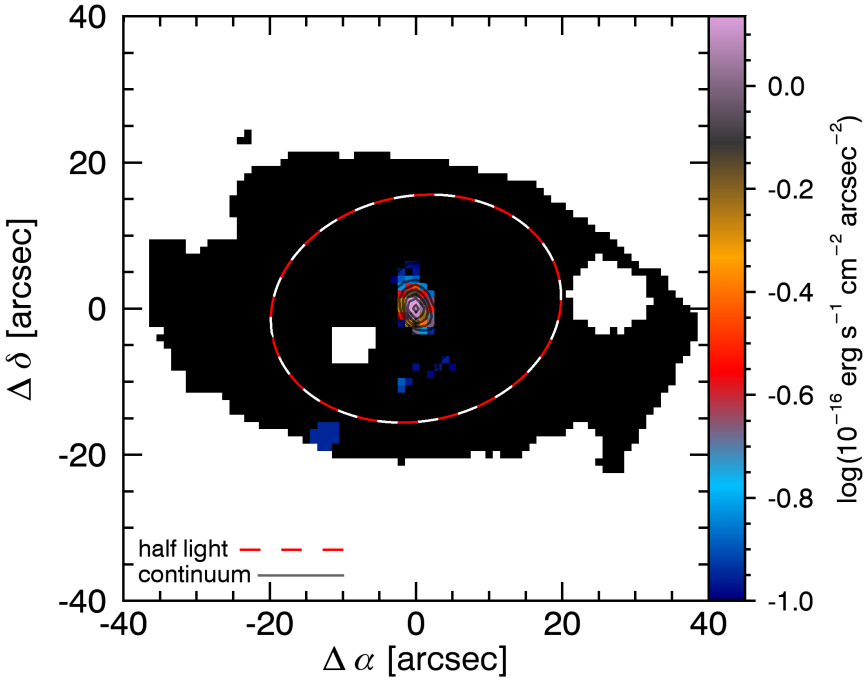

Figure 2.22: UGC11680 – **[OI] emission line flux.**

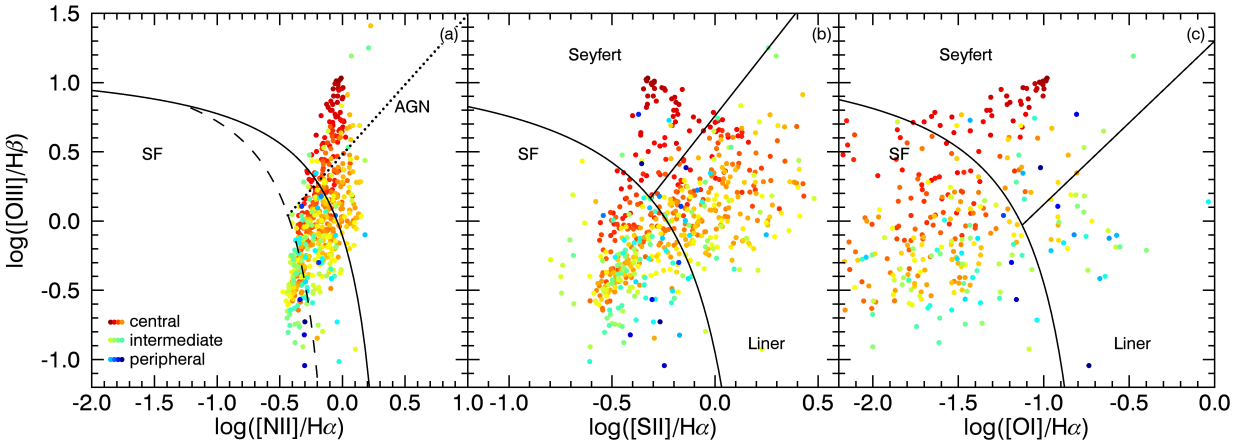

Figure 2.23: UGC11680 – **BPT diagram.** Data points are coloured by galactocentric radial distance and show emission line ratios of individual spaxels/bins of this galaxy. The galaxies centre is dominated by AGN/Seyfert signatures with high ionisation. The solid curved lines are the theoretically modelled "extreme starburst lines" (Kewley et al. 2001). The dashed line (Kauffmann et al. 2003c) and the dotted line (Cid Fernandes et al. 2010) in (a) and the straight solid lines (Kewley et al. 2006) in (b) and (c) are tracing a minimum in the central emission line ratio distribution of SDSS galaxies.

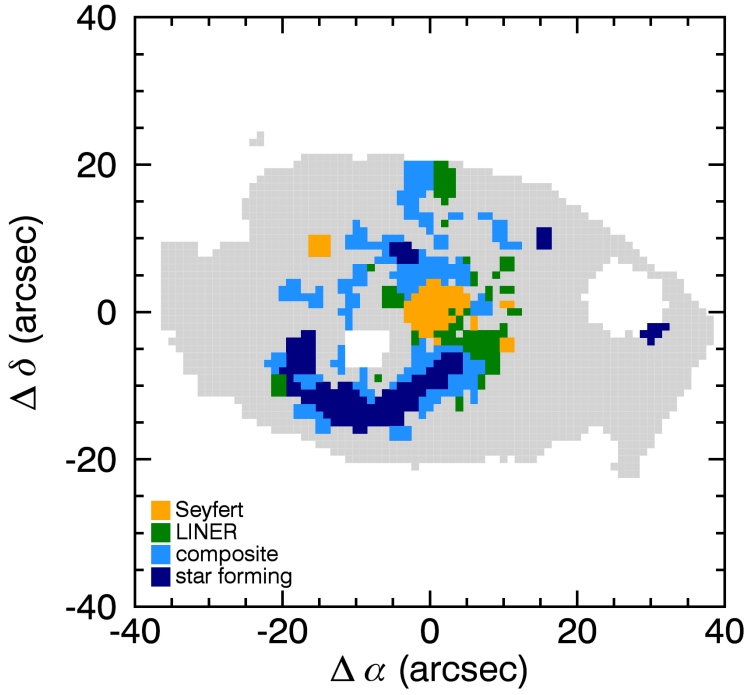

Figure 2.24: UGC11680 – **BPT map.** Two-dimensional representation of the BPT diagram (Figure 2.23). This map shows spatially the occurrence and distribution of the differently ionised regions. This galaxy in particular exhibits high ionisation Seyfert emission in the centre, followed by intermediate and star-forming regions along the spiral arms, and widely dispersed LINER-like emission.

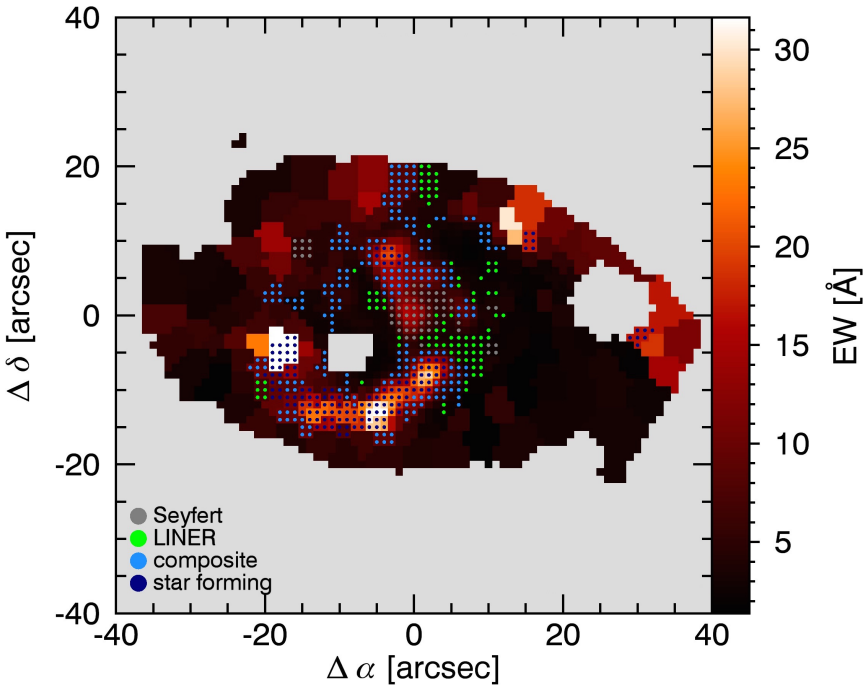

Figure 2.25: UGC11680 – **EW(Hα) map** with BPT overlay. Two-dimensional map of the equivalent width in Hα (EW(Hα)). It reveals a strong spatial correlation of LINER signatures occurring in regions of low EW(Hα) and star-formation occurring in regions with higher EW(Hα).

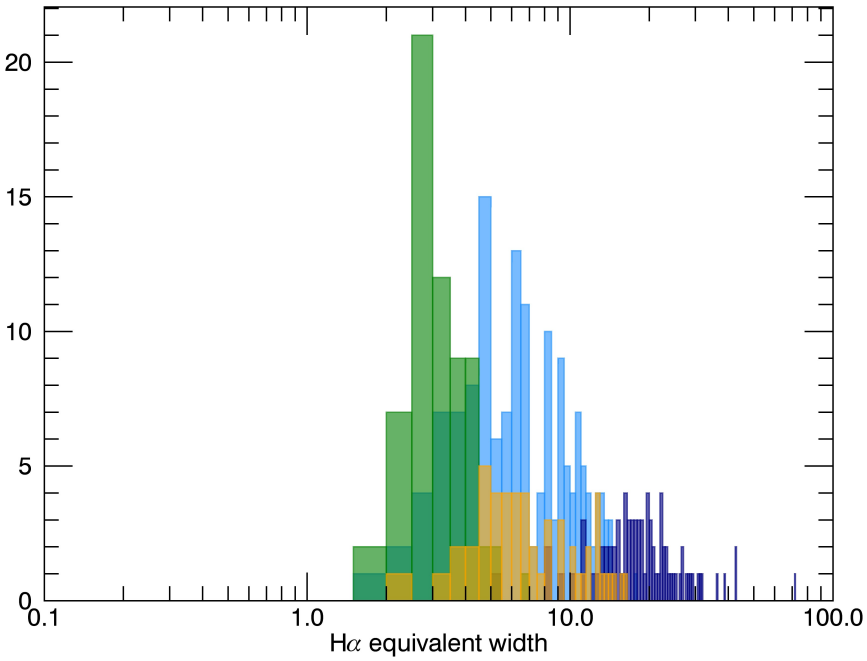

Figure 2.26: UGC11680 – **EW(Hα) histogram.** It visualises the separation of emission line regions with star-formation and LINER signatures. LINER-like regions are plotted in green, star-formation in blue, the Seyfert region in orange and intermediate regions in light-blue.

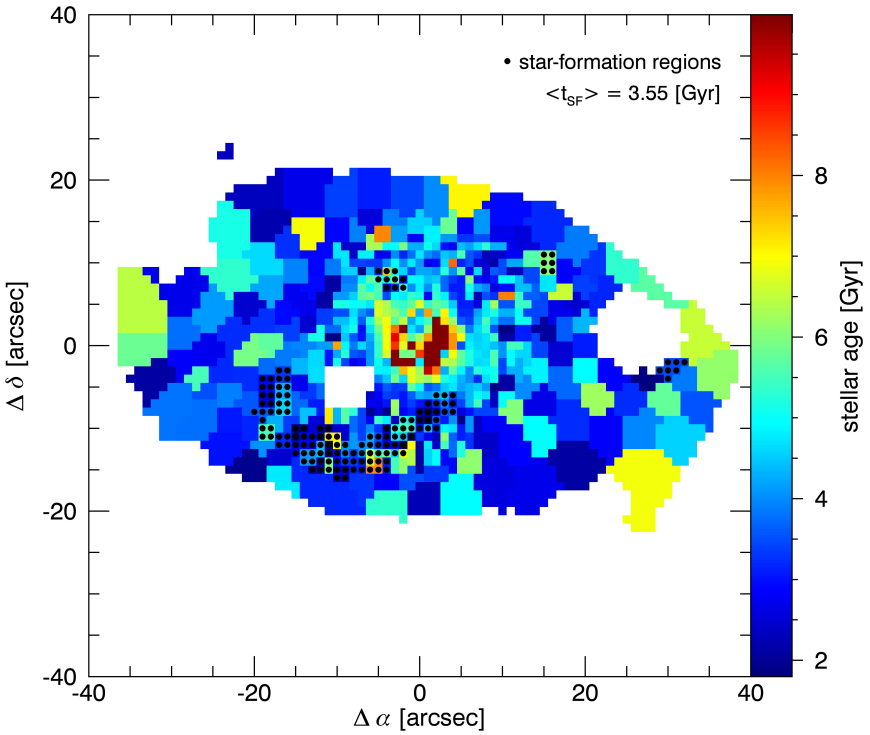

Figure 2.27: UGC11680 – **Stellar ages and star-forming regions.** The black dots indicate where regions of star-formation are on a light weighted stellar age map. The median age of star-forming regions in this galaxy is 3.55 Gyr.

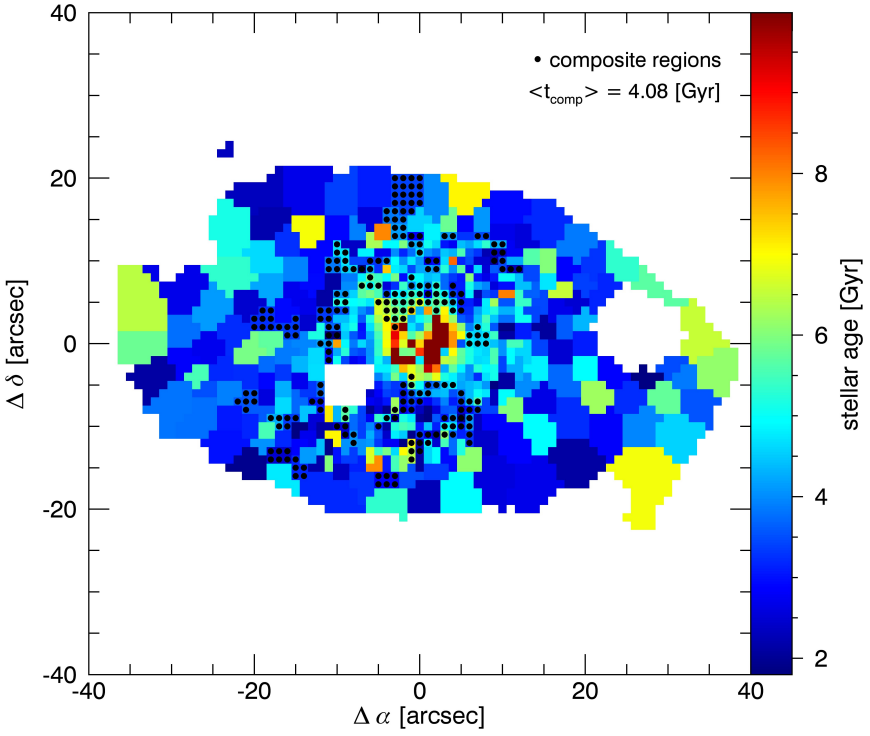

Figure 2.28: UGC11680 – **Stellar ages and composite regions.** The black dots indicate where regions of composite (also known as intermediate) emission are on a light weighted stellar age map. The median age of composite regions in this galaxy is 4.08 Gyr.

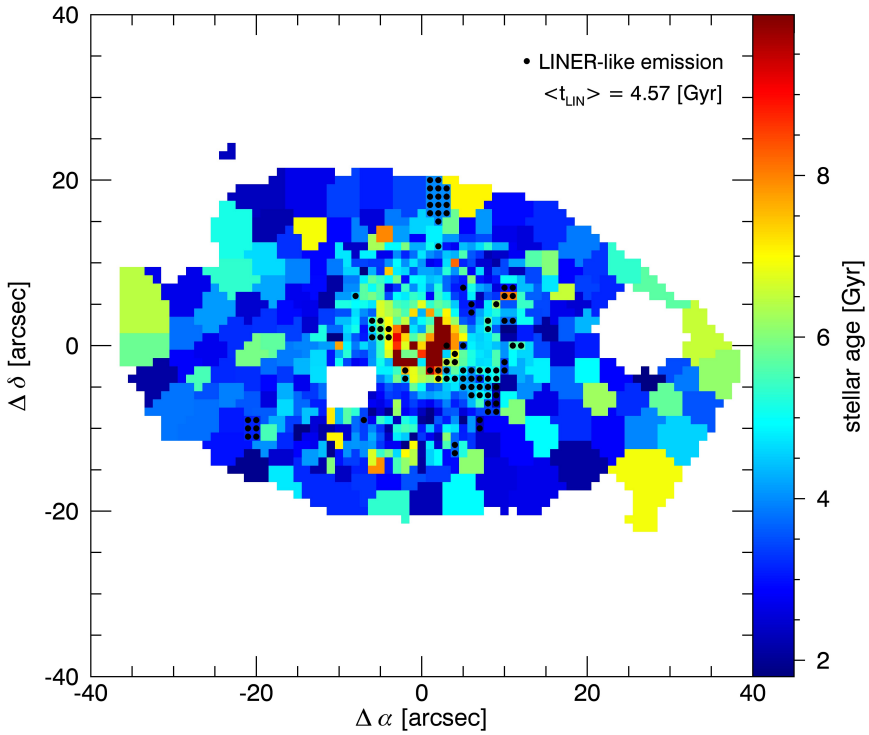

Figure 2.29: UGC11680 – **Stellar ages and LINER regions.** The black dots indicate locations with LINER-like emission on a light weighted stellar age map. The median age of regions with LINER-like emission in this galaxy is 4.57 Gyr.

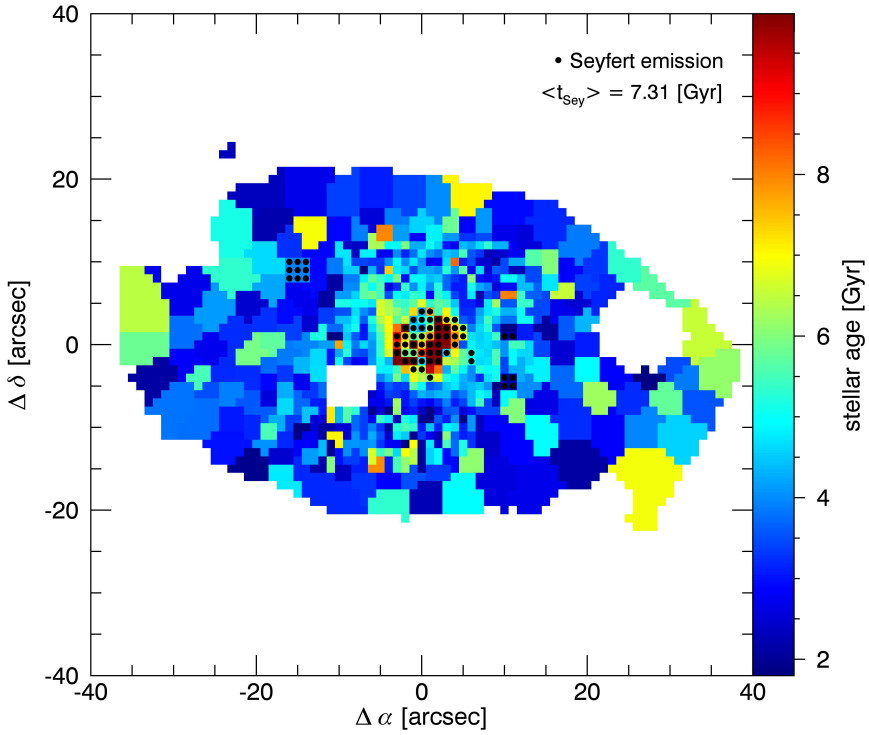

Figure 2.30: UGC11680 – **Stellar ages and Seyfert regions.** The black dots indicate where regions with Seyfert emission are on a light weighted stellar age map. The median age of Seyfert regions in this galaxy is 7.31 Gyr.

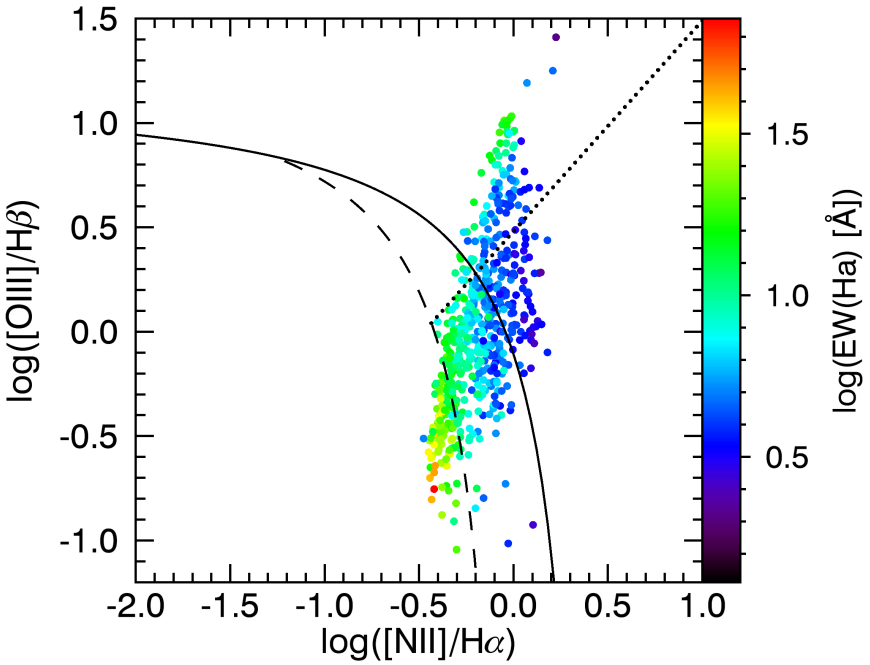

Figure 2.31: UGC11680 – **[OIII]/Hβ vs. [NII]/Hα vs. EW(Ha).** First panel of the BPT diagram from Figure 2.23. Data-points are coloured according to their equivalent width in Hα.

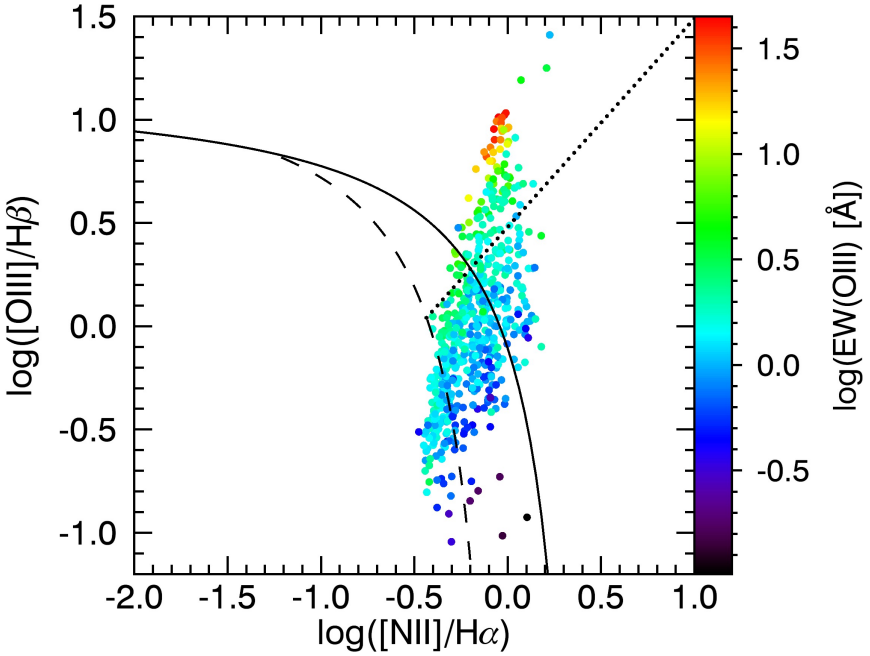

Figure 2.32: UGC11680 – **[OIII]/Hβ vs. [NII]/Hα vs. EW([OIII]).** First panel of the BPT diagram from Figure 2.23. Data-points are coloured according to their equivalent width in [OIII].

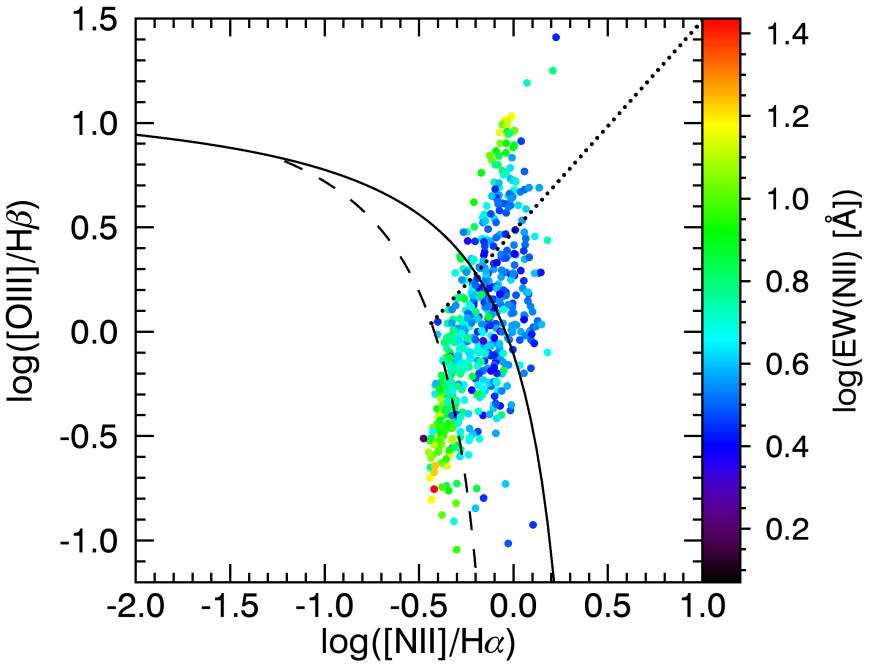

Figure 2.33: UGC11680 – **[OIII]/Hβ vs. [NII]/Hα vs. EW([NII]).** First panel of the BPT diagram from Figure 2.23. Data-points are coloured according to their equivalent width in [NII].

2.6 PUBLIC DATABASE

As a result of analysing the current number of 369 galaxies, we obtained the previously presented plots for each galaxy. Since many of those results and maps of individual galaxies can be interesting on their own, we created a public database and provide access to many of these secondary data products via the following link: www.mpia.de/3D/CALIFA.php.

This database contains the following items:

- starting with an SDSS image with a 5 kpc scale,
- flux maps for emission lines in: H$\alpha\lambda$6563 (Figure 2.7), H$\beta\lambda$4861 (2.19), [NII]λ6583 (2.13), [SII]$\lambda\lambda$6716,31 (2.20), [OIII]λ5007 (2.21), [OI]λ6300 (2.22),
- velocity and dispersion maps from the emission lines H$\alpha\lambda$6563 (2.9, 2.11), [NII]λ6583 (2.15, 2.17), and the stellar continuum from pPXF,
- error maps for flux, velocity and velocity dispersion in Hα (2.8, 2.10, 2.12) and [NII]λ6583 (2.14, 2.16, 2.18),
- the standard ionisation diagnostic BPT diagram (Figure 2.23),

- its corresponding BPT map (Figure 2.24),
- and a map of the equivalent width in Hα with a BTP classification overlay (Figure 2.25).

2.6.1 EXPLORING THE DATA

The database offers different options to search for specific items.

- We provide the list of our full sample in form of a table, where each galaxy is listed with the following parameters:
  - redshift,
  - line-of-sight velocity,
  - stellar mass,
  - ba (axes ratio) and,
  - Hubble type.
- Secondly one can select a specific *galaxy by* its *name*, which then leads to an overview pages of all available figures for the selected galaxy including a link to download the displayed data as compressed fits files. The fits files contain the following extensions:

  Extension 0: Ha flux
  Extension 1: Ha flux error
  Extension 2: Hb flux
  Extension 3: [NII]λ6583 flux
  Extension 4: [NII]λ6583 flux error
  Extension 5: [SII]$\lambda\lambda$6716,31 flux
  Extension 6: [OIII]λ5007 flux
  Extension 7: [OI]λ6300 flux
  Extension 8: Ha velocity
  Extension 9: Ha velocity error
  Extension 10: [NII]λ6583 velocity
  Extension 11: [NII]λ6583 velocity error
  Extension 12: Ha vel. dispersion
  Extension 13: Ha vel. dispersion error
  Extension 14: [NII]λ6583 vel. dispersion
  Extension 15: [NII]λ6583 vel. dispersion error

  All flux maps are in units of 10^{-16} erg s^{-1} cm^{-2} arcsec^{-2}. Velocity and dispersion maps in km s^{-1}.

- Selecting one *type of plot* from the second drop down menu, displays one specific aspect of all galaxies. One can, for example, view and compare the Hα velocity maps of all galaxies, while only being one click away from looking at the other plots on the overview page.

We tried to assure a high data quality and applied a signal to noise threshold of 20, measured in the continuum, to ensure that our results are only minimally, if at all, affected by erroneous fits and misclassified spaxels. As an additional constraint, the relative error in emission line ratio has to be below 50%. Error maps are provided for emission line flux and kinematics of Hα and [NII]λ6583, other data products e.g. BPT maps, do not come with measurement uncertainties but include the above mentioned constraints.

3 The LINER – AGN discrepancy

3.1 Spatially resolved LINER-like emission

Among the first 257 galaxies observed within the CALIFA survey, we found 48 LINER galaxies based on their measured central emission line ratios, covering a 3" diameter aperture. These galaxies cover almost all morphological types based on the averages of five independent visual classifications of SDSS r and i band images. Based on the ionisation strength and hence the underlying ionisation source, the so-called BPT diagram (Baldwin et al. 1981) is an empirically derived diagnostic tool to distinguish between star formation (dominated by Balmer Hα and Hβ lines), Seyfert galaxies (with high ionisation potential) and LINER galaxies (with low ionisation lines).

As shown by this diagnostic diagram in Figure 3.1, the flux in the lower-ionisation lines [NII]λ6583, [SII]$\lambda\lambda$6716,31 and [OI]λ6300 when compared to H$\alpha\lambda$6563 is too high for ionisation by young massive stars, and at the same time, the flux in [OIII]λ5007 when compared to H$\beta\lambda$4861 is too low for ionisation around a typical Seyfert-like medium-luminosity AGN. The emission lines that are combined in the ratios are close in wavelength; therefore, attenuation by dust cancels out, leaving the galaxies to be classified as LINERs.

Subsequently, we measured emission line ratios in different regions across the galaxy for each of these LINER galaxies. Even the weak emission lines can be robustly recovered as we are simultaneously fitting the stellar continuum and emission lines, while requiring a minimum signal-to-noise of 10 per pixel; in the outer parts we combine spectra from neighbouring regions to reach this minimum signal-to-noise. As illustrated for three example galaxies in Figure 3.2, we can then place all regions with reliable measured line ratios on the BPT diagrams and classify each

*This chapter is adapted from Singh et al. (2013)

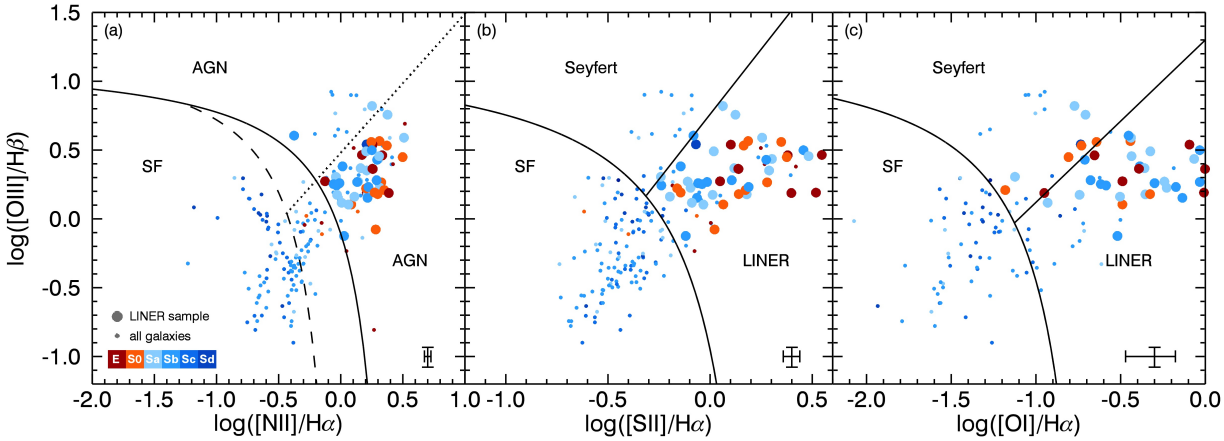

Figure 3.1: Selection of LINER galaxies. Data points are coloured by Hubble type and show central emission line ratios of 257 CALIFA galaxies on the BPT diagram. Those classified as AGN in (a) and LINER in (b) have larger symbol sizes and are selected for further analysis. Small symbol sizes in the LINER region may appear due to either an inconsistent BPT classification, this typically affects points near the demarcation lines, which are either LINERs in (b) but not AGN in (a), vice versa, or objects that have had the central measurement detect only one of either [NII] or [SII] emission lines. Panel (c) is shown for illustration but not used in the classification due to the larger relative error indicated in the lower right corner of each panel. The solid curves are the theoretically modelled "extreme starburst line" (Kewley et al. 2001). The dashed curve (Kauffmann et al. 2003c) and the dotted line (Cid Fernandes et al. 2010) in (a) and the solid lines (Kewley et al. 2006) in (b) and (c) are tracing a minimum in the central emission line ratio distribution of SDSS galaxies.

of them. Next, we can colour-code all regions across the galaxy according to this classification to obtain BPT maps. This map reveals which parts of the galaxy are dominated by star-formation-like emission (typically in the outer parts and/or in spiral arms), Seyfert-like emission (restricted to the centre), or LINER-like emission (typically extended well beyond the nucleus).

Finally, we select only those regions with LINER-like emission and plot the measured Hα surface brightness – or that of any other emission line – versus the distance of each region from the galaxy centre. After normalising the central Hα flux to unity for all galaxies, we arrive at the (smoothed) coloured radial profiles in Figure 3.3. The expected profile from central point-source illumination is plotted in black.

There is a strong gap between the latter predicted point-source-illumination profile and the actual observed profiles,which increase to $\gtrsim$ 1 dex toward the $\sim$ 30" radial extent of our data. In some regions, part of the emission can be the result of a superposition of different ionising flux sources. In Section 3.2, we describe tests, which assure that the discrepancy between data and the null hypothesis model is not due to this contribution. These tests show that the results are not affected by a potential contribution to the line flux triggered by young stars.

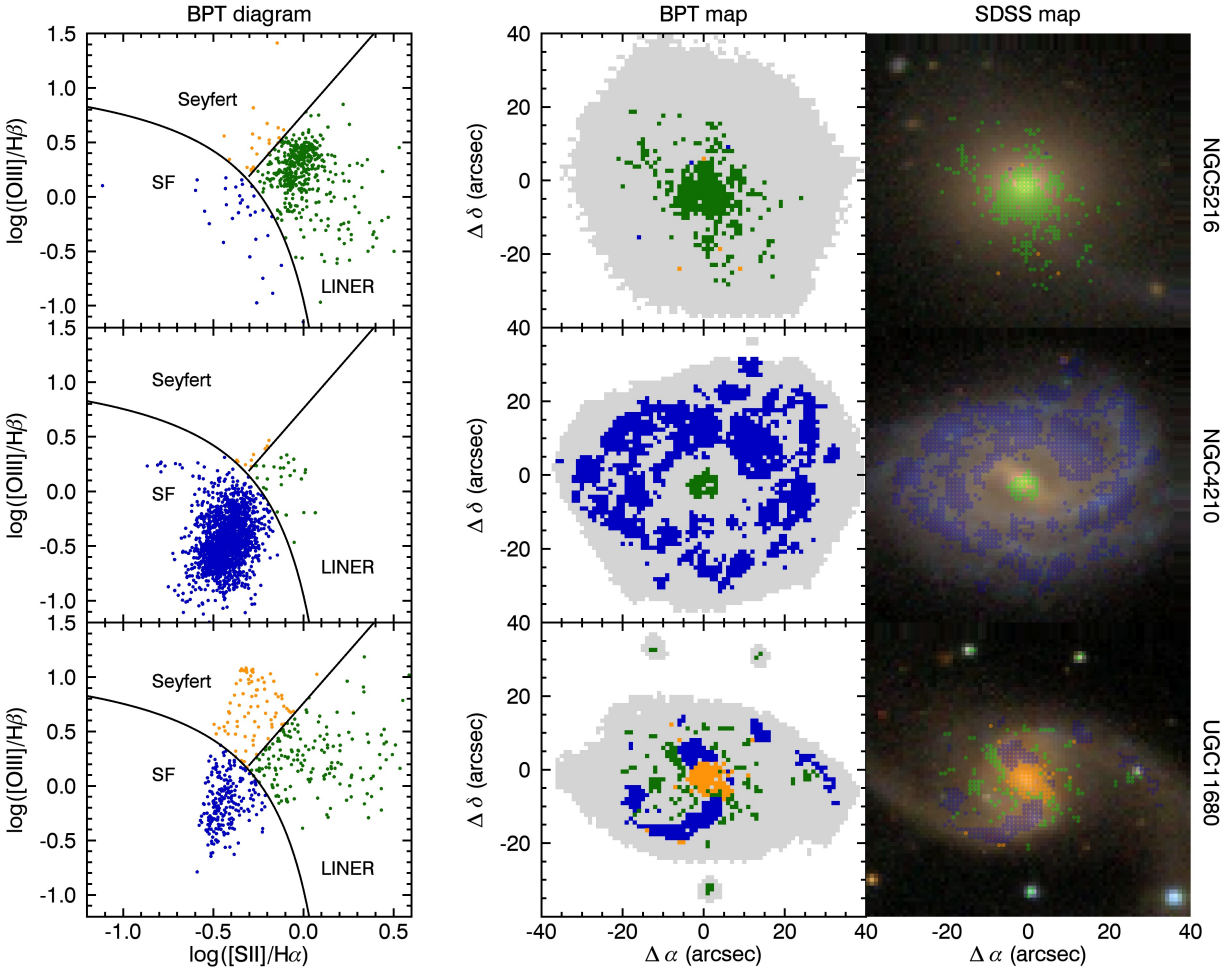

Figure 3.2: Emission line ratio classification of spatial regions. The distribution of measured emission line ratios in a BPT-diagram (left column) and spatially across the galaxy (middle column, usable data regions in grey) differ between example galaxies dominated by LINER-like emission (NGC 5216, top row), a galaxy dominated by star-formation (NGC 4210, middle row) and an AGN in a spiral host (UGC 11680, bottom row). The latter one is shown as an example but not part of our sample. Regions are colour-coded according to their position in the BPT diagram: green for LINER-like, orange for Seyfert-like, and blue for star-formation-like emission line ratios. Overlay of these regions onto the colour-composite image from the SDSS (right column) reveals how LINER-like emission is spatially extended, except when dominated by Seyfert-like emission in the centre or by star-formation-like emission in spiral arms or the disk.

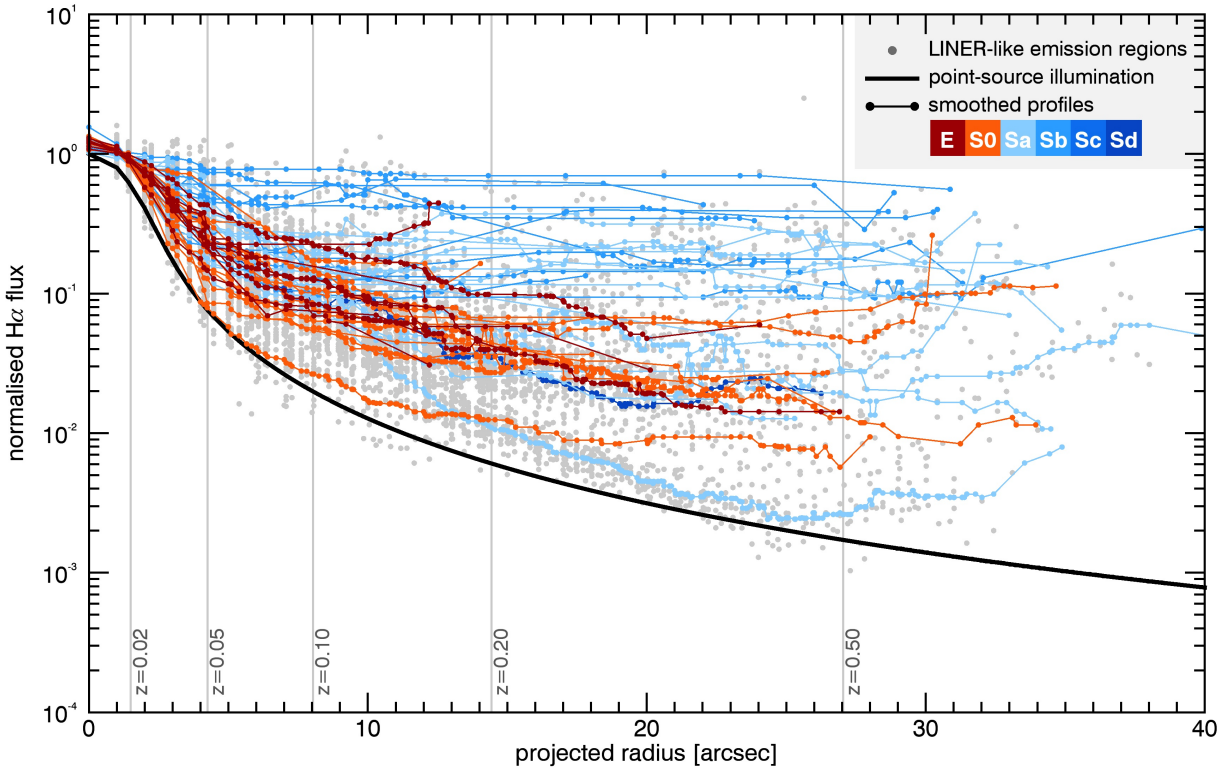

Figure 3.3: Radial profiles of LINER-ionised Hα flux. The coloured curves are normalised and smoothed radial surface brightness profiles of the Hα emission line flux from our 48 LINER galaxies and compared to a PSF convolved point-source illumination $1/r^2$-profile in black. All profiles are normalised with respect to the central flux inside a 1.″5 radius aperture. Different colours represent different morphological types ranging from round elliptical galaxies (dark red) to disk-dominated spiral galaxies (dark blue), with lighter colours in-between. Beyond the inner few arcsec for LINER galaxies of all types, there is a significant excess, with up to two orders of magnitude, above the prediction from a point-source ionisation. The vertical grey lines illustrate the radial extent covered by a 3"-diameter SDSS aperture when the CALIFA galaxies with $\bar{z} = 0.017 \pm 0.006$ would be placed at the indicated higher redshifts.

The vertical grey lines in Figure 3.3 illustrate the radial extent covered by a 3"-diameter SDSS aperture, if the CALIFA galaxies with an average redshift of 0.017 ± 0.006 would be placed at the indicated higher redshifts. This illustrates that SDSS emission line classifications can be non-unique and dependant on redshift, meaning that for example NGC 4210 from Figure 3.2 could be classified as a either star-forming or LINER galaxy, depending on its distance and hence, apparent size. In addition, we tested against projection effects for the disk-dominated galaxies in our sample, which affects both radius coordinates and flux densities. After these tests the discrepancy between observed radial line surface brightness profiles and the null hypothesis remains for both early- and late-type galaxies, hence rejecting the model that a central AGN is causing the spatially extended LINER-like emission.

3.2 VERIFYING THE ROBUSTNESS OF THE ANALYSIS

Below, we discuss various effects that could influence our results and verify that our findings are robust against them.

3.2.1 ROBUSTNESS OF WEAK EMISSION LINE EXTRACTION

A central technical part of this work is the extraction of weak emission lines in the presence of a stellar continuum. Since the equivalent width of the lines is often low, specifically with the Balmer Hβ line being superposed on an absorption trough, an unbiased extraction is the core of the present analysis.

We have employed three different procedures for line extraction. All avoid to model the line flux after a previous subtraction of the stellar continuum. Instead, continuum and line emission are modelled simultaneously, which provides the least-biased line measurement (Sarzi et al. 2006). To assess whether systematics in the line measurement are present and whether the uncertainties on line fluxes – and hence line ratios – are properly derived, we compared the extracted line fluxes and errors from the following complementary approaches:

(a) We use the gas and absorption line fitting procedure GANDALF (Sarzi et al. 2006) with the MILES (Sánchez-Blázquez et al. 2006; Falcón-Barroso et al. 2011) library of stellar templates. In this case, the best fit to a spectrum is the superposition of an optimal combination of the stellar templates with additional Gaussians representing the emission lines. Unfortunately, the GANDALF routine only computes errors for those emission lines that are unrestricted in their kinematical properties. Emission lines that are being tied to another line in either velocity or velocity dispersion are better recovered (Sarzi et al. 2006) but do not come with errors for the measured fluxes.

(b) Same as (a) but we used the MILES library of single stellar populations (SSP) instead of the MILES stellar template library.

(c) To acquire flux errors for all emission lines of interest, we employed a Monte Carlo simulation, perturbing the input spectrum one hundred times. This amount of different realisations is sufficient to create a Gaussian distribution in extracted fluxes from which we take the mean and standard deviation as measured flux and error value. To make this process computationally feasible, we use the best-fit composite stellar spectrum from a previous emission line masked stellar continuum fit with the procedure PPXF (Cappellari & Emsellem 2004) instead of the full template library.

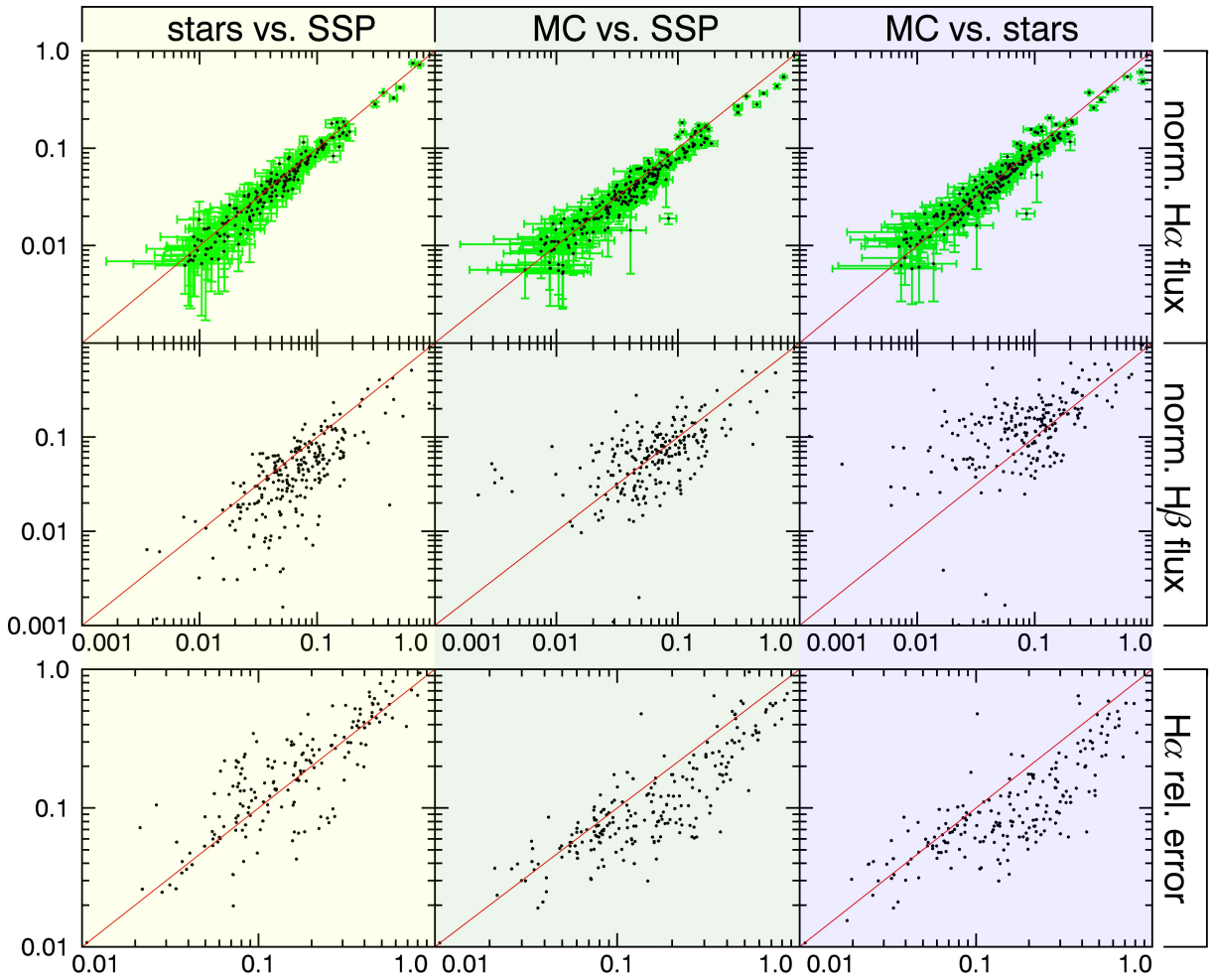

Figure 3.4: Comparison of extracted Hα fluxes, Hβ fluxes and estimated errors for the Hα line of NGC 5614, as extracted by Gandalf using the MILES stellar template library, the SSP library and a Monte Carlo variation of noise in the spectra. There is a very good match in the line fluxes between the three methods for the Hα line (row 1), while the errors estimated by Gandalf are larger than the statistical variance from the Monte Carlo approach (row 3). The weak Hβ line is generally better recovered using either the Monte Carlo or GANDALF/SSP method (row 2).

The example in Figure 3.4 compares the resulting fluxes and errors for the Hα and Hβ line of NGC 5614. There is no systematic difference in flux extraction between the three methods also at the faint end with a scatter within each method's uncertainty. The χ^2-based error from GANDALF, most likely due to unaccounted small pixel-to-pixel systematics and correlations, are larger than the robust Monte Carlo measurements. We verified that even if the Monte Carlo errors happened to be underestimated our results are unchanged, and we conclude that the line flux properties are accurately measured, down to the faintest end.

3.2.2 POINT SOURCE RADIATION TO RADIAL FLUX PROFILE

The radiation field from a central point source like an AGN declines with the inverse of the radial distance $\propto 1/r^2$. In the case that the photo-ionised gas is optically thin and distributed in an infinitesimally thin disk with a constant filling factor and constant density, the resulting observed emission line flux also falls off inversely squared with (projected) radius $\propto 1/R^2$.

The fall-off is even faster when the gas is not optically thin and part of the ionisation gets absorbed by intervening gas (clouds). Similarly, a radially decreasing filling factor results in a faster decline, whereas the opposite of an increase would require very special conditions. With perhaps the exception of strongly interacting galaxies, the gas density in galaxies is normally radially decreasing (Bigiel & Blitz 2012), so that the flux is also expected to drop at an even faster gradient than inverse square in this case. Only in the case that the thin-disk assumption is strongly invalidated do we expect the opposite effect of a decline shallower than $\propto 1/R^2$ – in the extreme case of optically thin gas with a constant filling factor and constant density in a spherical distribution, the line-of-sight integral results in an observed emission line flux that will fall off inversely linear with projected radius.

However, the resulting kinematics in all types of galaxies with (ionised) gas present shows clear disk-like rotation, apart from disturbances due to non-axisymmetric structures (bars and spiral arms) and tidal interactions (e.g., Garcia-Lorenzo et al. 2014). The resulting angular momentum implies that the gas always settles in a disk, which, however, can have a substantial thickness. After line-of-sight integration, the latter thickness still results in a slightly slower fall-off than the inverse square, but the radially declining gas density typically compensates for this.

We illustrate the latter by a simple model in which a central point source ionises optically thin gas with a constant filling factor distributed in an axisymmetric disk viewed at an inclination angle $i = 60°$ (with $i = 0°$ face-on and $i = 90°$ edge-on). Combined neutral and molecular hydrogen measurements in nearby galaxies show that the gas density declines exponentially

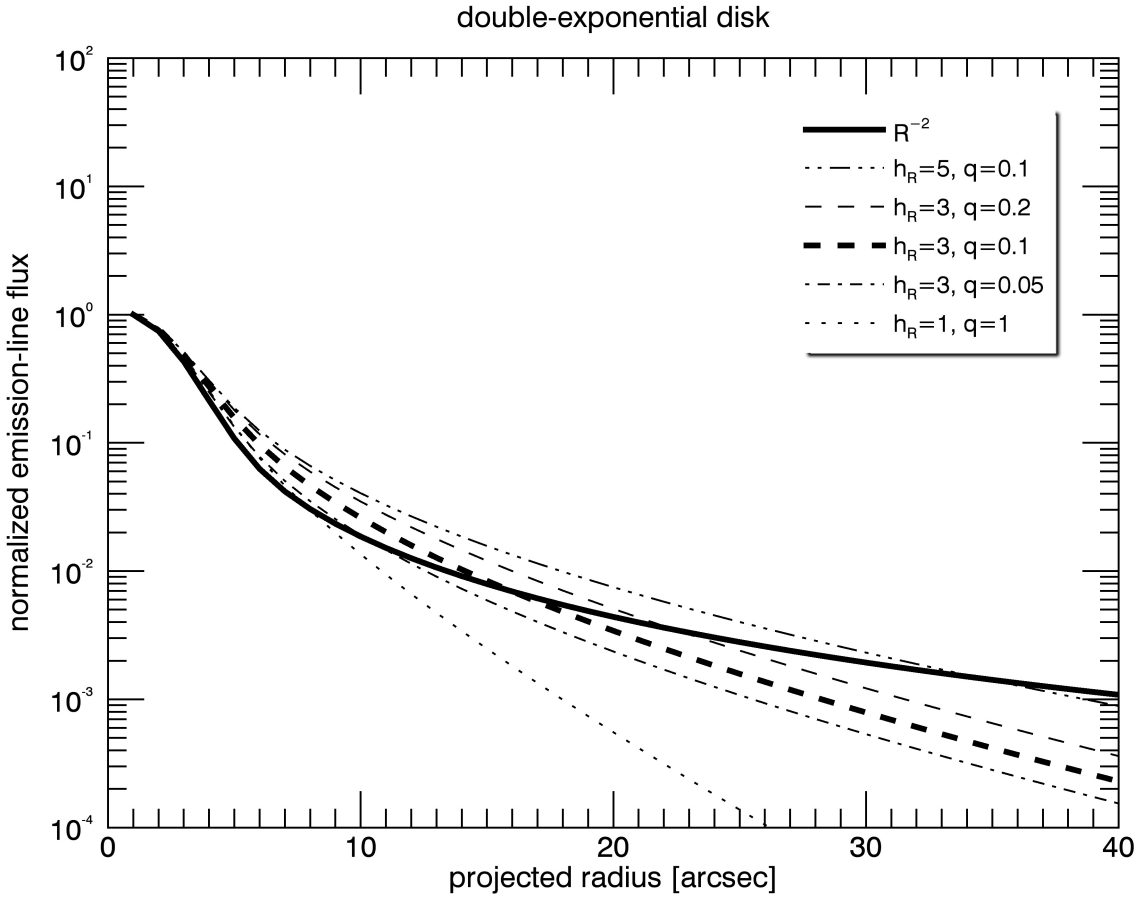

Figure 3.5: Normalised flux profiles as a function of projected radius R of gas being ionised by a central point source. The thick solid curve assumes that the gas is optically thin and distributed in an infinitesimally thin disk with a constant filling factor and constant density, so that the fall-off is the same inversely squared with radius as the point-source radiation. The thick dashed curve is when the gas is distributed in an axisymmetric disk of finite thickness with gas density both radially and vertically declining exponentially as $\propto \exp[-R/h_R]\exp[-|z|/(q\,h_R)]$ with fiducial values for the scale length of $h_R = 3\,\mathrm{kpc}$ and for the flattening of $q = 0.1$, viewed at an inclination angle of $i = 60°$. The thin long/short dashed curves show the effect of a factor of two thicker/thinner disk, the dash-dotted curve is for when the scale length is much larger, and the dotted curve is when the gas distribution is spherical and more centrally concentrated.

in radius (Bigiel & Blitz 2012) and that the vertical fall-off is typically well matched by an exponential as well. Henceforth, we adopt a double-exponential for the gas density

$$\rho_{gas} \propto \exp\left[\frac{-R}{h_R}\right] \exp\left[\frac{-|z|}{(q\, h_R)}\right] \tag{3.1}$$

with fiducial values for the scale length of $h_R = 3\,\mathrm{kpc}$ and for the flattening of $q = 0.1$. The resulting flux profile is shown in Figure 3.5 as the thick dashed curve, whereas the thin long/short dashed curves show the effect of a factor two thicker/thinner disk. The differences with respect to the $1/R^2$ fall-off (thick solid curve) are much smaller than the offset from the on average, much shallower observed flux profiles shown in Figure 3.3. The same holds true for a thin disk ($q = 0.1$) with a much larger scale length ($h_R = 5\,\mathrm{kpc}$), as indicated by the dash-dotted curve, or a spherical ($q = 1$) and more centrally concentrated ($h_R = 1\,\mathrm{kpc}$) gas distribution, represented by the dotted curve.

3.2.3 IMPACT OF GEOMETRIC PROJECTIONS

Even if the disks of galaxies are intrinsically round, the inclination at which we observe them results in projection effects that act both on the minor axis radius coordinate and the effective gas density and hence, line emitting region. Under the assumption of a geometrically thin gas distribution, a proper de-projected radius would be described by

$$R_{de} = \sqrt{R_a^2 + \left(\frac{R_b}{\cos i}\right)^2} \tag{3.2}$$

with a major-axis radius component R_a, observed minor axis component R_b, and inclination angle i. The gas distribution itself, on the other hand, would be projected by the same amount as the minor axis component, $\cos i$.

Hence, the observed projected profiles have all data points moved to smaller observed radii by different amounts, while the flux density is moved to higher values. To assess whether this produces a significant net increase or decrease of the difference between observations and models as seen in Figure 3.3, a tentative and maximal de-projection of all disk-dominated galaxies in our sample was carried out for illustrative purposes, as shown in Figure 3.6.

For this calculation, we adopted

$$\cos i = 1 - \epsilon \tag{3.3}$$

for a thin disk with observed ellipticity ϵ that is derived from an isophotal analysis of the SDSS images.

As can be seen, the impact on the discrepancy model–observations is at most small, and it can be concluded that projection effects play no significant role in the interpretation.

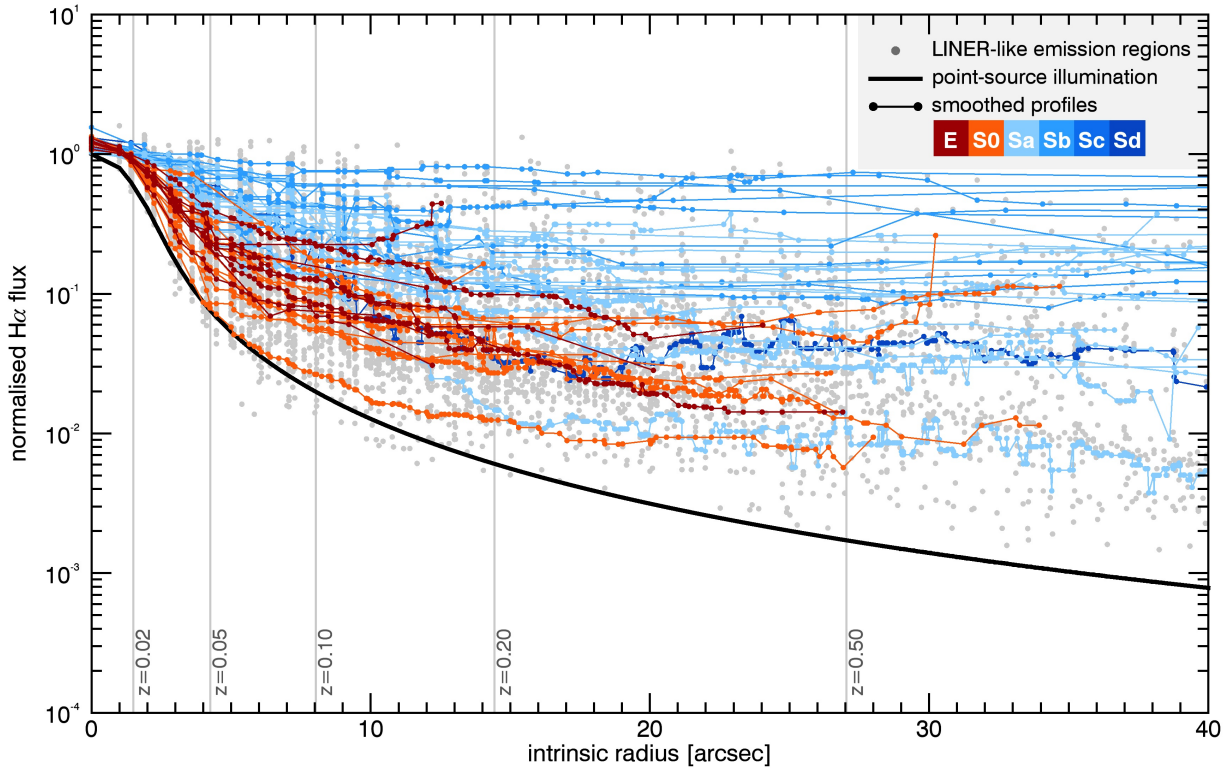

Figure 3.6: De-projection of radial Hα surface brightness profiles. To demonstrate how strongly potential projection effects of galaxy inclination could impact our results, all disk-dominated galaxies of the sample were subjected to a maximal geometrical de-projection. For this test, it was assumed that these galaxies were infinitely thin disks and that observed ellipticities were fully due to an inclination of the disk with respect to the observer's line of sight. Both radius and gas surface density projection were considered. The comparison to Figure 3.3 shows a stretch of the radius axis for some objects, but neither qualitative nor quantitative difference in surface brightness excess for the galaxies over the point-source line is shown.

3.2.4 Impact of mixed-in star formation contribution

A selection of spaxels in a BPT diagram above the theoretical upper limit of where star formation alone can produce given line ratios does not preclude a significant contribution to the line emission from star formation (SF). In principle, a mix of a fiducial "pure LINER" with a "pure SF" ionising radiation field, can lead to substantial SF contribution to the emission line flux outside the classical SF region. Given that early-type galaxies with negligible SF show similarly shallow flux profiles as late-type galaxies with significant SF (Figure 3.3), this result already hints that mixed-in SF contributions cannot be the source of the discrepancy with a point-source illumination.

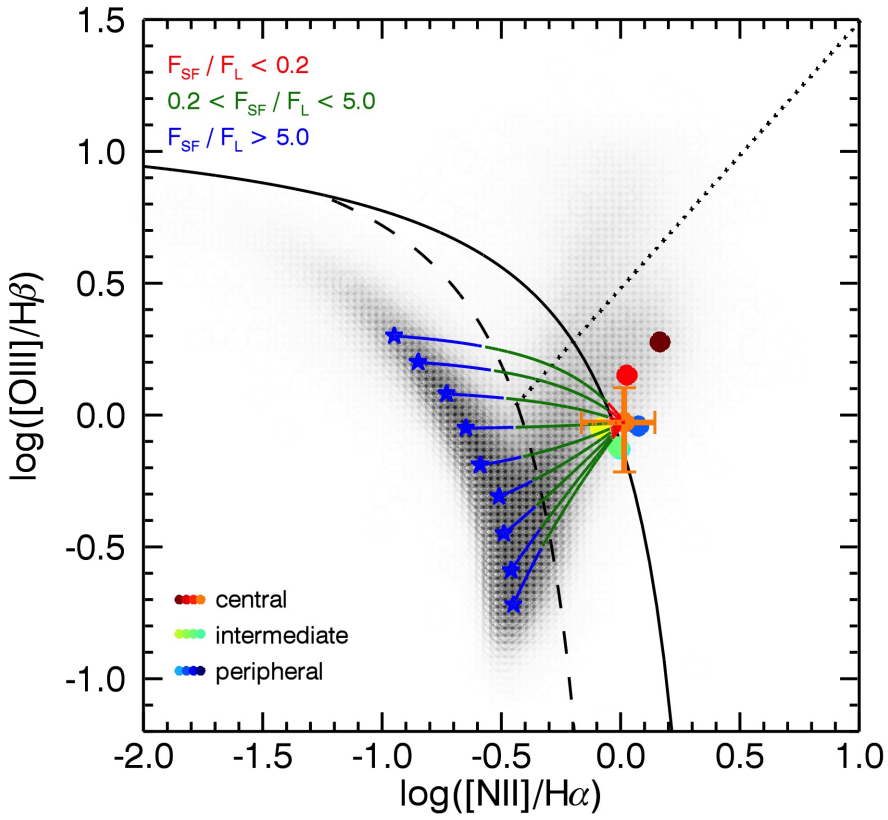

Figure 3.7: Resulting line ratios if line emission flux purely from SF (blue stars) and purely from a LINER mechanism (orange point) are linearly superposed (coloured lines). The generating Hα flux ratios are colour coded. This shows that the SF contribution in the selected LINER regime right of the solid curve is negligible (F_{SF}/F_L ¡ 0.2) and cannot be generating the discrepancy seen in radial emission line profiles with respect to a point-source illumination of >1 dex at larger radii.

Even so, we estimate the level of mixed-in SF contribution by assuming that the observed emission line fluxes are a linear combination of flux F_L from "pure LINER" ionisation and flux F_{SF} from "pure SF" ionisation. The line ratios from these pure ionisation sources correspond to points in the LINER and SF regimes of the BPT diagrams. For a given Hβ-to-Hα flux ratio, the so-called Balmer decrement, which increases the ratio F_{SF}/F_L from zero, traces a curve from the pure LINER point toward the pure SF point in the BPT diagram, as illustrated in Figure 3.7.

As the latter pure SF points (blue stars), we use locations on the SF-ridge of SDSS galaxies (Kewley et al. 2006) that are shown as grey levels in the background. We infer to the pure LINER point (orange point), from the average position of the nine elliptical LINER galaxies from our sample. These elliptical galaxies are devoid of any SF, but there could still be mixed-in ionisation contribution from a central AGN in their inner regions. Indeed, computing the position based on emission line fluxes from different galactocentric annuli shows that the two central-most annuli

(dark-red and red points) yield a position more toward the Seyfert regime. The average position resulting from the annuli further out nicely converge to the same position, again in-line with ionisation by the same but non-central sources.

To go from this pure LINER point to the black solid demarcation line, the SF-to-LINER flux ratio increases to $F_{SF}/F_L = 0.2$, so that a maximum of 1/6th of observed flux could be due to mixed-in SF contribution. The resulting decrease in the observed flux is negligible with respect to the offset from the point-source illumination in Figure 3.3. Placing the pure LINER point further away from the demarcation line increases the possible SF-to-LINER flux ratio. Given the spread in the convergence point among the elliptical galaxies (orange cross), however, we find $F_{SF}/F_L < 0.5$. Hence only 1/3rd of the observed flux could still be due to mixed-in SF contribution, and we conclude that, SF cannot be a significant source of the observed shallow emission line flux profiles even for the spiral galaxies, whereas ionisation from the same common old stars forms the natural explanation.

3.3 Discussion – part one

For 48 galaxies with LINER-like emission we unambiguously show, that the class of LINER galaxies, contrary to their 30-year old paradigm, are not predominantly powered by a central AGN, since their radial emission line surface brightness profiles are inconsistent with ionisation by a central point-source and hence cannot be due to an AGN alone.

When using this result in reverse, we conclude that the power source for LINER-like emission must be extended, which is possibly distributed all through the galaxy, while it is clear that an adequate supply of gas is indispensable for such line emission to exist in the first place.

Despite its name LINER-like emission covers all regions of the galaxies, aside from those where star-formation dominates the emission. There is also no spatial collimation as would be expected in the case of shock-driven ionisation. Henceforth, the most probable energy source are hot evolved stars after their asymptotic giant branch (AGB) phase. This was already suggested before (Binette et al. 1994; Goudfrooij 1997, 1999), but models of this phase in stellar evolution have only recently been picked up again (Stasińska et al. 2008). After stars leave their main sequence of hydrogen burning, and after a few subsequent evolutionary stages, they enter the so-called AGB. In the following post-AGB phase, the stars can become sufficiently hot to produce a spectrum capable of ionising atoms with a substantial ionisation potential. Realising this has the perplexing implication that every galaxy for both early- and late-type galaxies with stellar populations older than ~1 Gyr must have a radiation field from post-AGB stars that can ionise at least part of the interstellar gas when present.

Even if central or extended LINER-like emission is predominantly powered by post-AGB stars, it does not preclude the existence of AGNs in LINER galaxies. The AGN could provide some of the central radiation in some LINER galaxies, which may even host a higher fraction of AGN compared to the general population of massive galaxies (González-Martín et al. 2009): The reason for this could in the simplest case be a selection effect due to the required presence of central reservoirs of gas and hence potential for it being accreted onto a central black hole. However, many galaxies with LINER-like emission do not have a central AGN. This shows that the LINER diagnostic is in general not a good predictor for the presence of an AGN. In addition, relying on LINER signatures for AGN selection suffers from aperture effects: Observing galaxies at different distances therefore different physical apertures (see Figure 3.3) clearly makes a comparison of the properties even of classical LINERs difficult because of the mixing of signals from emitting regions at different radii.

This emphasises that LINERs or galaxies with widespread LINER-like emission are not just a mixed bag of properties but are mainly just normal galaxies with some gas content in the absence of substantial ionisation fields from young stars and AGN.

The consequences are profound for different fields in astrophysics, ranging from galaxy evolution models, which have hot old stars as an always-present ionisation source that create LINER-like emission whenever gas is present, to black hole studies, which do not have to resort to rare accretion models to explain the LINER galaxies. The three immediate consequences from this result are described below.

First, the ubiquitous presence of ionising radiation from post-AGB stars means that *galaxies with LINER-like emission are not a class defined by a property, but rather by the absence of a property*, or the absence of a stronger radiation field, as for example produced by young stars. This both explains why typical LINER galaxies are massive and old: These are the only galaxies without substantial star formation and with enough post-AGB stars to generally detect the LINER signature (Papaderos et al. 2013). This also tells us why LINERs appeared as a mixed bag: The presence of other sources of energy – AGN, star formation, shocks – is actually completely independent of the source powering the LINER signature.

Second, we need to revisit the properties of classical AGN host galaxies, since a number of studies in the past decade used, for example, the SDSS survey to investigate AGN host galaxies in the local Universe. Since the sample selection LINERs outnumber classical Seyferts 5:1, were often counted into the AGN class (Kauffmann et al. 2003c; Kauffmann & Heckman 2009; Schawinski et al. 2007), and were being impacted by the different physical apertures covered at different redshifts (Figure 3.3), these studies might have come to biased results.

Third, with LINER-signatures now being removed as a self-contained AGN indicator, the family of AGN becomes much smaller and simpler.

4 Stellar ages and ionisation mechanisms

4.1 Introduction

Among the first 257 galaxies observed with the CALIFA survey, we have shown in the previous chapter and Singh et al. (2013) that for a sample of 48 LINER galaxies, low-ionisation *nuclear* emission line regions were not only detected in their nuclei, as presumed by its definition, but rather spatially extended with emission line surface-brightness profiles contradicting the expected illumination by a point source.

To go beyond this analysis, we postulate that LINER-like emission occurs not only in certain galaxies, and thus defining a class, but rather that it is an omnipresent feature due to ubiquitous amounts of UV emission by hot old stars. It is only due to the lack of a stronger radiation field from young stars and in the absence of a powerful AGN that one can detect the underlying LINER-like emission.

Our emission line measurement avoids to model the line flux after a previous subtraction of the stellar continuum. Instead, continuum and line emission are modelled simultaneously, which provides the least biased line measurement (Sarzi et al. 2006). We use again the gas and absorption line fitting procedure GANDALF (Sarzi et al. 2006) with the MILES (Sánchez-Blázquez et al. 2006; Falcón-Barroso et al. 2011) library of single stellar populations. The best fit to a spectrum is the superposition of an optimal combination of the stellar templates with additional Gaussians representing the emission lines.

Here we analysed 369 galaxies, of which 267 (72%) are showing LINER-like emission (also see Figure 1.4), sorted into a separate sub-sample, and 117 galaxies (32%) where LINER-like regions did not only consist of individual or a few spaxels but are composed of larger patches. We put 36 galaxies into a separate sub-sample, for a separate analysis, since they showed significant

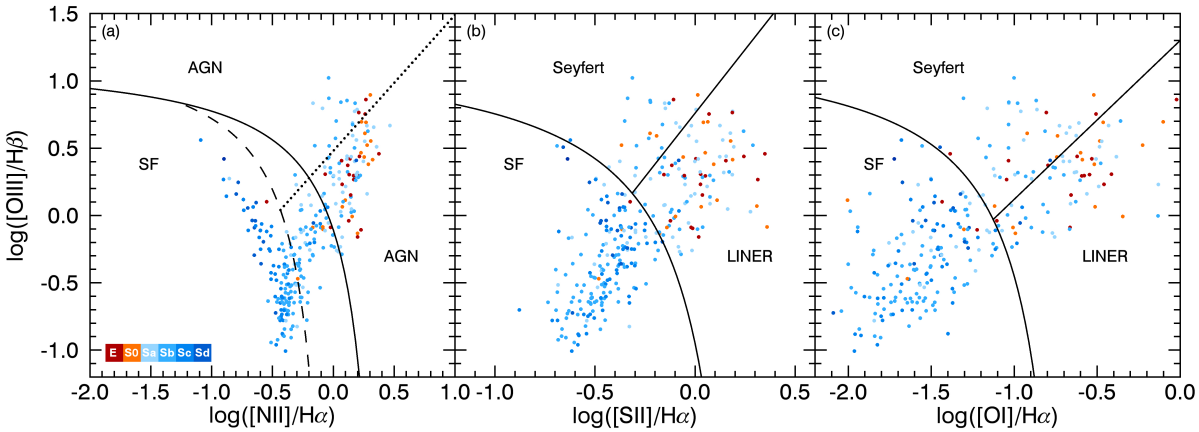

Figure 4.1: BPT diagram. We show the emission line ratios of the central 3″-diameter apertures of 369 CALIFA galaxies. Data points are coloured by Hubble type. The solid curved lines are the theoretically modelled "extreme starburst lines" (Kewley et al. 2001). The dashed line (Kauffmann et al. 2003c) and the dotted line (Cid Fernandes et al. 2010) in (a) and the straight solid lines (Kewley et al. 2006) in (b) and (c) are tracing a minimum in the central emission line ratio distribution of SDSS galaxies.

evidence of a recent or ongoing galaxy galaxy interaction. This is crucial since contribution to LINER-like emission from shock ionisation in merging galaxies cannot be ruled out or unambiguously disentangled from other mechanisms. For the following analysis we chose a signal to noise threshold of 20 (in the continuum) to ensure that our results are only minimally, if at all, affected by erroneous fits and misclassified spaxels. The GANDALF emission line fitting code provides errors for emission lines which are fitted freely, e.g. unrestricted in their kinematical properties. These are, in our case, Hα and [NII]λ6583. Emission lines that are being tied to another line in either velocity or velocity dispersion are better recovered (Sarzi et al. 2006) but do not come with errors for the measured fluxes. Assuming that the gas is co-spatial and subject to the same kinematics, we tied other Balmer lines in velocity with respect to Hα and other metal lines to [NII]λ6583 respectively. As an additional constraint, the relative errors in emission line ratios (here Hα/[NII]) have to be below 50%.

For our analysis regarding stellar ages in section 4.3, a different sub-sample had to be used. From the total sample of 369 galaxies only those remained viable for which both, V500 and V1200 data were available, which means that each galaxy must have been observed with both gratings. Following this constraint we obtained 193 galaxies with LINER signatures, separating off 26 cases of interacting galaxies and excluding 50 without LINER-like emission.

The emission line ratio diagnostic diagram in Figure 4.1 displays our full sample of 369 galaxies. It is used to distinguish between star formation, which is dominated by Balmer Hα and Hβ lines, Seyfert galaxies which have a high ionisation potential, and LINER galaxies, which have low

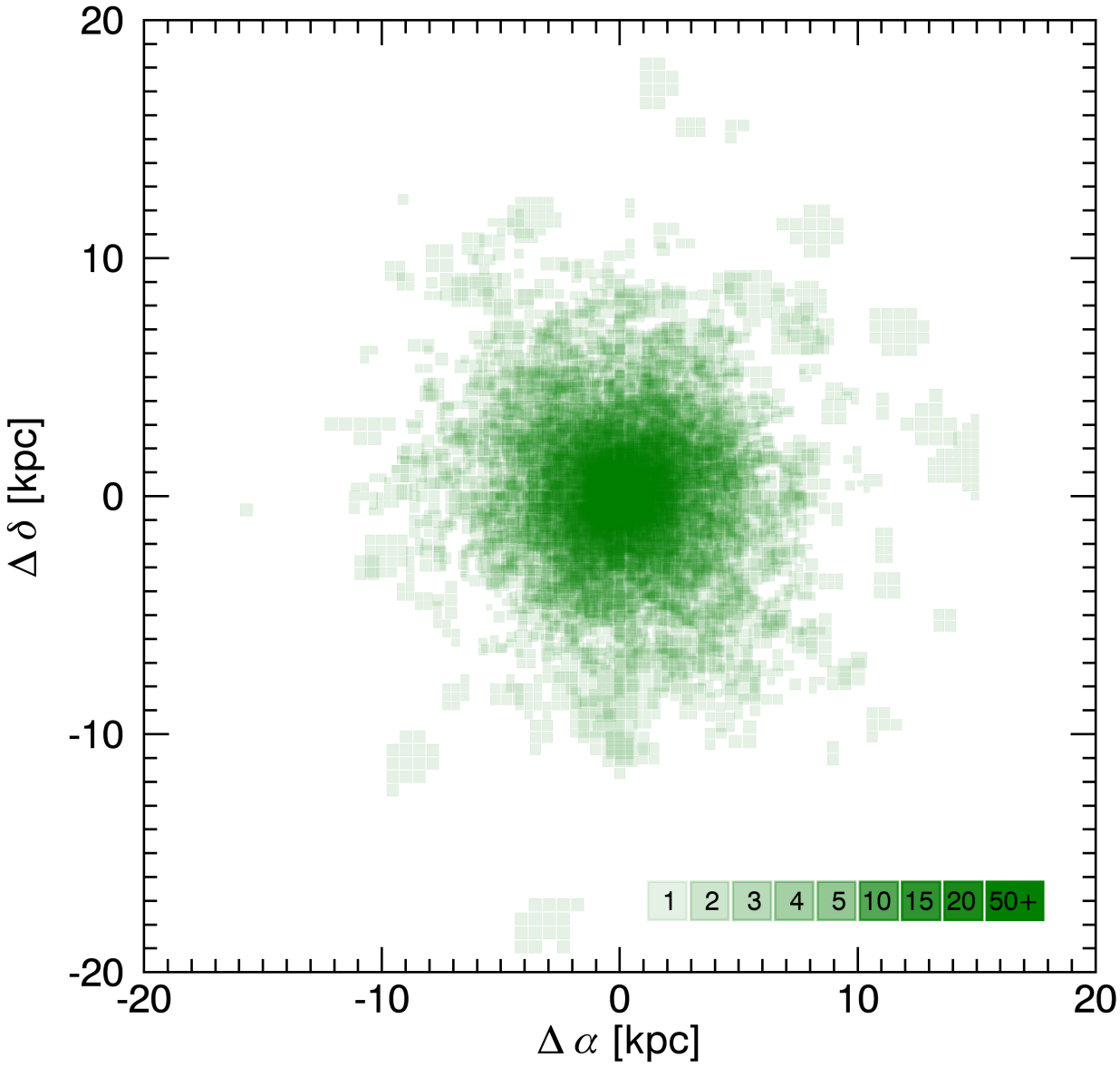

Figure 4.2: Cumulative liner regions. Stacked map with regions of LINER-like emission in 267 galaxies, excluding galaxies with signs of recent or ongoing interaction. LINER regions in each galaxy are plotted with 90% transparency. The amount of transparency for different numbers of overlay is shown in the legend.

ionisation lines. Following previous work with SDSS data, we plotted the integrated emission line flux ratios of all spaxels within a central 3 arcsec aperture.

Figure 4.2 shows the cumulative 2-D spatial distribution of all LINER-like regions for the sample of 267 galaxies for non-interacting galaxies. The boxes in the lower right corner show the amount of overlap for different numbers of over-plotted LINER-like regions, going left to right

from 1 (least opaque) to 50 or more (most opaque) over-plotted regions. The intensity gradient unsurprisingly shows fewer LINER-like regions at greater radial distance. This map shows again that LINER-like emission is not at all nuclear but covers all regions of galaxies. If LINER-like emission stems from ubiquitous hot old stars, the higher concentration of LINER-like regions in the centre can come from several factors. A typically higher gas fraction in the centre and radially decreasing filling factor, combined with the necessary absence of star formation, and a radially decreasing signal to noise ratio can lead to increased detection of LINER signatures in the centre relative to the outer parts. Furthermore LINER-like emission is not exclusively but predominantly seen in early type galaxies due to the absence of a stronger radiation field from regions of star-formation. In star forming galaxies, LINER-like emission is only seen, when the centre of the galaxy is not dominated by star-formation anymore. Galaxies that are centrally dominated by star-formation tend to lie completely on the HII part of the BPT diagram. Again, the contribution from low-power AGN activity in the innermost few arcsec cannot be ruled out but has been shown to be insufficient to power the large scale LINER emission (Singh et al. 2013).

4.2 Hα EQUIVALENT WIDTH

We analysed the distribution of equivalent width in Hα (EW(Hα)) and in other emission lines to corroborate the picture of LINER-like emission being powered by hot old stars. We examined for a large number of galaxies, whether their emission line regions show any [trend] with regard to the BPT classifications.

It has been shown by Cid Fernandes et al. (2011) that a value of 3 Å or less in EW(Hα) corresponds to ”retired galaxies” (or ”fake AGNs”) which are galaxies that have stopped their formation of stars and are now ionised by hot low-mass evolved stars (HOLMES; Flores-Fajardo et al. 2011).

The histogram in Figure 4.3 is the result after categorising every Voronoi bin of all 369 galaxies using the BPT diagnostic and measuring the EW(Hα) of each region. It shows a well separated bi-modal distribution for LINER-like and star-forming regions. The vertical red line at 3 Å is the threshold from Cid Fernandes et al. (2011) below which galaxies do not sustain star-formation. We show that this is not only true for the central 3 arcsec aperture of SDSS galaxies but also in a spatially resolved view for regions of individual galaxies. The LINER-like emission line regions typically peak at ~1 Å, similar to regions with Seyfert emission, while regions of star-formation peak at one order of magnitude higher.

The Hα equivalent width however does not provide the opportunity to distinguish between Seyfert and LINER-like emission. The emission from the intermediate regions, which is believed to be a mixture of both sources of ionisation, seems to fill the gap between the SF-LINER bi-modal distribution. We did not find equivalent widths of other emission lines that better separate the bi-modal distribution or help to distinguish between Seyfert and LINER-like emission.

For example EW([OIII]) is equally low at ~0.6 Å for all emission line regions, thus not a useful discriminator.

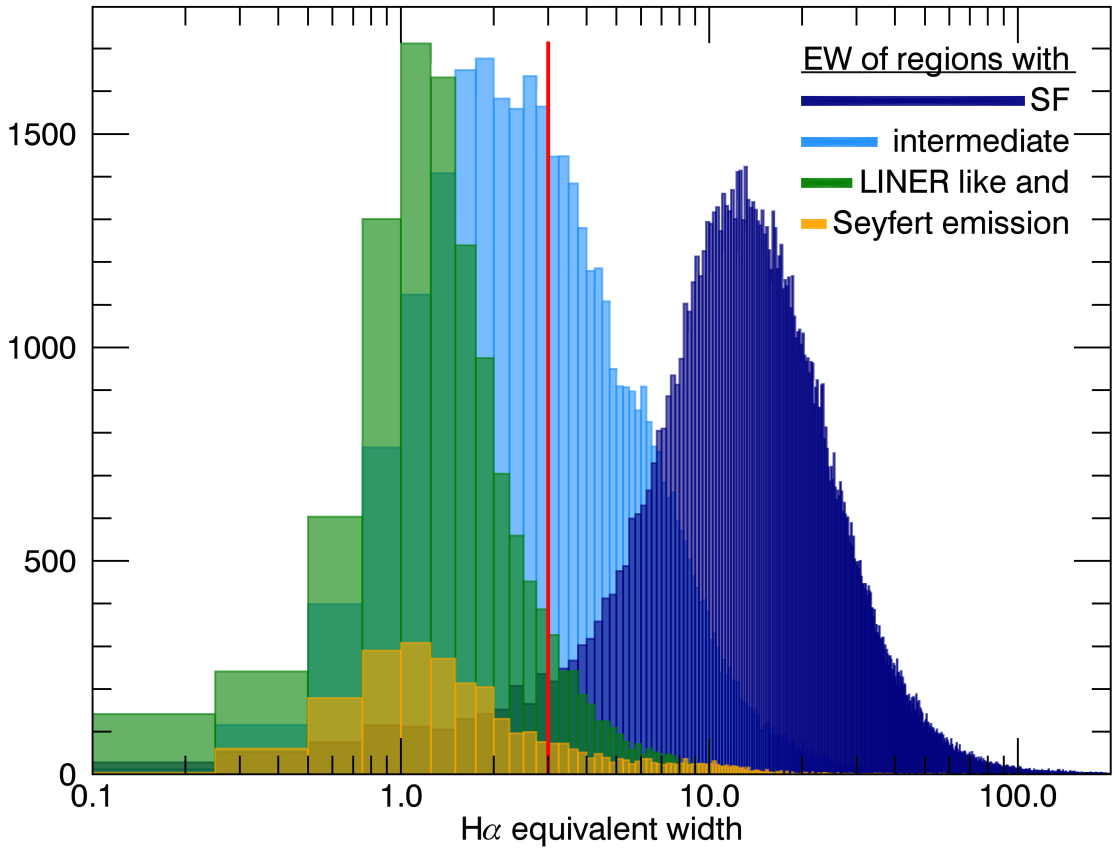

Figure 4.3: Histogram of the Hα equivalent width for individual regions in 369 CALIFA galaxies. There is a bi-modal distribution of regions with star-forming and LINER-like emission. The vertical red line at 3 Å indicates the empirically found threshold value (Cid Fernandes et al. 2011) between galaxies with star-formation and retired galaxies.

4.3 STELLAR AGES

The star-formation histories (SFHs) were calculated and provided by A. Gallazzi (see Gallazzi et al. 2005). The method is based on indices-fitting and its idea goes back to Kauffmann et al. (2003c). The following two paragraphs give an overview of the method. More specific details are explained in Gallazzi et al. (2005).

The observational constraints are a set of absorption features, both age- and metal-sensitive features to lift as much as possible the age-metallicity degeneracy. Using as bases stellar-population synthesis (SPS) models like the BC03 models, which have solar-scaled abundances, the preferred set of indices includes D4000n, Hβ, Hδ+Hγ, [MgFe], and [Mg2Fe] which are the least affected by α/Fe variations.

The main difference to other methods is the adoption of a Bayesian approach. Instead of looking for the best-fitting linear combination of single stellar populations (SSPs), or reconstruction of

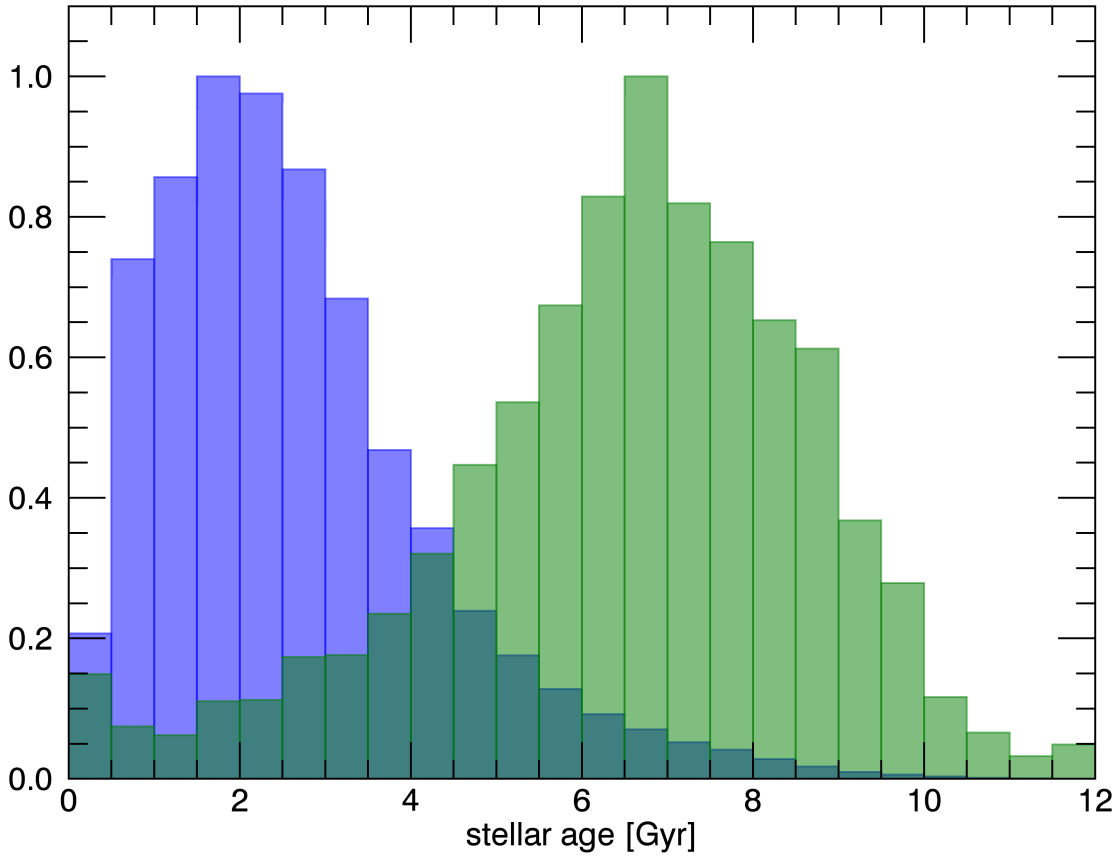

Figure 4.4: Stellar ages. Normalised histograms of light-weighted stellar ages for regions with star-formation (blue) and LINER-like emission (green) in 193 galaxies.

SFHs, a large suite of random SFHs is being considered. Each model is weighted by its goodness of fit and the probability density function (PDF) of a particular parameter (e.g. light-weighted age) is obtained by marginalising over all the other parameters of our models. In the specific case, the SFHs are modelled with an exponential law, superposed with random bursts. No dust is included as indices are minimally affected by dust. The median of the PDF is typically taken as the fiducial parameter estimate, and the 16-84 percentiles for the 1-sigma uncertainty. This uncertainty includes the degeneracy of all the possible SFHs that can lead to the observed features, which might be more realistic. Other methods, like Starlight, do not define a prior distribution of parametrised SFHs but they solve for a linear combination of SSPs. Also uncertainties due to dust-corrections become unavoidable, which is imperative if the whole spectra are to be fitted.

In our analysis of the spatial distribution of stellar ages we found a strong correlation between regions within galaxies that show LINER-like emission and their mean stellar age. LINER-like emission is mostly found in regions with older stellar populations. Regions with LINER-like emission have a median age of 6.72 Gyr, Seyfert regions are on average 5.61 Gyr old, composite/intermediate regions 4.44 Gyr and regions of star-formation 2.36 Gyr. Even though the distribution of stellar ages in star-forming and LINER regions have an overlap, both peak at very different ages. Figure 4.4 shows that there is a difference of 5 Gyr between both peaks with a 4.36 Gyr difference in their median values.

4.4 LINER "ICING" ON EDGE-ON DISKS

The example of UGC10043 in Figure 4.5 shows a galaxy perfectly edge-on with a disk dominated by star formation and a slightly harder radiation field around the central bulge. Interestingly a few galaxies like this one, reveal LINER-like emission in the outskirts around the bulge or above the disk. These LINER-like regions are associated with a low velocity dispersion of few tens km s^{-1}, inconsistent with ionisation even by slow shocks, but consistent with the hypothesis of ionisation by hot old stars. These LINER-like regions are seen, where apparently the radiation field from young hot stars in the disk becomes negligible to the older stellar body in the bulge. Furthermore the EW(Hα) in these regions is $\leq$ 3Å. The BPT map of UGC10043 also shows that the emission from the intermediate (a.k.a. composite) regions might in fact be just a mixture of both ionisation sources.

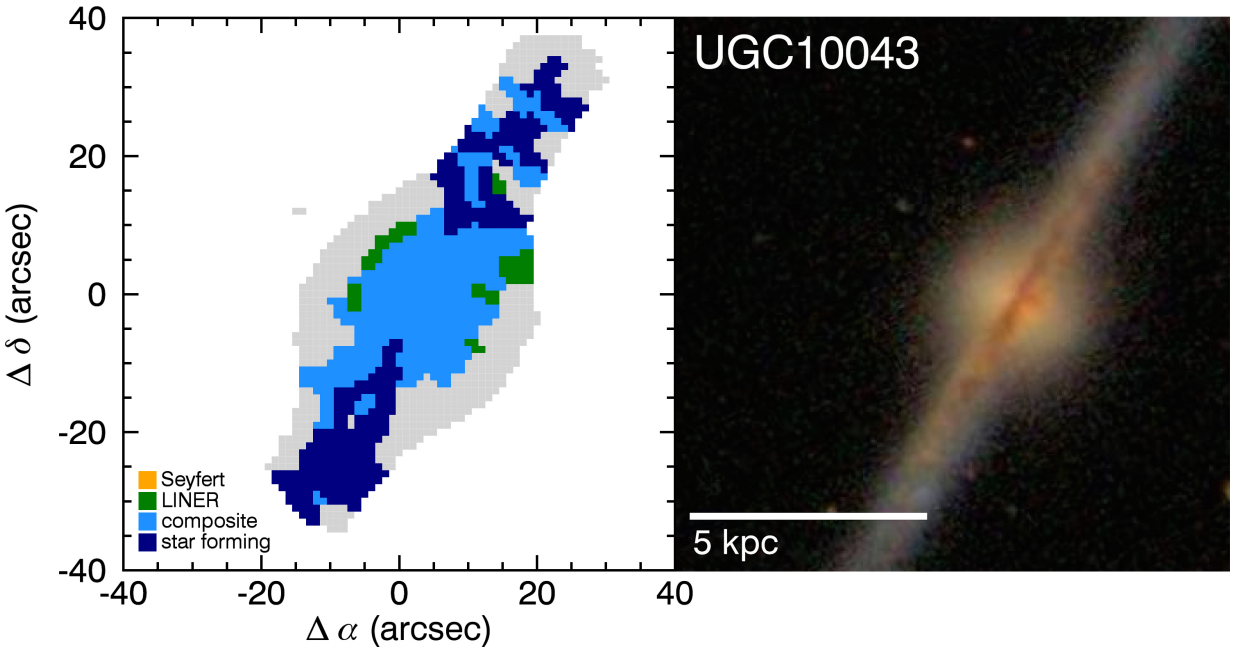

Figure 4.5: LINER coating. Edge-on disk galaxy UGC10043. Left: BPT map with SF dominated disk (blue) and LINER-like emission (green) coating the bulge (light-blue). Right: optical SDSS image

4.5 LINER EMISSION IN INTERACTING GALAXIES

From our total sample of 369 galaxies, 36 show signs of recent or ongoing interaction, and were, as previously mentioned, excluded from the preceding analysis. UV radiation from hot old stars is not the only viable ionisation mechanism which can lead to LINER-like emission. The characteristic emission line ratios in regions with LINER-like emission can as well be induced by fast radiative shocks (Dopita & Sutherland 1996; Dopita et al. 1996), and slow shocks with velocities around 100 - 250 km s^{-1} (Rich et al. 2010, 2011; Farage et al. 2010). Shock excitation is particularly important in galaxy mergers and galaxies with large scale outflows. It can be seen in a number of CALIFA galaxies, of which we show one example in Figure 4.6.

NGC3303 is one of several interacting galaxies which has been observed with CALIFA. Figure 4.6 shows the BPT map and SDSS image of this violent interaction. The LINER-like emission in this case is seen across the whole galaxy and post-AGB stars are most likely not the dominating source of ionisation. The gas velocity dispersion in the "LINER-regions" of this galaxy go beyond 200 km s^{-1}. Figure 4.7 shows that the Hα equivalent width does not exhibit a similar behaviour as seen in Figure 4.3. The BPT-classified LINER regions do not follow the same trend of having a low EW(Hα) value. Instead regions with LINER-like ionisation are mostly above 3 Å and up to one order of magnitude higher in EW(Hα) than what would be expected for ionisation by hot old stars.

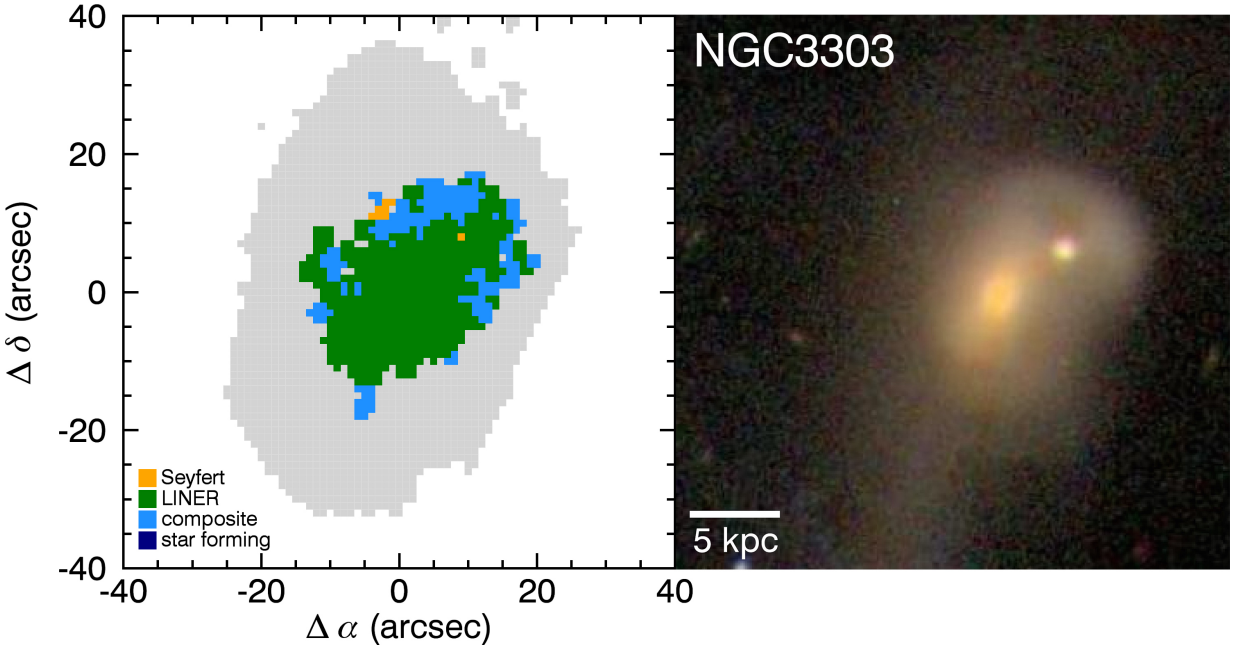

Figure 4.6: Galaxy merger. Example of a merging galaxy (NGC3303) and the large scale, shock induced regions of LINER-like emission line ratios. Left: BPT map with LINER signatures in green. Right: optical SDSS image

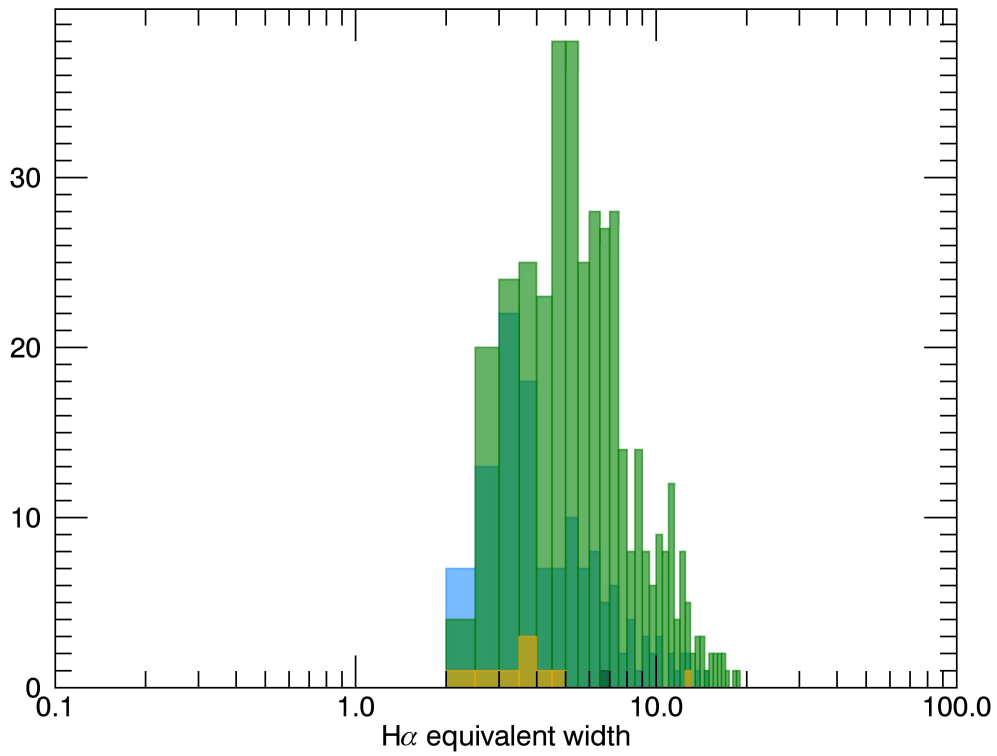

Figure 4.7: EW(Hα) histogram for NGC3303. All regions with LINER-like emission have EW(Hα) $\geq$ 2 Å, most of which are above 3 Å and up to one order of magnitude higher than what would be expected for ionisation by hot old stars.

4.6 DISCUSSION – PART TWO

LINER-like emission line regions are a ubiquitous phenomenon in many galaxies across all regions, and across all morphological types. It has been shown in Singh et al. (2013) for 48 galaxies with central LINER-like emission, that the LINER galaxies are predominantly not powered by a central AGN. Their radial emission line surface brightness profiles are inconsistent with ionisation by a central point-source and therefore cannot be due to an AGN alone. While we do not claim that galaxies with LINER-like emission never have an AGN, we rule out its contribution to the spatially extended LINER-like emission, since, if it has an effect at all, it only affects the innermost central region and not the spatially extended part.

We confirmed for an even larger sample that for non-merging galaxies, LINER-like emission occurs on all scales, across all morphological types, from the centre to the outskirts. While acknowledging that LINER-like emission can also be caused by shocks in interacting galaxies, when excluding such cases we put the focus on two indicators for hot old stars in non-interacting galaxies: the stellar ages, and equivalent width of H. After refuting the low-luminosity AGN paradigm, this work shows that regions with LINER signatures can well be explained in the post-AGB framework. With ~7 Gyr, the stellar populations in regions with LINER-like emission are one of the oldest, followed by Seyfert regions with ~6 Gyr and a stark contrast to star-forming regions at ~2 Gyr. In addition, an equivalent width value in Hα below 3 Å, which has been shown to trace galaxies that have stopped their star-formation and are only ionised by hot and evolved stars, correlates significantly with the spatial locations of LINER-like emission.

5

Summary and Outlook

Since the 1980s, when galaxies with low ionisation nuclear emission line regions have first been identified, they were thought to be part of the AGN population. It was clear from the beginning that the ionising radiation field, that causes strong detections of weakly ionised atoms, in that newly discovered class, could not be spectrally identified with young hot stars from regions of star-formation. Few authors proposed that the peculiar emission lines of low ionisation might be created by shocks and other mechanisms. Fast radiative shocks as well as slow shocks with velocities of 100 - 250 km s^{-1} have been studied, and while certainly some galaxies with LINER-like emission, can be associated with shocks, the bulk of it can not. Shock excitation mainly occurs in galaxies with large scale outflows and in interacting galaxies, as we have shown as well. In the last years, doubts about the AGN explanation were again re-fuelled. Inconsistencies were found between the AGN-ionisation hypothesis, and either predicted emission line strengths or the spatial distribution of LINER-like ionised regions in galaxies, but neither was conclusive, because they either lacked full spatial or spectral coverage.

It is important to understand *the true nature of LINER galaxies* because they are not rare and isolated instances. They are in fact very common. Only 1 out of 4 galaxies does *not* show LINER-like emission and among the AGN population they constitute the largest fraction. The physics of LINERs has never been properly described theoretically in an AGN context, but they were nevertheless included in AGN samples. It is therefore crucial to understand the main mechanism for LINER-like emission.

The initial aim of this thesis was to study not only central regions of galaxies but entire, spatially resolved galaxies, with the help of a new set of observational data. This data combines for the first time spectroscopic information of the whole optical wavelength range at each position across the optical extend of up to 600 nearby galaxies. Our results are based on observations from the Calar Alto Integral Field Area (CALIFA) survey of nearby galaxies. CALIFA provides

spatially resolved galaxy spectroscopy over a ∼1 arcmin field-of-view. It covers the full optical wavelength range which includes the emission lines Hα, Hβ, [OIII], [OI], [NII], and [SII], which enables us to apply the standard emission line ratio diagnostics (BPT) to identify regions within galaxies based on their ionisation characteristics. The BPT diagnostic was initially used for entire galaxies, but the advent of integral field spectroscopy made it possible to analyse individual galaxies on a spatially resolved basis.

We have unambiguously shown that the class of LINER galaxies, contrary to their 30-year-old paradigm, are not powered by a central AGN alone. Following a conservative assumption that the gas density is constant with radius, the geometrical dilution of the radiation field from an AGN drops off as $1/r^2$. This is an upper limit, because the expected gas density would actually fall off with increasing radius. At first we analysed 48 LINER galaxies following the literal definition of having LINER emission in the centre. For each galaxy we selected all spatial regions which exhibit LINER characteristics, and excluded regions that show star-formation or Seyfert emission. Comparing the observed emission line surface brightness profiles for LINER regions of 48 galaxies, against the expected profile from a centrally illuminating point-source like AGN, reveals a significant and increasing gap towards larger radial distances. If any of these galaxies host an AGN, it may only affect the very innermost region, but the observed excess in flux can not be explained by an AGN alone. This result necessitates another ionisation mechanism that can explain the observed emission line ratios.

Next, we have shown for a sample of 267 non-merging galaxies, that LINER-like emission occurs on all scales, across all morphological types, from the centre to the outskirts and focus our analysis on ionisation by hot old stars. These post-AGB stars have a very short but hot phase. They are ubiquitous, also in massive early type galaxies, and should roughly be distributed as the bulk of stellar mass. This would provide a *distributed* light source, immediately explaining the observed radial line profiles. While acknowledging that LINER-like emission can also be caused by shocks in interacting galaxies, we put such cases into a separate analysis, and focus on two indicators for hot old stars in non-interacting galaxies. We analyse the light weighted mean stellar ages and equivalent width of Hα, EW(Hα), in regions with LINER-like emission, finding that a strong correlation exists between those spatial regions and first of all their stellar age and secondly a low EW(Hα). It has been shown by others, that galaxies with EW(Hα) < 3 Å are so called retired galaxies, which means that they have stopped forming stars and are ionised by hot low-mass evolved stars. We could show that individual regions in 369 galaxies follow the same trend. Regions with LINER-like emission are typically below 3 Å and peak around 1 Å, while star-forming regions are almost always above 3 Å, up to 100 Å, with a peak around 15 Å. Furthermore, regions with LINER-like emission have on average the oldest stellar population (∼7 Gyr), separated by 5 Gyr to regions with star-formation (∼2 Gyr).

In conclusion, we have shown that the low-luminosity AGN explanation can be ruled out as the sole ionisation mechanism in LINER galaxies and since both, the high stellar ages and low EW(Hα) in LINER regions, corroborate the hypothesis of ionisation by hot old stars, they are a very likely and plausible source of the ionisation.

Further studies could for example examine the contribution and influence of shocks and outflows on LINER regions by doing a kinematical analysis. Outflows can be detected due to an increase in velocity dispersion with additional line components of different velocities. It is possible to modify the emission line fitting routine GANDALF such that multiple line components, with different kinematical properties, can be fitted. An automated detection for the analysis of many galaxies, like in the CALIFA survey, could be done by applying a harmonic decomposition and remove a smooth component from the kinematics to detect cone-like structures in the kinematics and/or line ratios.

Another potentially interesting idea, is to look into our own galaxy. With data from the still ongoing Wisconsin H-Alpha Mapper (WHAM) survey, which maps the ionised gas in the Milky Way, one could transfer our extragalactic analysis to our own Galaxy. This survey detects several emission lines that are needed for the commonly used emission line ratio diagnostics, and mapping the distribution and properties of LINER-like emission regions within our own galaxy would be something that has never been done before.

Bibliography

Allington-Smith, J., & Content, R. 1998, PASP, 110, 1216

Antonucci, R. 1993, Annual Review of Astronomy and Astrophysics, 31, 473

Bacon, R., et al. 2001, MNRAS, 326, 23

Baldwin, J. A., Phillips, M. M., & Terlevich, R. 1981, PASP, 93, 5

Bell, E. F., et al. 2004, ApJ, 608, 752

Bigiel, F., & Blitz, L. 2012, ApJ, 756, 183

Binette, L., Magris, C. G., Stasińska, G., & Bruzual, A. G. 1994, A&A, 292, 13

Bonnet, H., et al. 2004, The Messenger, 117, 17

Cappellari, M., & Copin, Y. 2003, MNRAS, 342, 345

Cappellari, M., & Emsellem, E. 2004, PASP, 116, 138

Cid Fernandes, R., Stasińska, G., Mateus, A., & Vale Asari, N. 2011, MNRAS, 413, 1687

Cid Fernandes, R., Stasińska, G., Schlickmann, M. S., Mateus, A., Vale Asari, N., Schoenell, W., & Sodré, L. 2010, MNRAS, 403, 1036

Croom, S. M., et al. 2012, MNRAS, 421, 872

Dopita, M. A., Koratkar, A. P., Evans, I. N., Allen, M., Bicknell, G. V., Sutherland, R. S., Hawley, J. F., & Sadler, E. 1996, in Astronomical Society of the Pacific Conference Series, Vol. 103, The Physics of Liners in View of Recent Observations, ed. M. Eracleous, A. Koratkar, C. Leitherer, & L. Ho, 44

Dopita, M. A., & Sutherland, R. S. 1996, ApJS, 102, 161

Faber, S. M., et al. 2007, ApJ, 665, 265

Falcón-Barroso, J., Lyubenova, M., van de Ven, G., & the CALIFA collaboration. 2014, ArXiv e-prints

Falcón-Barroso, J., Sánchez-Blázquez, P., Vazdekis, A., Ricciardelli, E., Cardiel, N., Cenarro, A. J., Gorgas, J., & Peletier, R. F. 2011, A&A, 532, A95

Farage, C. L., McGregor, P. J., Dopita, M. A., & Bicknell, G. V. 2010, ApJ, 724, 267

Ferland, G. J., & Netzer, H. 1983, ApJ, 264, 105

Flores-Fajardo, N., Morisset, C., Stasińska, G., & Binette, L. 2011, MNRAS, 415, 2182

Gallazzi, A., Charlot, S., Brinchmann, J., White, S. D. M., & Tremonti, C. A. 2005, MNRAS, 362, 41

García-Benito, R., et al. 2014, ArXiv e-prints

Garcia-Lorenzo, B., et al. 2014, A&A

González-Martín, O., Masegosa, J., Márquez, I., Guainazzi, M., & Jiménez-Bailón, E. 2009, A&A, 506, 1107

Goudfrooij, P. 1997, in Astronomical Society of the Pacific Conference Series, Vol. 116, The Nature of Elliptical Galaxies; 2nd Stromlo Symposium, ed. M. Arnaboldi, G. S. Da Costa, & P. Saha, 338

Goudfrooij, P. 1999, in Astronomical Society of the Pacific Conference Series, Vol. 163, Star Formation in Early Type Galaxies, ed. P. Carral & J. Cepa, 55

Halpern, J. P., & Steiner, J. E. 1983, ApJ, 269, L37

Heckman, T. M. 1980, A&A, 87, 152

Hubble, E. P. 1926, ApJ, 64, 321

Husemann, B., et al. 2013, A&A, 549, A87

Juneau, S., Dickinson, M., Alexander, D. M., & Salim, S. 2011, ApJ, 736, 104

Juneau, S., et al. 2014, ApJ, 788, 88

Kauffmann, G., & Heckman, T. M. 2009, MNRAS, 397, 135

Kauffmann, G., et al. 2003a, MNRAS, 341, 33

—. 2003b, MNRAS, 341, 54

—. 2003c, MNRAS, 346, 1055

Kelz, A., et al. 2006, PASP, 118, 129

Kewley, L. J., Dopita, M. A., Sutherland, R. S., Heisler, C. A., & Trevena, J. 2001, ApJ, 556, 121

Kewley, L. J., Groves, B., Kauffmann, G., & Heckman, T. 2006, MNRAS, 372, 961

Lamareille, F. 2010, A&A, 509, A53

Lamareille, F., Mouhcine, M., Contini, T., Lewis, I., & Maddox, S. 2004, MNRAS, 350, 396

Martini, P., & Weinberg, D. H. 2001, ApJ, 547, 12

Narayan, R., & Yi, I. 1994, ApJ, 428, L13

Papaderos, P., et al. 2013, A&A

Pérez, E., et al. 2013, ApJ, 764, L1

Rich, J. A., Dopita, M. A., Kewley, L. J., & Rupke, D. S. N. 2010, ApJ, 721, 505

Rich, J. A., Kewley, L. J., & Dopita, M. A. 2011, ApJ, 734, 87

Roth, M. M., et al. 2005, PASP, 117, 620

Sánchez, S. F., et al. 2012, A&A, 538, A8

—. 2013, A&A, 554, A58

Sánchez-Blázquez, P., et al. 2006, MNRAS, 371, 703

Sarzi, M., et al. 2006, MNRAS, 366, 1151

—. 2010, MNRAS, 402, 2187

Schawinski, K., Thomas, D., Sarzi, M., Maraston, C., Kaviraj, S., Joo, S.-J., Yi, S. K., & Silk, J. 2007, MNRAS, 382, 1415

Schneider, P. 2014, Extragalactic Astronomy and Cosmology, 2nd edn. (Springer)

Seyfert, C. K. 1943, ApJ, 97, 28

Shakura, N. I., & Sunyaev, R. A. 1973, A&A, 24, 337

Singh, R., et al. 2013, A&A, 558, A43

Stasińska, G., Cid Fernandes, R., Mateus, A., Sodré, L., & Asari, N. V. 2006, MNRAS, 371, 972

Stasińska, G., et al. 2008, MNRAS, 391, L29

Stein, W. A., O'Dell, S. L., & Strittmatter, P. A. 1976, Annual Review of Astronomy and Astrophysics, 14, 173

Terlevich, R., & Melnick, J. 1985, MNRAS, 213, 841

Trouille, L., Barger, A. J., & Tremonti, C. 2011, ApJ, 742, 46

Urry, C. M., & Padovani, P. 1995, PASP, 107, 803

Vanderriest, C. 1980, PASP, 92, 858

Veilleux, S., & Osterbrock, D. E. 1987, ApJS, 63, 295

Yan, R., & Blanton, M. R. 2012, ApJ, 747, 61

Yan, R., et al. 2011, ApJ, 728, 38

List of Figures